Extracting Energy from Unsteady Flows through Vortex Control

by

Knut Streitlien

S.M., Ocean Engineering, MIT (1990)
Sivilingeniør, Marine Technology, Norwegian Institute of Technology (1987)

Submitted in partial fulfillment of the
requirements for the degree of

DOCTOR OF PHILOSOPHY IN OCEANOGRAPHIC ENGINEERING

at the

MASSACHUSETTS INSTITUTE OF TECHNOLOGY

and the

WOODS HOLE OCEANOGRAPHIC INSTITUTION

September 1994

Signature of Author .....
Joint Program in Applied Ocean Science and Engineering
Massachusetts Institute of Technology
Woods Hole Oceanographic Institution
September 1994

Certified by .....
Prof. Michael S. Triantafyllou
Professor, MIT
Thesis Supervisor

Certified by .....
Dr. Mark A. Grosenbaugh
Associate Scientist, WHOI
Thesis Supervisor

Accepted by .....
Prof. Arthur B. Baggeroer
Chairman, Joint Committee for Applied Ocean Science and Engineering
Massachusetts Institute of Technology/Woods Hole Oceanographic Institution

Extracting Energy from Unsteady Flows through Vortex Control

by

Knut Streitlien

Submitted to the Massachusetts Institute of Technology/
Woods Hole Oceanographic Institution
Joint Program in Applied Ocean Science and Engineering
on September 1994, in partial fulfillment of the
requirements for the degree of
Doctor of Philosopy

Abstract

Vortex control is a new paradigm in fluid mechanics, with applications to propulsion and wake reduction. A heaving and pitching hydrofoil placed in a flow with an array of oncoming vortices can achieve a very high propulsive efficiency and reduced wake signature. The canonical example of flow with regular arrays of vortices is the Kármán vortex street, and this is our model for the inflow to the foil.

The problem of an oscillating foil placed within a Kármán vortex street is investigated with a theoretical model and numerical simulation. The theoretical model is an adaptation of the classical linear theory for unsteady aerofoils. It combines the effects of nonuniform inflow and foil motion to predict the resulting thrust, lift, and moment.

The numerical procedure allows for nonlinear interaction between the foil, performing large amplitude oscillations, and the oncoming vortex street. The method is based on two–dimensional potential flow and the theory of functions of a complex variable. Careful formulation of the velocity potential, and closed form expressions for force and moment on a Joukowski foil in the presence of point vortices, permits rapid evaluation of hydrodynamic performance.

The theory and simulation results agree in their main conclusion: For optimum performance, the foil should try to intercept the vortices head on, while remaining inside the border of the oncoming vortex street. This mode is associated with a high degree of interaction between oppositely signed vorticity in the combined wake leading to reduced wake signature. The lowest efficiency is predicted when the foil avoids coming close to the vortices, here the combined wake consists of a row of very strong vortices of alternate sign. The theory also indicates that an oscillating foil can recover more of the energy contained in the vortex street than a stationary one, but this has not been confirmed in simulation.

The interaction process in the wake is studied in more detail, using a much simplified model; the foil wake is modeled as a uniform shear layer of small but finite

thickness, and an oppositely signed vortex is placed next to it to simulate the effect of one of the vortices in the Kármán street. The subsequent interaction is simulated with the vortex method, assuming periodic boundary conditions.

These simulations show that the shear layer rolls up and partially engulfs the vortex patch when two conditions are satisfied. The vortex must be close to the shear layer, and the circulation about the vortex and a representative segment of the shear layer must balance, such that neither one dominates the problem.

In both of these simulations, a fast, $O(N)$, vortex summation method based on multipole expansions is used, with special adaptations to account for the influence of image vortices.

Thesis Supervisor: Prof. Michael S. Triantafyllou
Professor, MIT

Thesis Supervisor: Dr. Mark A. Grosenbaugh
Associate Scientist, WHOI

Acknowledgments

This work was funded by the MIT Sea Grant College Program under grant number NA90AA-D-SG424 by ARPA, and the Office of Naval Research, under contracts N00014-92-J-1726 and N00014-93-1-0587.

However, there are many other people that deserve credit for being of help in my research.

Thanks to my advisor, Mike Triantafyllou for providing the original idea for the thesis, and he and my other committee members, Dick Yue and Mark Grosenbaugh for stimulating discussions.

Design Laboratory manager Mike Drooker always made sure we had the best possible work environment.

Séamus Tuohy provided the computer graphics software displaying the simulations. It made my work visually as well as intellectually stimulating.

Tom Korsmeyer was of great help in adapting his $O(N)$ code to my problem.

Throughout my years in school I have had many teachers, and I would like to thank those that went to extraordinary lengths to present their material with clarity and consistence. This goes all the way back to Mrs. Snekvik in first grade who had to pull my hair to make me realize the importance of starting sentences with capital letters. There are too many to mention, but you know who you are, and you should know that your efforts are appreciated as an inspiration for students long after they leave the classroom.

MIT and WHOI are exciting places to be, and if it was possible, I would thank all those that have made them what they are. In particular, I have enjoyed digging around in the MIT Libraries, and Toscanini's Ice Cream is the campus coffee authority.

To all the friends that I have made in America, you made my stay such a joy. Kymberlee Keckler is a sweetheart and helped correct my writing, but she is not to be held accountable for poor English and other mistakes.

My parents always supported the decisions I made about my life, I am forever grateful for their understanding.

Contents

1 Introduction **10**

1.1 The concept 10

1.2 Methods of investigation 12

2 Linear theory **14**

2.1 Introduction 14

2.2 The von Kármán vortex street 15

2.3 The no–wake vorticity distribution on the foil 19

2.4 Vorticity caused by the wake 24

2.5 Lift 25

2.6 Moment 27

2.7 Leading edge suction and thrust 27

2.8 Foil performance and input parameters 30

3 A numerical procedure for vortex flow over a Joukowski profile **37**

3.1 Introduction 37

3.2 Coordinate systems 38

3.3 Conformal mapping 40

3.4 Boundary value problem for translating and rotating section 42

3.5 Vortex potentials 46

3.6 Vortex convection and vortex shedding algorithm 48

3.7 Pressure in a rotating and translating coordinate frame 52

3.8 Force 55

3.9 Moment 62
3.10 Comments 71

4 Simulation Results **72**
4.1 A comparison with experiment for uniform inflow 72
4.1.1 Experimental run "nov1413" 74
4.1.2 Experimental run "nov2916" 77
4.1.3 Very high efficiency runs 79
4.2 How the oncoming vortex street is generated in numerical simulation 80
4.3 Comparison with a vortex – foil interaction experiment 82
4.4 Simulation results 86

5 The dynamics of shear layer – vortex interaction **95**
5.1 Vortex mixing in the wake of an oscillating foil 95
5.2 Convergence of vortex methods 98
5.3 Simulation results 101
5.4 The significance of shear layer instability 110

6 Conclusions **114**
6.1 Summary of main results 114
6.2 Recommendations for future work 115

A The fast vortex method **116**
A.1 Introduction 116
A.2 The multipole expansion method 119
A.3 Adaptation to Joukowski foil simulations 122
A.4 Adaptation to periodic boundary conditions 127

List of Figures

1-1 Examples of foil–vortex interaction. 11

2-1 The model problem. 14
2-2 Geometry of the Kármán vortex street. 16
2-3 Encounter frequency for the vortex street. 19
2-4 Velocity in Kármán vortex street. 20
2-5 Flow for leading edge suction analysis. 28
2-6 Energy recovery factor for stationary foil in vortex street. $\kappa/(Uc) = 0.1$. 33
2-7 Energy recovery factor for stationary foil in vortex street. $\kappa/(Uc) = 0.4$. 33
2-8 Energy recovery factor for stationary foil in vortex street. $\kappa/(Uc) = 1.0$. 34
2-9 Thrust coefficient for a stationary foil in a vortex street with $\kappa/(Uc) = 0.1$ 34
2-10 Energy recovery for oscillating foil for $\kappa/(Uc) = 0.4$, $p/c = 4$, $q/c = 1$. 35

3-1 Definition of coordinate systems. 38
3-2 Mapping between Joukowski profile and circle. 40
3-3 Definitions for boundary value problem. 42
3-4 Streamlines of the unit velocity potentials. From top to bottom: w_1, w_2 and w_3. 47
3-5 Vortex shedding algorithm. 49
3-6 Circulation around an impulsively started flat plate normalized by its steady state value. 52
3-7 Pressure distribution at three different times for an impulsively started foil. 54
3-8 Integration contour for force. 56

3-9 Typical time history of sum in brackets in equation (3.36) for two different time steps, $\Delta t = 0.4$ and $\Delta t = 0.1$. 61
3-10 Forces on an impulsively started flat plate. 63
3-11 Integration contour for moment. 66
3-12 Moment on an impulsively started flat plate normalized by its steady state value, $\pi U^2 c^2 \alpha_0$. 70

4-1 Experimental rig for oscillating foil. 73
4-2 Profile shapes. 74
4-3 Force and moment records. 75
4-4 Force and moment records. 78
4-5 Experimentally obtained velocity field of incoming vortex street. . . . 83
4-6 Incoming vortex street for numerical simulation. 84
4-7 Wake velocity field for foil alone. 85
4-8 Foil path and streamlines as seen by an observer moving with the Kármán vortex street.Solid path: $\phi = 0$, dashed path: $\phi = \pm\pi$. 86
4-9 Vortex interaction. 87
4-10 Combined wake velocity fields. 88
4-11 Instantaneous and averaged thrust for Case 1, $\phi = 0.1$. 89
4-12 Hydrodynamic performance for Case 1. 90
4-13 Hydrodynamic performance for Case 2. Legend in Figure 4-12. 90
4-14 Hydrodynamic performance for Case 3. Legend in Figure 4-12. 91
4-15 Hydrodynamic performance for Case 4. Legend in Figure 4-12. 91
4-16 Hydrodynamic performance for Case 5. Legend in Figure 4-12. 92
4-17 Hydrodynamic performance for Case 6. Legend in Figure 4-12. 93
4-18 Hydrodynamic performance for Case 7. Legend in Figure 4-12. 93
4-19 Hydrodynamic performance for Case 8. Legend in Figure 4-12. 93

5-1 Initial configuration for model problem. 96
5-2 Initializing the vortex method. 100
5-3 $I_p(t)$ for $R/b = 4$ and $\Gamma_p/\Gamma_s = 1$. 103

5-4 $I_p(t)$ for $R/b = 4$ and $D/b = 2$. 103
5-5 $I_p(t)$ for $D/b = 2$ and $\Gamma_p/\Gamma_s = 1$. 104
5-6 Case 2 106
5-7 Case 4 107
5-8 Case 8 108
5-9 Case 9 109
5-10 Exact and approximate velocity profiles for the shear layer. 110
5-11 Growth rates for linear instabilities on the shear layer. 111
5-12 Deflection of the shear layer for Case 4. 112
5-13 Case 9 with disturbances added to the shear layer. 113
5-14 Evolution of vortex patch polar moment when the shear layer is disturbed. 113

A-1 Typical vortex distribution and box tree for foil simulation. 123
A-2 Moving the box tree to accommodate a multipole. 124
A-3 Setting the maximum level. 125
A-4 How periodic boundary conditions are treated. 127
A-5 Execution times for periodic boundary conditions. 131

Chapter 1

Introduction

1.1 The concept

This thesis is an investigation of foil–vortex interaction in the context of high efficiency propulsion. The canonical model problem is shown in Figure 1-1a, where an oscillating hydro– or aerofoil is located in the wake of a bluff body. Such a wake is often highly organized, with distinct and concentrated regions of positive and negative vorticity. The presumption of this study is that the unsteadiness of the inflow to the foil can be exploited to yield a high propulsive efficiency. Unsteady inflow causes a degradation in the performance of traditional propulsors, whereas a flapping foil may perform *better* under such conditions, by controlling the incoming vortices.

The inspiration for this problem comes from biofluiddynamics, where flow visualizations [58] indicate that the flapping tail of a fish may recover some of the energy in vortices formed over the anterior parts of the body, Figure 1-1b. This prompted my advisor, Professor Triantafyllou, to propose the fish swimming mode of propulsion for Autonomous Underwater Vehicles, which must move about very efficiently to conserve energy from a limited power supply. A vehicle equipped with such propulsor would have the additional benefit of being highly maneuverable, as demonstrated by many fish. This would be an important attribute during operations in constrained quarters.

The term Blade–Vortex Interaction normally refers to the problem in Figure 1-1c,

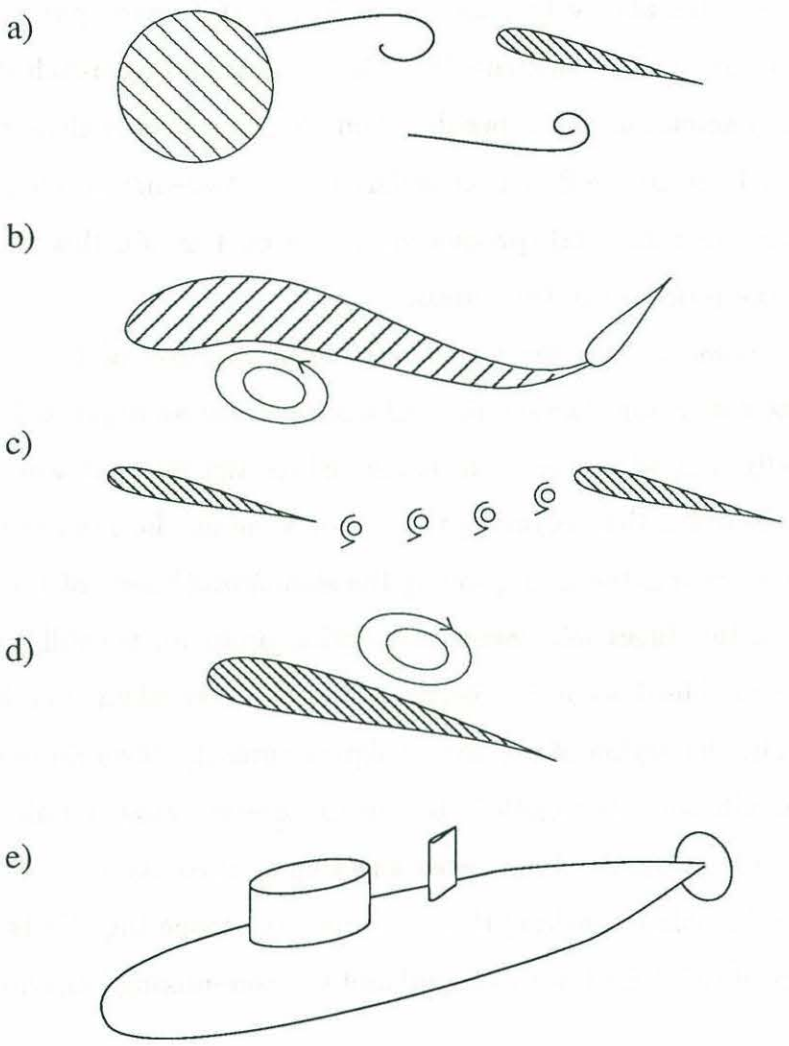

Figure 1-1: Examples of foil–vortex interaction.

which has been widely studied in the aviation community. A helicopter in powered descent will produce a vortex wake behind each rotor blade that impinges on the following blade, resulting in pressure fluctuations and noise [37, 25, 53, 74]. These studies are therefore not concerned with the overall forces on the foil.

One example of constructive foil–vortex interference is the so called Kasper foil, Figure 1-1d, where the ability to trap a vortex in a stationary position above the foil results in enormous lift coefficients [61, 36]. The natural approach in this case is to look for steady solutions to the problem and then investigate their stability with a linearized model. Since the flow is considered to be two–dimensional, steady, and inviscid, there are no horizontal (propulsive) forces on the foil, this being the main difference from the problems in this thesis.

Figure 1-1e shows an idea for an alternative application of the vortex control principle. To the extent that the sail of a submarine sheds an organized vortex wake, a foil strategically located downstream could reduce the unsteadiness of the wake. Perhaps more important than reducing the overall drag on the submarine is the fact that the *wake signature* is lower, improving the stealthworthiness of the submarine.

In addition to the direct foil–vortex interaction problem, we will also study the dynamics of the combined wake in isolation. The model problem is an infinite shear layer next to a circular region of oppositely signed vorticity. Two finite core vortices of opposite sign will not mix together, but in the present case, a finite core vortex is paired with a vortex sheet. The vortex sheet spontaneously rolls up and engulfs fluid particles in its vicinity, making this a problem of competing effects between the natural tendency of the shear layer to engulf and the non–mixing behavior of opposite sign vortices.

1.2 Methods of investigation

Several problems related to Foil–Vortex Interaction are considered in this thesis, but they all share the assumption of inviscid two–dimensional flow. This is not to suggest that viscous or three–dimensional effects are unimportant, but the reduced compu-

tational effort in the simpler method is a great advantage in the investigation of the rather large parameter space. When the most interesting cases have been identified, it will be appropriate to employ a more realistic computational method.

First, a method based on the classical linear theory of airfoils in nonuniform motion is adapted to handle a combination of unsteady inflow and foil oscillations. The formulation of Sears and von Kármán [79, 67] is well suited to this problem, because it can handle both incoming flow disturbances and foil motion, and can readily be extended to find thrust force.

The bulk of the thesis is concerned with numerical simulations of the problem, permitting arbitrary foil motion and inflow vorticity. Here we consider the foil shape to be a Joukowski profile, and the vorticity field is represented by point vortices. By conformal mapping we are able to satisfy the body boundary conditions exactly and express the convection velocities of the vortices. A fast multipole expansion method is used to step the solution forward in time. An important part is to calculate the reaction forces on the foil, and the necessary integrations can be carried out analytically, leading to closed form expressions for the force and moment.

The wake dynamics is investigated by means of the vortex method with finite size computational elements. Here, the fast interaction computations have been adapted to periodic boundary conditions.

Chapter 2

Linear theory

2.1 Introduction

In this chapter we shall employ the well known linear unsteady foil theory to the problem of an oscillating foil placed in a Kármán vortex street seen in Figure 2-1. The usual restrictions of of this theory apply: the flow is assumed two-dimensional and inviscid, the Kutta condition of smooth flow at the trailing edge holds, and the deviations from a uniform flow are small enough to allow the boundary conditions on the foil to be projected onto its mean position and the wake to be modeled as a flat vortex sheet convecting with the free stream.

We will show that the velocity field at the centerline of a Kármán vortex street can be modeled as a sinusoidal gust, under certain conditions. This allows the upwash on a foil at a fixed location to be described as a Fourier series in the arccosine of the position along the chord. Another such series, corresponding to the heave and

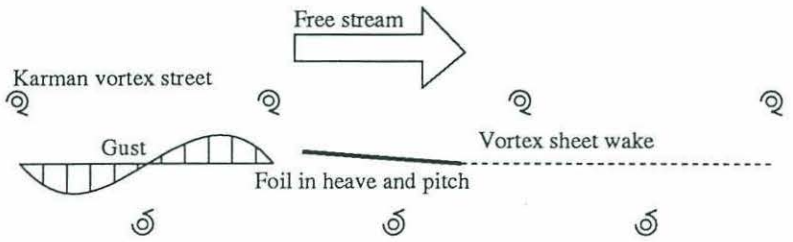

Figure 2-1: The model problem.

pitch motion of the foil in an otherwise uniform flow, can be constructed and added. This yields a description of the total relative upwash on the foil, neglecting the wake influence. By the results due to Glauert [26], the corresponding vorticity distribution may be written down immediately in the form of another series, without solving the integral equation. The first 4 coefficients of the no–wake vorticity series is all that is needed in the subsequent analysis of the wake influence.

Linear theory for a foil in nonuniform motion or inflow was a subject of intense study during the first decades of human fight, because of its importance to aeroelastic response. This effort culminated with two papers by Sears and von Kármán[1] [79, 67], and the interested reader is strongly encouraged to consult these references. We shall recapitulate the parts of their work that pertain to our problem, with one important extension. Since we are interested in the performance of the foil as a propulsive device, it is necessary to determine the horizontal force, which depends in large part on leading edge suction. Therefore, we show how to determine leading edge suction from the vorticity distribution, and apply that knowledge in the linear theory. Finally, the thrust and input power are averaged over one period, so that the propulsive performance may be assessed. This chapter also serves to define the relevant performance criteria, as well as the nondimensional groups that form the input parameters to the problem.

2.2 The von Kármán vortex street

The Kármán vortex street is an ideal flow model for the wake downstream of a bluff body. Mallock [46], in 1907, was the first to report observations on the regular vortex pattern behind bluff bodies in a uniform flow at intermediate Reynolds numbers. This striking phenomenon is one of the most studied in all of fluid mechanics; much of the earlier research is reviewed in Goldstein [27]. At a suitable distance downstream, the wake may be modeled as two infinite rows of discrete vortices in an otherwise

[1]The influence of these papers on the development of nonlinear theories was recently reviewed by McCune and Tavares [48].

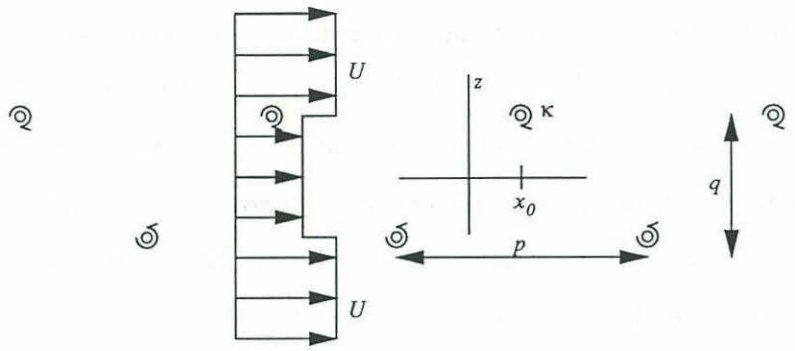

Figure 2-2: Geometry of the Kármán vortex street.

irrotational flow, arranged as shown in Figure 2-2. The purpose of this section is to approximate the resulting velocity field in a way that facilitates the use of linear theory.

Milne Thomson [75] shows how to construct a closed form expression for the potential due to a single row of vortices, and two such rows can be added to a free stream of velocity U, giving the desired velocity potential:

$$w = Uz + i\kappa \left[\log \sin \frac{\pi(z - iq/2 - x_0)}{p} - \log \cos \frac{\pi(z + iq/2 - x_0)}{p} \right]$$

where x_0 is the abscissa of a vortex in the upper row.

The corresponding velocity field is obtained by taking the z derivative:

$$u - iv = U + \frac{i\pi\kappa}{p} \left[\frac{\cos \frac{\pi(z-iq/2-x_0)}{p}}{\sin \frac{\pi(z-iq/2-x_0)}{p}} - \frac{\sin \frac{\pi(z+iq/2-x_0)}{p}}{\cos \frac{\pi(z+iq/2-x_0)}{p}} \right]$$

One feature of interest is the velocity field that is obtained by averaging over one period in the x direction. Consider first a single vortex row with a vortex located at the origin. It has the potential:

$$w(z) = i\kappa \log \sin \frac{\pi z}{p}$$

Now the average velocity can be found from the difference in potential at two points,

one period apart:

$$\begin{aligned} < u > -i < v > &= \frac{1}{p}[w(p/2+iy) - w(-p/2+iy)] \\ &= \frac{i\kappa}{p} \log\left[\frac{\sin(\pi(1/2+iy/p)}{\sin(\pi(-1/2+iy/p)}\right] \\ &= \frac{i\kappa}{p}\log(-1) \end{aligned}$$

It remains to decide the proper branch of $\log(-1)$. For large positive values of y, we know that the flow has a uniform velocity $\pi\kappa/p$ and for large negative y it is $-\pi\kappa/p$. This corresponds to the two branches $\log(-1) = -i\pi$ and $\log(-1) = i\pi$, respectively. The flow is continuous everywhere except at the vortices, so the change in branch must take place at $y = 0$. We may therefore conclude that the average velocity field due to a single row of vortices is given by:

$$< u > -i < v >= \begin{cases} \pi\kappa/p & \text{if } y > 0 \\ -\pi\kappa/p & \text{if } y < 0 \end{cases}$$

The averaging process is a linear one, consequently the average velocity due to a free stream and two vortex rows constituting the Kármán vortex street is written down by simple superposition:

$$< u > -i < v >= \begin{cases} U & \text{if } |y| > q/2 \\ U - 2\pi\kappa/p & \text{if } |y| < q/2 \end{cases} \tag{2.1}$$

It is interesting to note that $< u > -i < v >$ corresponds to the steady velocity field that would result if the vorticity in the point vortices was distributed into two shear layers of zero thickness, as indicated in Figure 2-2.

The vortex street convects in the x direction with a constant velocity given by:

$$U_c = U - \frac{\pi\kappa}{p}\tanh\frac{\pi q}{p} \tag{2.2}$$

Thus, $< u > -i < v >$ can be considered time averaged velocities at a fixed location.

By the same token, the value of x_0 is a function of time:

$$x_0 = U_c(t - t_0) \tag{2.3}$$

i.e. the vortex street is drifting downstream with a vortex passing the y-axis in the upper half plane at a time t_0. The time t_0 determines the phase between the foil motion and the inflow fluctuations, and is therefore an important input parameter to the problem. Now, substituting (2.3) in (2.2), we obtain an expression for the velocity field as a function of both space and time:

$$u - iv = U + \frac{i\pi\kappa}{p}\left[\frac{\cos\frac{\pi(z-iq/2-U_c(t-t_0))}{p}}{\sin\frac{\pi(z-iq/2-U_c(t-t_0))}{p}} - \frac{\sin\frac{\pi(z+iq/2-U_c(t-t_0))}{p}}{\cos\frac{\pi(z+iq/2-U_c(t-t_0))}{p}}\right]$$

Next we make an approximation based on the small amplitude assumption of the linear theory. We consider the velocity fluctuations in the inflow to the foil to be independent of y, by replacing z by x. This will hold only as long as the foil motion amplitude is small compared to q. Now:

$$u - iv = U - \frac{2\pi\kappa}{p}\frac{\cosh\frac{\pi q}{p}}{\sinh\frac{\pi q}{p} - i\sin\omega(t - x/U_c - t_0)}$$

Thus, the velocity field caused by the Kármán vortex street have been replaced by a vertical gust independent of y. The encounter frequency, ω, is given by:

$$\omega = \frac{2\pi U_c}{p} \tag{2.4}$$

and is shown as a contour plot versus p and κ in Figure 2-3. Here, $U = q = 1$, which is equivalent to making ω, p and κ nondimensional with U/q, q, and Uq, respectively. It is evident that ω is uniquely determined from p and κ, but if ω and κ is thought of as independent variables, there can be none, one, or two solutions for p. This point will be raised again in Chapter 4.

In Figure 2-4, u and v are shown for different ratios q/p. As the ratio between the width and the spatial period, q/p, becomes larger, we note that the fluctuations

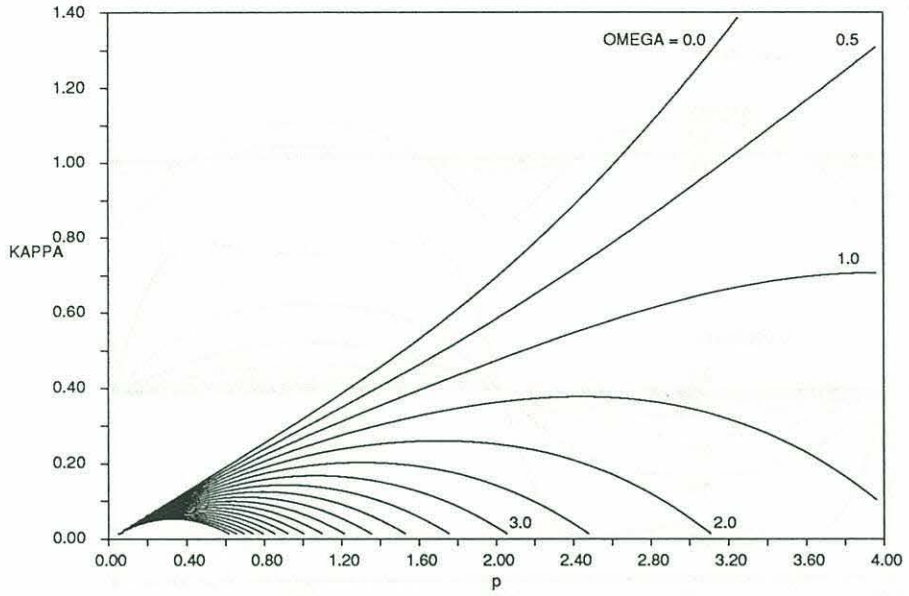

Figure 2-3: Encounter frequency for the vortex street.

in u decay faster than the fluctuations in v. We also see that the fluctuations in v become more sinusoidal for larger q/p. We now make one assumption in addition to those of linear theory; namely that q/p is large enough for u and v to be accurately described with only one component of their Fourier series:

$$u = U - \frac{2\pi\kappa}{p} \tag{2.5}$$

$$v = \frac{2\pi\kappa}{p\cosh\frac{\pi q}{p}}\sin\omega(t - x/U_c - t_0) \tag{2.6}$$

Actually, the amplitude of v is not a formally computed Fourier coefficient, but a simpler factor obtained by matching values at $\omega(t - x/U_c - t_0) = \pi/2$. In the limit of large q/p, they are the same. A more refined theory could be built up by using higher order Fourier terms to describe the velocity field more accurately.

2.3 The no–wake vorticity distribution on the foil

In the linear theory as formulated by von Kármán and Sears, the only information that is needed about the foil motion and the vertical gust, is a description of the no–wake vorticity distribution along the foil, denoted $\gamma_0(x)$. "No–wake", means simply

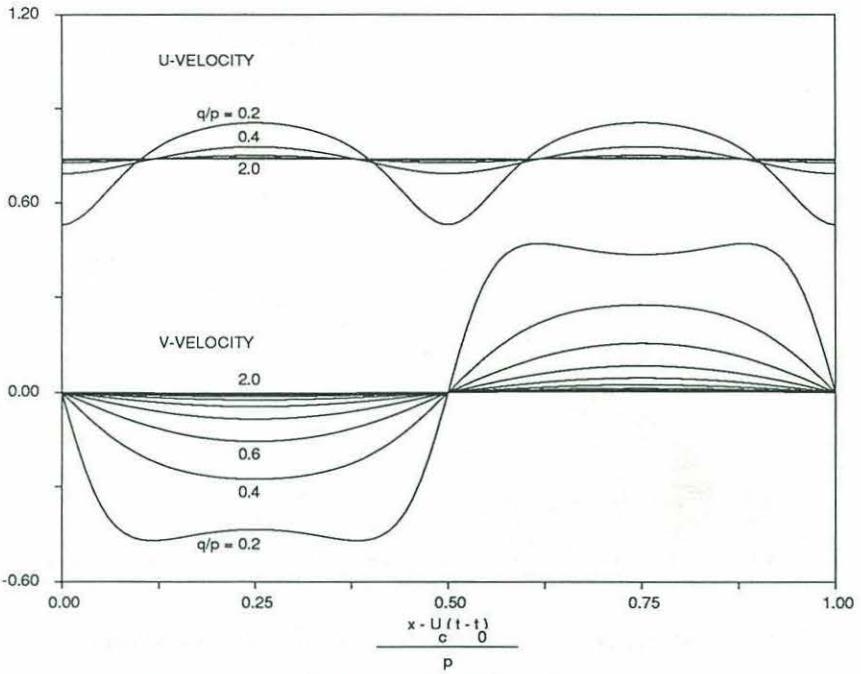

Figure 2-4: Velocity in Kármán vortex street.

that the influence of the foil's own wake is neglected. By virtue of an ingenious device due to Glauert [26], $\gamma_0(x)$ can be obtained immediately from the relative no–wake upwash (normal fluid velocity at an imaginary surface replacing the foil), part of which we found in the previous section.

The first step in this process is to define a new coordinate θ for the chordwise location:

$$x = c\cos\theta \tag{2.7}$$

so that θ runs from 0 at the trailing edge to π at the leading edge on a foil of length $2c$.

The no–wake upwash on the foil, as seen by an observer fixed in the foil, is then expressed as a series in θ:

$$v_0 = U_0 \left[A_0 + 2\sum_{n=1}^{\infty} A_n \cos n\theta \right] e^{i\omega t} \tag{2.8}$$

Here, we have restricted attention to harmonic time dependence, the real part of the right hand side being implied, but this is not necessary in general. For the free

stream, U_0, we take the average velocity in the vortex street (2.6):

$$U_0 = U - \frac{2\pi\kappa}{p} \tag{2.9}$$

Now, in order that the body boundary condition be satisfied, a vortex distribution γ_0 (positive clockwise) is necessary, satisfying the integral equation:

$$v_0(x,t) + \int_{-c}^{c} \frac{\gamma_0(x',t)}{2\pi(x-x')} dx' = 0 \tag{2.10}$$

This equation states that the upwash and vortex distribution must result in a zero relative normal velocity on the foil. The typical vortex element has clockwise circulation $\gamma_0 dx$, so the notation is different from the other chapters by a factor $1/(2\pi)$.

By virtue of the Glauert integrals:

$$\int_0^{\pi} \frac{\cos n\phi}{\cos\phi - \cos\theta} d\phi = \pi \frac{\sin n\theta}{\sin\theta} \tag{2.11}$$

it is straightforward to verify that

$$\gamma_0 = 2U_0 \left[A_0 \frac{1-\cos\theta}{\sin\theta} + 2\sum_{n=1}^{\infty} A_n \sin n\theta \right] e^{i\omega t} \tag{2.12}$$

is a solution to the problem. This particular solution has the property that $\gamma_0(x = c) = 0$, which means that the Kutta condition is satisfied at the trailing edge. The problem is now reduced to finding the coefficients that describe v_0, which has has two contributions; the relative upwash due to foil heave and pitch, and the incoming gust.

The upwash due to heave and pitch is conveniently formulated in the notation of Lighthill [44], where a flat plate heaving with amplitude h_0 and pitching about a point b with amplitude α_0, has a vertical displacement given by:

$$y = [h_0 - i\alpha_0(x-b)]e^{i\omega t}$$

We assume that the frequency of foil motion equals the encounter frequency, such that a steady harmonic response results. The resulting upwash is due both to the

vertical velocity of the foil and the angle of incidence with the free stream:

$$v_0 = \{-i\omega[h_0 - i\alpha_0(x-b)] - i\alpha_0 U_0\}\, e^{i\omega t}$$

Substitution of (2.7) yields a description of the desired form (2.8).

The vertical gust velocity must be put in the form (2.8) and added. (2.6) may be written:

$$v_0 = V_g e^{i\omega[t - x/U_c]}$$

where V_g is the complex gust amplitude:

$$V_g = -\frac{2\pi i \kappa e^{-i\omega t_0}}{p \cosh \frac{\pi g}{p}} \tag{2.13}$$

Using the new coordinate θ, we have

$$v_0 = V_g e^{i\omega t} e^{-i\sigma_c \cos\theta}$$

Here, σ_c is the reduced frequency of the gust,

$$\sigma_c = \frac{\omega c}{U_c} \tag{2.14}$$

At this point we should note that there are three different reduced frequencies in this problem. Apart from σ_c, which is based on the convection velocity of the Kármán vortex street (i.e. the velocity of the inflow disturbance), we define reduced frequencies based on the mean velocity inside and outside the vortex street, respectively:

$$\sigma_0 = \frac{\omega c}{U_0} \tag{2.15}$$

$$\sigma = \frac{\omega c}{U} \tag{2.16}$$

From the theory of Bessel functions it can be found that

$$e^{-i\sigma_c \cos\theta} = J_0(\sigma_c) + 2\sum_{n=1}^{\infty}(-i)^n J_n(\sigma_c)\cos n\theta$$

See for instance equations (9.1.21), (9.1.44), (9.1.45) of Abramowitz and Stegun [1]. Thus we have the desired form of the vertical gust:

$$v_0 = V_g\left[J_0(\sigma_c) + 2\sum_{n=1}^{\infty}(-i)^n J_n(\sigma_c)\cos n\theta\right]e^{i\omega t}$$

The total upwash due to heave, pitch and gust is now given as:

$$v_0 = \left\{-i\omega[h_0 - i\alpha_0(c\cos\theta - b)] - i\alpha_0 U_0 + V_g J_0(\sigma_c) + 2V_g\sum_{n=1}^{\infty}(-i)^n J_n(\sigma_c)\cos n\theta\right\}e^{i\omega t}$$

It will turn out that only the 4 first coefficients of the Glauert series (2.8) are needed, these are:

$$A_0 = \omega\alpha_0 b/U_0 - i\omega h_0/U_0 + i\alpha_0 + V_g J_0(\sigma_c)/U_0 \tag{2.17}$$

$$A_1 = -\alpha_0\sigma/2 - iV_g J_1(\sigma_c)/U_0 \tag{2.18}$$

$$A_2 = -V_g J_2(\sigma_c)/U_0 \tag{2.19}$$

$$A_3 = iV_g J_3(\sigma_c)/U_0 \tag{2.20}$$

We shall need to know the no–wake foil circulation, which can be found by integrating γ_0 over the length of the foil:

$$\Gamma_0(t) = \int_{-c}^{c}\gamma_0(x,t)dx = G_0 e^{i\omega t} \tag{2.21}$$

Using the Glauert series representation we readily find:

$$G_0 = 2\pi U_0 c(A_0 + A_1) \tag{2.22}$$

2.4 Vorticity caused by the wake

Having completed the discussion of the no–wake vorticity γ_0, we turn to a description of the influence of the wake as presented by von Kármán and Sears [79]. They denote the wake vorticity $\gamma(\xi, t)$ where ξ is the coordinate of a point in the wake. Therefore, $\gamma(x, t)$ and $\gamma(\xi, t)$ signify bound and free vorticity, respectively. An infinitesimal segment of the wake has clockwise circulation $\gamma(\xi, t)d\xi$. Through conformal mapping and the circle theorem[2], the foil vorticity $\gamma_1(x, t)$ caused by an element of the wake can be determined. Integration over all $\xi \in (c, \infty)$ yields the bound vorticity caused by the wake:

$$\gamma_1(x,t) = \sqrt{\frac{c-x}{c+x}} \int_c^\infty \frac{\gamma(\xi,t)}{\pi(\xi - x)} \sqrt{\frac{\xi + c}{\xi - c}}\, d\xi \tag{2.23}$$

A circulation has been added that keeps the velocity from becoming infinite at the trailing edge. Consequently, the complete vorticity distribution on the foil,

$$\gamma(x,t) = \gamma_0(x,t) + \gamma_1(x,t) \tag{2.24}$$

satisfies the Kutta condition.

In linear theory, the condition of continuous pressure in the wake implies that the vorticity in the wake convects with the free stream. In the harmonic case, this condition takes the form:

$$\gamma(\xi,t) = g e^{i\omega(t - \xi/U_0)} \tag{2.25}$$

The purpose of this section is to determine the complex wake strength, g, by invoking Kelvin's theorem. Once g is found in terms of the Glauert coefficients, $\gamma(x, t)$ follows from (2.23) and (2.24).

First, consider the wake induced circulation around the foil:

$$\begin{aligned} \Gamma_1(t) &= \int_{-c}^{c} \gamma_1(x,t)dx \\ &= \int_{-c}^{c} dx \sqrt{\frac{c-x}{c+x}} \int_c^\infty d\xi\, \frac{\gamma(\xi,t)}{\pi(\xi - x)} \sqrt{\frac{\xi + c}{\xi - c}} \end{aligned}$$

[2]These techniques are explained in the next chapter.

Substituting (2.7) and using two known trigonometric integrals [14], we can carry out the integration in x:

$$\Gamma_1(t) = \int_c^\infty \gamma(\xi, t) \left[\sqrt{\frac{\xi + c}{\xi - c}} - 1 \right] d\xi \tag{2.26}$$

Now, since the time dependence is harmonic, $\Gamma_1(t) = G_1 e^{i\omega t}$, and $\gamma(\xi)$ has the form (2.25). It can be shown that the integral is a combination of modified Bessel functions of the second kind (see 8.432.3 of Gradshteyn & Ryzhik [29] and [79]):

$$\begin{aligned} G_1 &= g \int_c^\infty d\xi \left[e^{-i\sigma_0 \xi / c} \sqrt{\frac{\xi + c}{\xi - c}} - 1 \right] \\ &= gc \left[K_0(i\sigma_0) + K_1(i\sigma_0) - \frac{e^{-i\sigma_0}}{i\sigma_0} \right] \end{aligned} \tag{2.27}$$

Kelvin's theorem states that the total vorticity in the fluid must remain zero at all times, or equivalently that the rate of change of circulation about the foil is matched by the vorticity that is shed into the free stream. Hence,

$$\begin{aligned} \frac{d(\Gamma_0 + \Gamma_1)}{dt} &= -U_0 \gamma(\xi = c) \\ &\Downarrow \\ i\omega(G_0 + G_1) &= -U_0 g e^{-i\sigma_0} \\ &\Downarrow \\ g &= \frac{-G_0/c}{K_0(i\sigma_0) + K_1(i\sigma_0)} \\ &\Downarrow \\ g &= \frac{-2\pi U_0 (A_0 + A_1)}{K_0(i\sigma_0) + K_1(i\sigma_0)} \end{aligned} \tag{2.28}$$

So the complex wake strength depends only on the two first Glauert coefficients and is modified by a factor that is a function of the reduced frequency σ_0.

2.5 Lift

Due to Kelvin's theorem, the vorticity distribution along the foil and the wake has zero net strength, and can be considered to consist of pairs of equal but opposite

vortex elements. From the fact that the momentum associated with such a pair of vortices is given by the product of their strength and the distance between them, the following expression holds for the vertical momentum of the fluid:

$$I = \int_{-c}^{c} x\gamma(x,t)dx + \int_{c}^{\infty} \xi\gamma(\xi,t)d\xi$$

Here, it is assumed that the fluid density is unity. With (2.24) and (2.23) we get:

$$I = \int_{-c}^{c} x\gamma_0(x,t)dx + \int_{c}^{\infty} \gamma(\xi,t)\sqrt{\xi^2 - c^2}d\xi$$

The lift force on the foil is given by the rate of change in the vertical fluid momentum, which must be evaluated with some care because the wake is continually growing. The end result is [79]):

$$l(t) = -\frac{dI}{dt} = -\frac{d}{dt}\int_{-c}^{c} x\gamma_0(x,t)dx + U_0\Gamma_0(t) + U_0\int_{c}^{\infty} d\xi\frac{\gamma(\xi,t)}{\sqrt{\xi^2 - c^2}} \tag{2.29}$$

The three terms in this expressions may be interpreted as apparent mass, quasisteady lift and wake effect, respectively.

This method of finding the reaction force on the foil, the Kelvin impulse method, is different from the method in Chapter 3, where we perform the integration of pressure on the foil surface.

Now, with $l(t) = Le^{i\omega t}$,

$$\begin{aligned} L &= -i\omega\int_{-c}^{c} xg_0(x)dx + U_0G_0 + U_0cg\int_{c}^{\infty}\frac{e^{-i\sigma_0\xi/c}}{\sqrt{\xi^2 - c^2}}d\xi \\ &= i\pi\omega U_0c^2(A_0 - A_2) + 2\pi U_0^2c(A_0 + A_1) - 2\pi U_0^2c(A_0 + A_1)\frac{K_0(i\sigma_0)}{K_0(i\sigma_0) + K_1(i\sigma_0)} \\ &= i\pi\sigma_0U_0^2c(A_0 - A_2) + 2\pi U_0^2c(A_0 + A_1)C(\sigma_0) \end{aligned} \tag{2.30}$$

In the last step, we introduced the Theodorsen function:

$$C(\sigma_0) = \frac{K_1(i\sigma_0)}{K_0(i\sigma_0) + K_1(i\sigma_0)} \tag{2.31}$$

2.6 Moment

Similarly, the counterclockwise moment about $z = 0$ may be found by considering the rate of change of moment of momentum. The analysis is somewhat more involved, the final result is [79]):

$$M = i\pi\sigma_0 U_0^2 c^2 \frac{A_1 - A_3}{4} + \pi U_0^2 c^2 \left[-A_0 C(\sigma_0) + A_1(1 - C(\sigma_0)) + A_2\right] \tag{2.32}$$

2.7 Leading edge suction and thrust

In a real flow, the leading edge of a foil must be rounded to permit good hydrodynamic performance. The flow here is fast, but finite, which causes a drop in pressure and a force with a forward component. Linear theory on the other hand, which assumes that the foil has zero thickness, allows a singularity in the potential at the leading edge. The pressure singularity, although acting over a portion of the foil of zero area, has associated with it a finite forward force component, the leading edge suction. The leading edge suction can be thought of as the limiting case for the force on a rounded leading edge as the radius of curvature shrinks, neglecting real flow phenomena like separation and cavitation. We will show here how to obtain the leading edge suction when the behavior of $\gamma(x)$ is known.

For this purpose, we can consider the leading edge to be the end of a semi–infinite flat plate with the flow shown in Figure 2-5. Let $z = re^{i\theta}$ be a complex plane coordinate system with origin at the end of the plate. The complex potential can be found from conformal mapping onto a half space:

$$\begin{aligned} w(z) &= Q\sqrt{z} \\ &= Q\sqrt{r}\left(\cos\frac{\theta}{2} + i\sin\frac{\theta}{2}\right) \end{aligned}$$

If the amplitude, Q, is a function of time, the pressure field has a term

$$-\frac{\partial\phi}{\partial t} = -\frac{dQ}{dt}\sqrt{r}\cos\frac{\theta}{2}$$

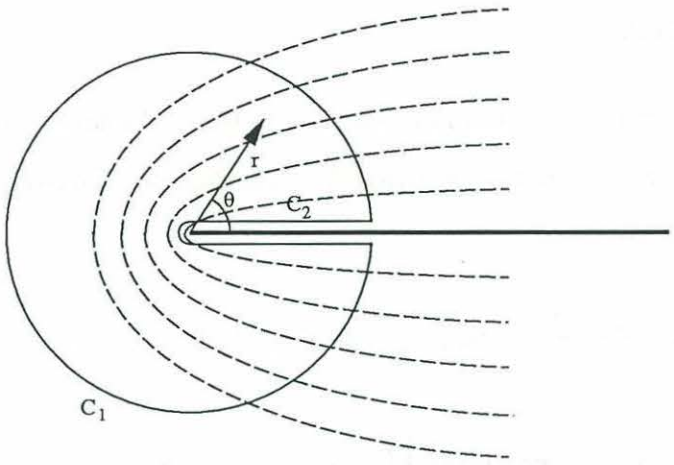

Figure 2-5: Flow for leading edge suction analysis.

This term vanishes at the end of the plate and does not contribute to the leading edge suction. Consequently, the flow can be considered steady. The velocity field is given by:

$$u - iv = -\frac{Q}{2\sqrt{z}} = -\frac{Q}{2\sqrt{r}}[\cos\frac{\theta}{2} - i\sin\frac{\theta}{2}]$$

resulting in the following vorticity distribution near the leading edge:

$$\gamma = u(\theta = 0) - u(\theta = 2\pi) = \frac{Q}{\sqrt{x}}$$

The balance of momentum for the control volume enclosed by $C_1 + C_2$ in Figure 2-5 can be written:

$$\int_{C_1+C_2} p\,\mathbf{n}\,ds = \int_{C_1+C_2} \mathbf{u}u_n ds \tag{2.33}$$

The leading edge suction, s, is given by the x component of this equation.

$$\begin{aligned} s &= \int_{C_2} pn_x dl \\ &= \int_{C_1+C_2} uu_n dl - \int_{C_1} pn_x dl \end{aligned}$$

On C_1, $p = \frac{1}{2}(u^2 + v^2)$ is constant, and on C_2, $u_n = 0$. C_1 is a circle of radius R, and here:

$$u_n = u\cos\theta + v\sin\theta = \frac{Q}{2\sqrt{R}}\cos\frac{\theta}{2}$$

We are left with:

$$\begin{aligned} s &= \int_{c_1} u u_n ds \\ &= \int_0^{2\pi} \frac{Q}{2\sqrt{R}} \cos\frac{\theta}{2} \; \frac{Q}{2\sqrt{R}} \cos\frac{\theta}{2} \, R \, d\theta \\ &= \frac{\pi Q^2}{4} \end{aligned}$$

Thus, at the leading edge, vorticity and suction are related through:

$$\gamma = \frac{Q}{\sqrt{x}} \qquad \Longleftrightarrow \qquad s = \frac{\pi Q^2}{4} \tag{2.34}$$

In our case, the singularity is located at $x = -c$, and $\gamma = \gamma_0 + \gamma_1$, where

$$\gamma_0(x,t) \sim 2\sqrt{2c} u_0 A_0 e^{i\omega t} (c+x)^{-1/2}, \text{ as } x \to -c^+$$

from (2.12), and

$$\begin{aligned} \gamma_1(x) &= \frac{g e^{i\omega t}}{\pi} \sqrt{\frac{c-x}{c+x}} \int_c^\infty d\xi \frac{e^{-i\sigma_0 \xi/c}}{\pi(\xi - x)} \sqrt{\frac{\xi + c}{\xi - c}} \\ &\sim \frac{\sqrt{2c} g e^{i\omega t}}{\pi\sqrt{c+x}} \int_c^\infty d\xi \frac{e^{-i\sigma_0\xi/c}}{\sqrt{\xi^2 - c^2}}, \text{ as } x \to -c^+ \\ &= \frac{\sqrt{2c} g e^{i\omega t} K_0(i\sigma_0)}{\pi\sqrt{c+x}} \\ &= -2\sqrt{2c} u_0 (A_0 + A_1) e^{i\omega t} \frac{K_0(i\sigma_0)}{K_0(i\sigma_0) + K_1(i\sigma_0)} (c+x)^{-1/2} \end{aligned}$$

from (2.23), (2.25), and (2.28).

We add these contributions and write the answer in terms of the Theodorsen function, explicitly specifying the real part to avoid confusion when squaring Q:

$$\gamma(x,t) \sim \sqrt{8c}\, U \, \mathrm{Re}\left\{ \left[A_0 C(\sigma_0) - A_1 (1 - C(\sigma_0)) \right] e^{i\omega t} \right\} (c+x)^{-1/2}, \text{ as } x \to -c^+$$

Leading edge suction is therefore given by:

$$s(t) = \left[\mathrm{Re}\left\{Se^{i\omega t}\right\}\right]^2 \tag{2.35}$$

where

$$S = \sqrt{2\pi c}U_0\left[A_0C(\sigma_0) - A_1(1 - C(\sigma_0))\right] \tag{2.36}$$

Instantaneous thrust, $T(t)$, also has a component due to the inclination of lift force, such that:

$$T(t) = \left[\mathrm{Re}\left\{Se^{i\omega t}\right\}\right]^2 + \mathrm{Re}\left\{Le^{i\omega t}\right\}\mathrm{Re}\left\{-i\alpha_0 e^{i\omega t}\right\} \tag{2.37}$$

So we see that in order to compute the force and moment acting on the foil in our problem, we need only the first 4 Glauert coefficients, which follow from the normal velocity of the inflow relative to the moving foil surface. Now we must determine the relevant performance criteria, as well as the input parameters.

2.8 Foil performance and input parameters

The rate of work, or power, that is needed to sustain the foil motion, is given by the negative lift force times the vertical velocity of the foil midpoint minus the counterclockwise moment times the counterclockwise angular velocity:

$$P(t) = -\mathrm{Re}\left\{Le^{i\omega t}\right\}\mathrm{Re}\left\{i\omega(h_0 + i\alpha_0 b)e^{i\omega t}\right\} - \mathrm{Re}\left\{Me^{i\omega t}\right\}\mathrm{Re}\left\{\omega\alpha_0 be^{i\omega t}\right\} \tag{2.38}$$

Given two harmonically oscillating quantities, Re $\{Ae^{i\omega t}\}$ and Re $\{Be^{i\omega t}\}$, the time average of their product is given by:

$$\frac{1}{2}\mathrm{Re}\left\{A\overline{B}\right\}$$

where the overline denotes complex conjugate. Using this, we determine the average

thrust and input power:

$$< T >= \frac{1}{2}\mathrm{Re}\left\{S\overline{S} + Li\alpha_0\right\} \tag{2.39}$$

$$< P >= \frac{1}{2}\mathrm{Re}\left\{L\omega(ih_0 - \alpha_0 b) - M\omega\alpha_0\right\} \tag{2.40}$$

The efficiency of the foil is given by:

$$\eta = \frac{< T > U}{< P >} \tag{2.41}$$

where U is the free stream velocity outside the Kármán vortex street. The efficiency can be made arbitrary high by letting the motion amplitudes h_0 and α_0 become small. An alternative way of assessing performance, is to consider the energy recovery. The incoming vortex street has a mean drag force associated with it [75]:

$$< D >= \omega\kappa q - 2\pi\frac{\kappa^2}{p}\left[1 - \tanh\frac{\pi q}{p}\right] \tag{2.42}$$

In order to propel the imaginary upstream body through the fluid, an average power

$$U < D >$$

is required. The foil recovers

$$U < T >$$

of this, but must spend

$$< P >$$

We define the energy recovery factor as the net gain divided by original power:

$$\eta_R = \frac{U < T > - < P >}{U < D >} \tag{2.43}$$

From the input parameters in the problem we can form 7 nondimensional groups

that define the parameter space, for instance:

$$\begin{aligned} & p/c \\ & \kappa/(Uc) \\ & q/c \\ & h_0/c \\ & b/c \\ \Theta &= \frac{\alpha_0 U}{\omega h_0} \\ \phi &= \omega t_0 \end{aligned} \tag{2.44}$$

The reduced frequency $\sigma = \omega c/U$ is not an independent parameter, it is determined by the three first nondimensional groups in this list. Θ is known as the feathering parameter [44], and is the ratio between the angle of the foil and the gliding angle.

This is a large parameter space, but we can make some headway into it by considering a stationary foil in a vortex street, in which case the input parameters reduce to the first 3 in (2.44). We will consider η_R as a function of p/c, q/c, and $\kappa/(Uc)$, see Figures 2-6 – 2-8. The leftmost end of each figure represents the minimum p/c that we can have for that particular $\kappa/(Uc)$, and still have a positive mean flow U_0.

These figures indicate that a moderate portion of the energy in the vortex street can be recovered by a stationary foil, particularly for narrow vortex streets (small q/c). This is not surprising, as a narrow vortex street has little energy and induces large upwash velocities leading to high thrust. Here we should keep the limitations of the theory in mind. Small values for q/p stretches the assumption used in the representation of the inflow.

Another limitation becomes evident when we compute the thrust coefficient, defined as $C_T =< T > /(cU^2)$ versus p/c and q/c. In Figure 2-9, $\log C_T$ is shown for $\kappa/(Uc) = 0.1$. We see that the thrust depends very strongly on the values of p and q, which are difficult to control during numerical simulations. Therefore, it is hard to get exact agreement in the average thrust between simulations and theory. Fortunately,

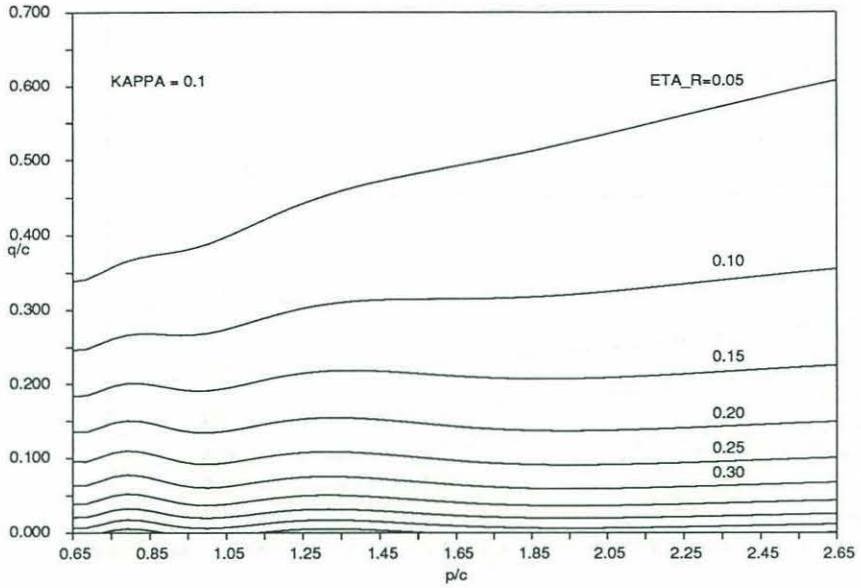

Figure 2-6: Energy recovery factor for stationary foil in vortex street. $\kappa/(Uc) = 0.1$.

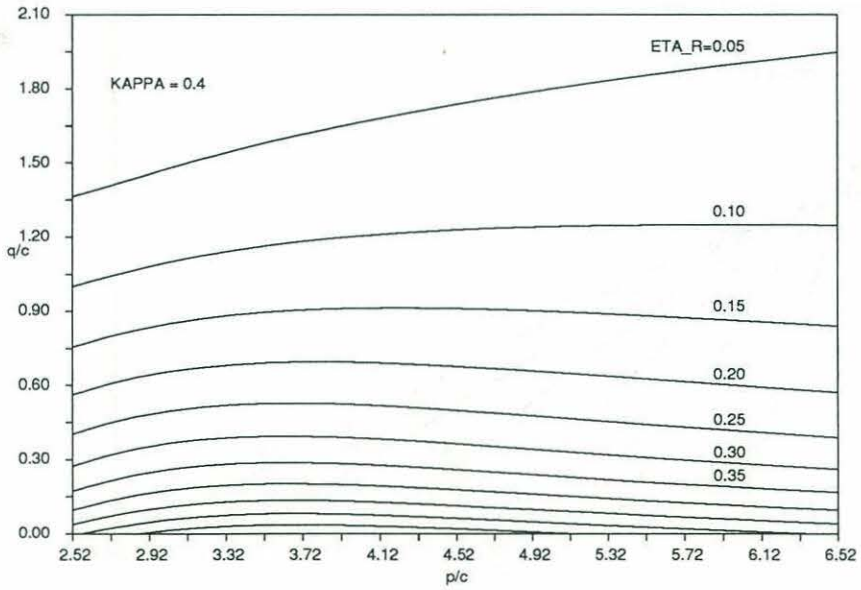

Figure 2-7: Energy recovery factor for stationary foil in vortex street. $\kappa/(Uc) = 0.4$.

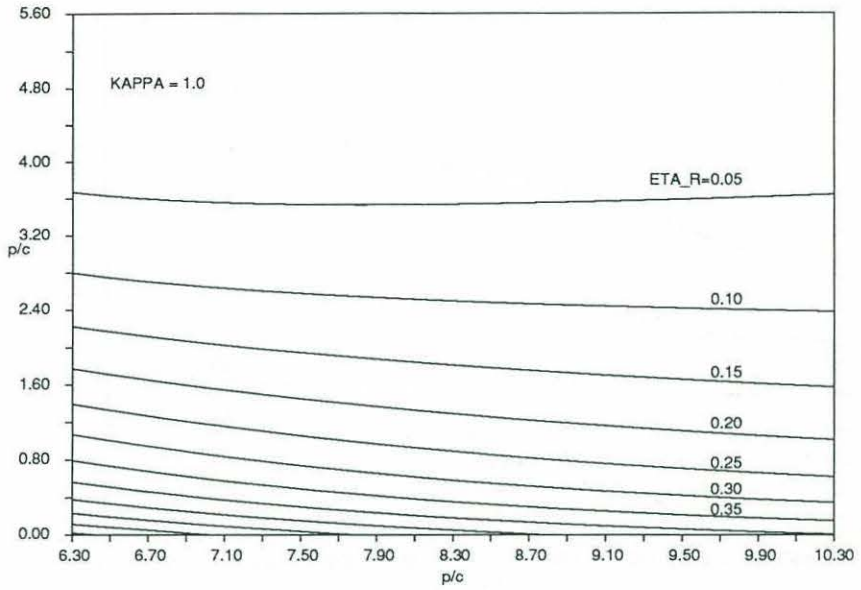

Figure 2-8: Energy recovery factor for stationary foil in vortex street. $\kappa/(Uc) = 1.0$.

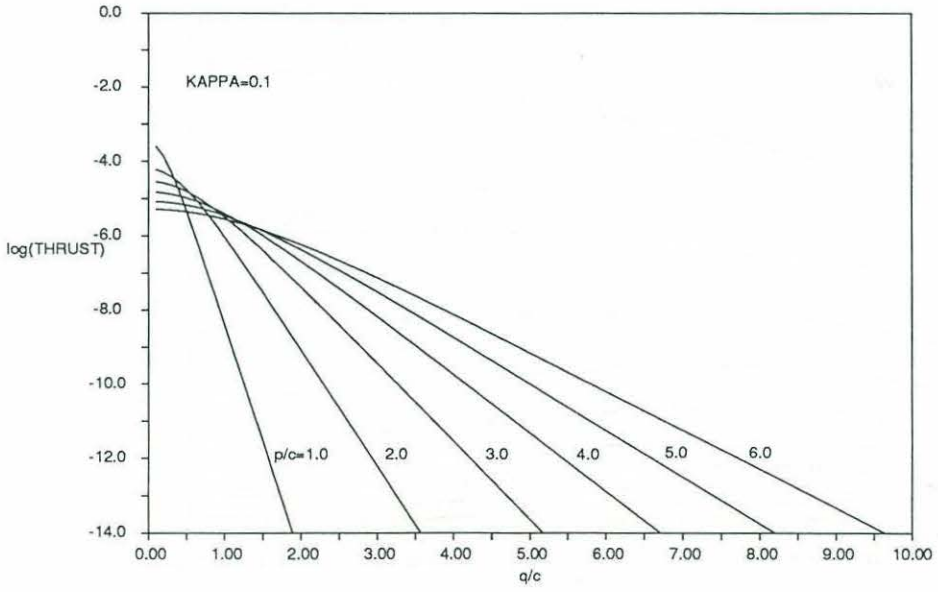

Figure 2-9: Thrust coefficient for a stationary foil in a vortex street with $\kappa/(Uc) = 0.1$

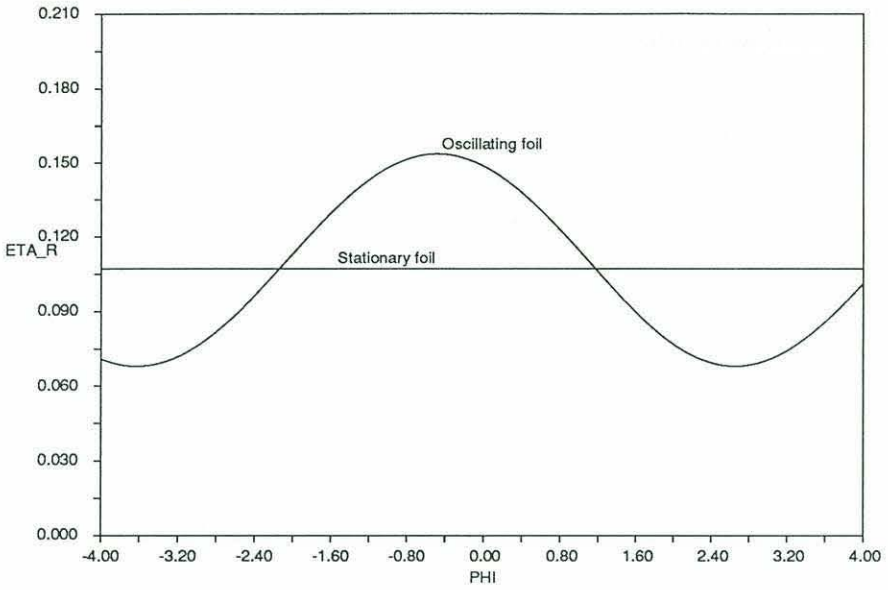

Figure 2-10: Energy recovery for oscillating foil for $\kappa/(Uc) = 0.4$, $p/c = 4$, $q/c = 1$.

this sensitivity goes away when the foil is heaving and pitching.

One interesting question to ask, is whether a foil that is allowed to heave and pitch can recover more of the vortex street energy than a stationary foil. If this is the case, it means that a bluff body can be optimally streamlined by using the foil in an active fashion, giving substance to the term "vortex control". If it is not the case, it means we are better off keeping the foil stationary if drag reduction is our main objective. In cases where the foil is intended as a propulsive device, this question becomes less important, as the foil must oscillate regardless of the value of η_R. Then we must ask which is better; placing the foil inside or outside the wake.

The theory does indicate that η_R can be increased by letting the foil oscillate, an example is shown in Figure 2-10. We see that a small heave and pitch motion ($h_0/c = 0.1$, $\alpha_0 = 0.05$, $b/c = 1.0$), can increase η_R over the value for a stationary foil, provided the phase ϕ is around 0.

In a paper that treats the problem of a foil oscillating in a fluid under the free surface, Grue & al. [32] found that up to 75% of the energy in incoming waves could be extracted by the foil. That is a different performance criterion, but it indicates that a higher energy recovery could be obtained in their problem.

We shall have more use for the theory in Chapter 4, where it provides verification of some of the simulation results.

Chapter 3

A numerical procedure for vortex flow over a Joukowski profile

3.1 Introduction

This chapter describes a method for simulating foil–vortex interaction, assuming that the flow is two–dimensional and inviscid. The assumption of two–dimensional flow limits the scope of the method to cases with high aspect ratio foils and incoming vortices of high correlation length, although we expect the qualitative results to be valid even when this assumption is relaxed. The inviscid flow assumption restricts the method to cases with high Reynolds number and absence of stall, or leading edge separation. Thus there is an implicit assumption of low local angles of attack in order to keep the flow attached to the foil, otherwise we should have to resort to computationally very intensive methods or experiments.

As a further simplification, the foil shape is taken to be a Joukowski profile, which is obtained through a simple transformation of a circular cylinder. This leads to a closed form description of the flow in the circle plane, where the vortex field is modeled with point vortices. Furthermore, the question of which face of the foil the wake is tangent to at the trailing edge [9] becomes a moot point, as the trailing edge of a Joukowski foil is cusped.

In order to evaluate the performance of the foil (mainly the efficiency), it is nec-

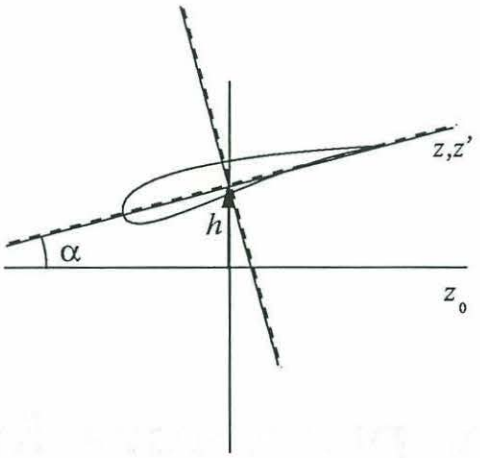

Figure 3-1: Definition of coordinate systems.

essary to calculate forces and moment experienced by the foil during the simulation. It is possible to numerically integrate the pressure on the foil at any time, but this is a slow process that requires many function calls involving all the vortices in the flow. Additional difficulties arise in cases where the foil has zero thickness and a sharp leading edge, which are important for verification. Therefore, a major part of the chapter is devoted to the derivation of closed form expressions for force and moment, using the fact that the foil shape is a Joukowski profile.

3.2 Coordinate systems

In the following we shall need 3 different plane coordinate systems to describe and solve for the flow over a wing profile in surge, heave and pitch. In complex notation, these are (1) $z_0 = x_0 + iy_0$, (2) $z = x + iy$ and (3) $z' = x' + iy'$. They are shown together in Figure 3-1.

(1) The z_0 plane is used to describe the mean flow and the motion of the foil. z_0 is fixed in the mean position of the foil, and an observer in this reference frame will see the foil oscillating in heave and pitch and a free stream U_0 flowing from left to

right. The motion of the foil has the following form:

$$\begin{aligned} h &= h_0 \cos(\omega t + \mu) - \alpha_0 b \sin(\omega t + \mu) \\ \alpha &= \alpha_0 \sin(\omega t + \mu) \end{aligned} \tag{3.1}$$

Here, h_0 and α_0 are heave and pitch amplitude respectively. The phasing between the two motions is determined by b. For motions of moderate pitch amplitude, b can also be thought of as the pitch point. ω, t and μ are frequency, time and phase, respectively. The freedom to choose the phase μ is convenient in certain cases. For example $\omega = 0$, $\mu = -\pi/2$ specify an impulsively started foil (the foil and fluid are assumed to be at rest at $t < 0$). It also allows arbitrary phase between the oncoming vortex street and the foil motion, just like $\phi = \omega t_0$ in the previous chapter. This may seem redundant, but since we cannot determine t_0 a priori in the simulations, it is more convenient to let μ vary and correct for t_0 afterwards. This will be dealt with in Chapter 4. The above definitions of the foil motion (with $\mu = 0$) coincide with Lighthill's [44] in the limit of small amplitudes. Other motions, such as a foil moving in circles without pitching [65], can be simulated with minor modifications.

(2) The z plane coincides with the foil at the instant under consideration, and is at rest in the fluid at infinity. An observer in this reference frame will see the foil moving in the x– and y–direction with velocities U and V respectively, sometimes denoted $W = U + iV$ for brevity. Furthermore, the foil is rotating counterclockwise about $z = 0$ with angular velocity Ω. This is the reference frame in which we solve the boundary value problem for the oscillating foil. The two coordinate systems are related by

$$z_0 = ih + ze^{i\alpha} \tag{3.2}$$

and the velocities are given by

$$\begin{aligned} W &= \left(-U_0 + i\dot{h}\right) e^{-i\alpha} \\ \Omega &= \dot{\alpha} \end{aligned} \tag{3.3}$$

(3) The z' plane is fixed in the foil at all times and coincides with z at any particular

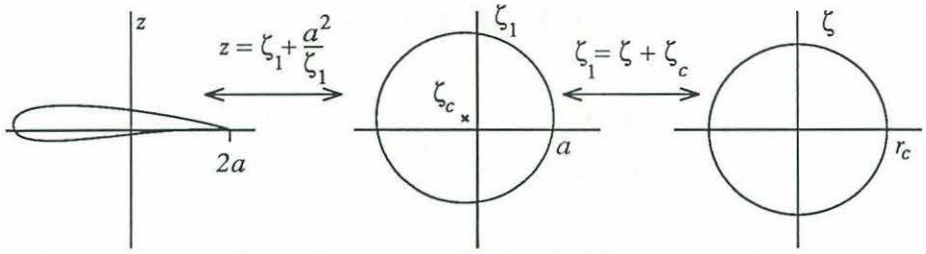

Figure 3-2: Mapping between Joukowski profile and circle.

instant. An observer in the z' system sees the fluid moving over a stationary foil, the fluid motion being everywhere rotational if $\Omega \neq 0$. The fact that the foil is fixed in this frame, makes it suitable for deriving force and moment expressions from pressure integration, The pressure expression must of course be corrected for non–inertial effects.

3.3 Conformal mapping

As Figure 3-2 shows, a Joukowski foil shape, S, can be obtained as a mapping of a circle, C, of radius r_c in the ζ plane:

$$z = F(\zeta) = \zeta + \zeta_c + \frac{a^2}{\zeta + \zeta_c} \tag{3.4}$$

This function is obtained in two steps. First, the foil is mapped to a circle in an intermediate plane, ζ_1, that has center at ζ_c and goes through the point a on the real axis. Thus, $r_c = |a - \zeta_c|$. This circle is mapped to the ζ plane by a simple translation. The parameters a and ζ_c determine the size, thickness and camber of the foil. The inverse of the mapping function is given by:[1]

$$\zeta = F^{-1}(z) = \frac{1}{2}\left[z + \sqrt{z^2 - 4a^2}\right] - \zeta_c \tag{3.5}$$

Three quantities of interest are the area, center of area and polar moment of area

[1] When implementing a multivalued expression like this one on a computer, it is important to choose the proper branch. FORTRAN returns square roots with nonnegative real part, and the correct inverse mapping results if we expand: $\zeta = \frac{1}{2}\left[z + \sqrt{z - 2a}\,\sqrt{z + 2a}\right] - \zeta_c$.

for the Joukowski foil. They can be found from either of the following expressions for an arbitrary function, f, of z and its complex conjugate, $\overline{z}$:

$$\int_{\partial R} f(z,\overline{z})d\overline{z} = -2i\int\int_R \frac{\partial f}{\partial z}dA \quad , \quad \int_{\partial R} f(z,\overline{z})dz = 2i\int\int_R \frac{\partial f}{\partial \overline{z}}dA \tag{3.6}$$

These expressions can be verified by virtue of Stokes theorem applied to the real and imaginary parts of f, on the two–dimensional region R which is bounded by ∂R [75]. Replacing ∂R by S, we can now write for the Joukowski foil area:

$$A = \int\int_R dA = \frac{1}{2i}\int_S \overline{z}dz$$

To evaluate the integral, we change the variable of integration to ζ and perform the integral on circle C:

$$A = \frac{1}{2i}\int_C \left(\overline{\zeta} + \overline{\zeta}_c + \frac{a^2}{\overline{\zeta} + \overline{\zeta}_c}\right) F'(\zeta)d\zeta$$

Here, the prime denotes derivative, and $F'(\zeta) = dF/d\zeta$ is not to be confused with the coordinate system fixed in the foil, z'. Using the fact that $\overline{\zeta} = r_c^2/\zeta$ on C, we obtain an integrand that is analytic except for discrete poles:

$$A = \frac{1}{2i}\int_C \left(\frac{r_c^2}{\zeta} + \overline{\zeta}_c + \frac{a^2}{r_c^2/\zeta + \overline{\zeta}_c}\right)\left(1 - \frac{a^2}{(\zeta + \zeta_c)^2}\right)d\zeta$$

The integrand is then expanded out to 6 terms that are evaluated by the residue theorem, and when they are added, we arrive at an expression for the area:

$$A = \pi r_c^2\left[1 - \frac{a^4}{(r_c^2 - \delta^2)^2}\right] \tag{3.7}$$

where $\delta^2 = \zeta_c\overline{\zeta}_c$.

Similarly, we have for the center of area, z_c, and radius of gyration, r_g:

$$z_c A = \int\int_R z dA = -\frac{1}{4i}\int_S z^2 d\overline{z} = \pi r_c^2\left[\zeta_c + \frac{a^6\overline{\zeta}_c}{(r_c^2 - \delta^2)^3}\right] \tag{3.8}$$

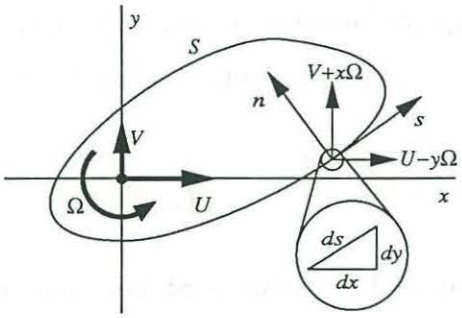

Figure 3-3: Definitions for boundary value problem.

$$r_g^2 A = \int\int_R z\bar{z}dA = -\frac{1}{4i}\int_S z^2\bar{z}d\bar{z} = \frac{\pi}{2}r_c^2\left[r_c^2 + 2\delta^2 - a^8\frac{r_c^2+2\delta^2}{(r_c^2-\delta^2)^4}\right] \tag{3.9}$$

The values for A and $z_c A$ were verified by the time–honored method of cutting the profile shape out of heavy cardboard, which could be weighted and balanced.

3.4 Boundary value problem for translating and rotating section

Consider an arbitrary profile S in the $z = x + iy$ plane, translating with velocity $W = U + iV$ and rotating with angular velocity Ω as shown in Figure 3-3. The velocity of a material particle at a point (x, y) on S, has a component v_n in the **n** direction. The boundary condition of no flow through S, can be written:

$$v_n = -\frac{\partial\psi}{\partial s} = -\frac{\partial\psi}{\partial x}\frac{dx}{ds} - \frac{\partial\psi}{\partial y}\frac{dy}{ds} \tag{3.10}$$

where ψ is the stream function of the flow. From the kinematics of the body it can be seen that:

$$v_n = (V + \Omega x)\frac{dy}{ds} - (U - \Omega y)\frac{dx}{ds}. \tag{3.11}$$

For these expressions to be consistent for arbitrary slopes dy/dx, the stream function must satisfy

$$\frac{\partial\psi}{\partial x} = -V - \Omega x \quad , \quad \frac{\partial\psi}{\partial y} = U - \Omega y \quad , \text{ on } S$$

i.e.

$$\psi = Uy - Vx - \frac{1}{2}\Omega(x^2 + y^2) \quad , \text{ on } S \tag{3.12}$$

We shall see later how vortices can be added to the flow without violating this condition.

Since the flow is assumed irrotational and incompressible, a complex potential can be formed from the velocity potential and the stream function in the usual manner:

$$w(z) = \phi(x, y) + i\psi(x, y)$$

In addition to (3.12), the conditions on w is that it must be analytic exterior to S (except at sharp corners) and have a vanishing derivative as $z \to \infty$. The form of the boundary condition (3.12) indicates that the solution is a linear superposition of three unit velocity potentials;

$$w = Uw_1 + Vw_2 + \Omega w_3$$

which must satisfy

$$\mathrm{Im}\{w_1\}_S = \mathrm{Im}\{z\}_S \, , \quad \mathrm{Im}\{w_2\}_S = \mathrm{Im}\{-iz\}_S \, , \quad \mathrm{Im}\{w_3\}_S = \mathrm{Im}\left\{-\frac{i}{2}z\overline{z}\right\}_S \tag{3.13}$$

The subscript on the curly brackets refers to the contour at which the relationships must hold, S from now on means the Joukowski profile.

Since the value of ψ must be the same at corresponding points in the physical and the mapped plane, the mapping (3.4) provides a way of solving these boundary value problems in the ζ plane. For example, the boundary condition for w_1 may be stated as;

$$\mathrm{Im}\{w_1\}_C = \mathrm{Im}\left\{\zeta + \zeta_c + \frac{a^2}{\zeta + \zeta_c}\right\}_C \tag{3.14}$$

We are looking for a solution that is analytic outside C. One might suggest that $\zeta + \zeta_c + a^2/(\zeta + \zeta_c)$ is in fact the solution for w_1. This would be acceptable, except for the first term, which violates the condition at infinity. However, we have the fact

that:

$$\mathrm{Im}\{\zeta\}_C = \mathrm{Im}\left\{-\frac{r_c^2}{\zeta}\right\}_C$$

Thus, by replacing the ζ term, the correct solution can be constructed:

$$w_1 = -\frac{r_c^2}{\zeta} + \zeta_c + \frac{a^2}{\zeta + \zeta_c} \tag{3.15}$$

The solution could be written explicitly in z through (3.5), but that would be an unnecessary complication, as there is no need to know $w(z)$ explicitly. For example, if we need the fluid velocity at a point z, we apply the chain rule:

$$u - iv = \frac{dw}{dz} = \frac{dw}{d\zeta}\frac{d\zeta}{dz} = \left[\frac{dw}{d\zeta}\frac{1}{F'(\zeta)}\right]_{\zeta=F^{-1}(z)}$$

The reason for keeping the constant ζ_c in w_1, is that the boundary condition (3.12) is assumed to hold without any additional constants in the calculation of the moment on the profile.

In the same way, w_2 is found to be:

$$w_2 = -i\frac{r_c^2}{\zeta} - i\zeta_c - i\frac{a^2}{\zeta + \zeta_c} \tag{3.16}$$

For w_3, which is somewhat more complicated, we use the intermediate variable ζ_1:

$$\begin{aligned}
\mathrm{Im}\{w_3\}_C &= \mathrm{Im}\left\{-\frac{i}{2}\left(\zeta_1 + \frac{a^2}{\zeta_1}\right)\left(\overline{\zeta}_1 + \frac{a^2}{\overline{\zeta}_1}\right)\right\}_C \\
&= \mathrm{Im}\left\{-\frac{i}{2}\left[\zeta_1\overline{\zeta}_1 + a^2\left(\frac{\overline{\zeta}_1}{\zeta_1} + \frac{\zeta_1}{\overline{\zeta}_1}\right) + \frac{a^4}{\zeta_1\overline{\zeta}_1}\right]\right\}_C \\
&= \mathrm{Im}\left\{-\frac{i}{2}\left[\zeta_1\overline{\zeta}_1 + 2a^2\frac{\overline{\zeta}_1}{\zeta_1} + \frac{a^4}{\zeta_1\overline{\zeta}_1}\right]\right\}_C \\
&= \mathrm{Im}\left\{-\frac{i}{2}\left[\zeta\overline{\zeta} + \overline{\zeta}_c\zeta + \zeta_c\overline{\zeta} + \delta^2 + 2a^2\frac{\overline{\zeta} + \overline{\zeta}_c}{\zeta + \zeta_c}\right.\right. \\
&\quad \left.\left. + \frac{a^4}{\zeta\overline{\zeta} + \overline{\zeta}_c\zeta + \zeta_c\overline{\zeta} + \delta^2}\right]\right\}_C
\end{aligned} \tag{3.17}$$

Now,

$$\zeta\overline{\zeta} = r_c^2 \quad \text{on } C \quad \text{and} \quad \text{Im}\{i\overline{\zeta}_c\zeta\} = \text{Im}\{i\zeta_c\overline{\zeta}\},$$

so that

$$\begin{aligned}
\text{Im}\{w_3\}_C &= \text{Im}\left\{-\frac{i}{2}\left[r_c^2 + 2\zeta_c\overline{\zeta} + \delta^2 + 2a^2\frac{\overline{\zeta}+\overline{\zeta}_c}{\zeta+\zeta_c} + \frac{a^4}{r_c^2 + \overline{\zeta}_c\zeta + \zeta_c\overline{\zeta} + \delta^2}\right]\right\}_C \\
&= \text{Im}\left\{-\frac{i}{2}\left[r_c^2 + 2\zeta_c\frac{r_c^2}{\zeta} + \delta^2 + 2a^2\frac{r_c^2/\zeta + \overline{\zeta}_c}{\zeta+\zeta_c}\right.\right. \\
&\quad \left.\left. + \frac{a^4}{r_c^2 + \overline{\zeta}_c\zeta + \zeta_c r_c^2/\zeta + \delta^2}\right]\right\}_C \qquad (3.18)
\end{aligned}$$

The only thing preventing the use of the expression inside the curly brackets as a solution for w_3 is the last term, which contains a dipole singularity at $\zeta = -r_c^2/\overline{\zeta}_c$. This singularity must be neutralized by adding another dipole of opposite strength, according to the circle theorem of two–dimensional potential flow [10, 75]. This theorem will be of great use in the next section, and it goes as follows:

Consider a flow with complex potential $f(z)$, whose singularities are all at a distance greater than r_c away from the origin. A flow with the same singularities and far field behavior, but internally bounded by a circle of radius r_c centered at the origin, has the potential:

$$w(z) = f(z) + \overline{f}\left(\frac{r_c^2}{z}\right)$$

It is straightforward to verify that this potential is purely real on the circle, $|z| = r_c$, making the circle a streamline.

Now, we can put a dipole of moment q, say, at $\zeta = -r_c^2/\overline{\zeta}_c$ without affecting the boundary condition (3.12) by adding:

$$\frac{q}{\zeta + r_c^2/\overline{\zeta}_c} - \frac{\overline{q}}{r_c^2/\zeta + r_c^2/\overline{\zeta}_c}$$

to the flow. To cancel the singularity external to C in (3.18), the dipole strength q must be chosen:

$$q = -\frac{ia^4 r_c^2}{(r_c^2 - \delta^2)\overline{\zeta}_c}$$

We add these terms inside the curly brackets of (3.18), and when the terms are combined, the correct solution for w_3 is obtained:

$$w_3 = -i\left[\frac{\zeta_c r_c^2}{\zeta} + a^2\frac{r_c^2/\zeta + \overline{\zeta}_c}{\zeta + \zeta_c} + \frac{a^4\zeta_c}{(\zeta+\zeta_c)(r_c^2+\delta^2)} + \frac{a^4 + r_c^4 - \delta^4}{2(r_c^2-\delta^2)}\right] \tag{3.19}$$

Figure 3-4 shows the streamlines associated with the three unit potentials in the case of a profile with $a = 0.5$, $\zeta_c = -0.05 + i0.1$.

3.5 Vortex potentials

In addition to the potentials due to foil motion, we must determine the influence of point vortices in the flow. First we note that an arbitrary amount of circulation around the foil is provided by a central vortex in the ζ plane:

$$\gamma_c w_4 = \gamma_c i \log\frac{\zeta}{r_c} \tag{3.20}$$

w_4 is purely real on C and S, so this term can be added without affecting the boundary condition (3.12).

Finally, a free vortex at some point z_k, is introduced by adding a vortex at the corresponding point in the ζ plane, $\zeta_k = F^{-1}(z_k)$. According to the circle theorem, this vortex must have an oppositely signed image at the *inverse point*, $r_c^2/\overline{\zeta}_k$ and a same sign image at $\zeta = 0$. The latter can be absorbed in $\gamma_c w_4$ however, and is not considered a part of the free vortex potential. Instead, the value of γ_c is determined on physical grounds when a new vortex is introduced in the flow. Any number of vortices of different strengths can be incorporated by linear superposition:

$$\sum_k \gamma_k w_5(\zeta;\zeta_k)$$

where

$$w_5 = i\log\left(-\frac{r_c}{\zeta_k}\frac{\zeta-\zeta_k}{\zeta - r_c^2/\overline{\zeta}_k}\right) \tag{3.21}$$

As with the central vortex potential, w_5 is written such that it is purely real on S,

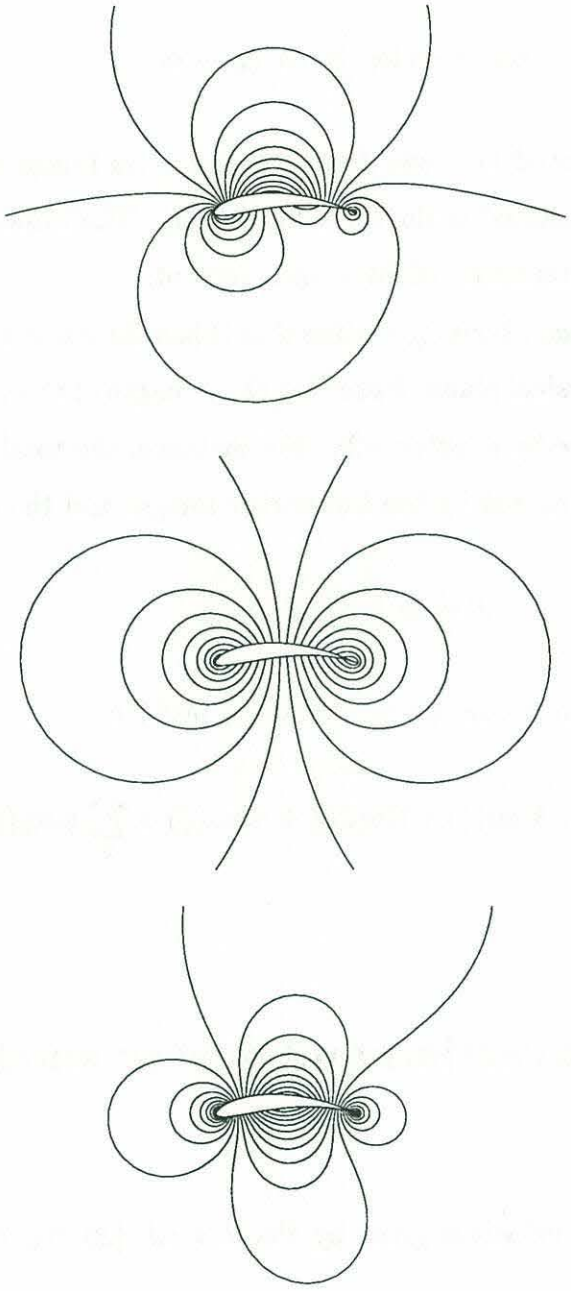

Figure 3-4: Streamlines of the unit velocity potentials. From top to bottom: w_1, w_2 and w_3.

and (3.12) holds without any additional constant. In addition, care has been taken to ensure that for $|\zeta| = O(r_c)$:

$$w_5 \to -i \log \frac{\zeta}{r_c} \text{ as } \zeta_k \to \infty$$

Thus, as a vortex is removed far away from the circle, its image moves toward the center, giving rise to a potential af the same form as w_4. The importance of this will become evident in the formulation of force and moment.

A Taylor expansion of w_5 about ζ_k, verifies that it has the correct singular behavior of a vortex at z_k in the physical plane. Note that the strength of the vortices differ from what many researchers use by a factor -2π. For instance, the total counterclockwise circulation about the foil caused by the free vortex images and the central vortex, is:

$$\Gamma = 2\pi \left(\sum_k \gamma_k - \gamma_c \right) \tag{3.22}$$

The flow in the z plane is now completely described by:

$$w = U w_1(\zeta) + V w_2(\zeta) + \Omega w_3(\zeta) + \gamma_c w_4(\zeta) + \sum_k \gamma_k w_5(\zeta; \zeta_k)$$

and the mapping (3.4).

3.6 Vortex convection and vortex shedding algorithm

The vortices convect with velocities given by *Routh's rule* [20, 63, 70];

$$\begin{aligned} \frac{d\overline{z}_k}{dt} &= \frac{d}{dz} \left[w(z) - i\gamma_k \log(z - z_k) \right]_{z=z_k} \\ &= \frac{1}{F'(\zeta_k)} \frac{d}{d\zeta} \left[w(\zeta) - i\gamma_k \log(\zeta - \zeta_k) \right]_{\zeta=\zeta_k} - \frac{i\gamma_k}{2} \frac{F''(\zeta_k)}{[F'(\zeta_k)]^2} \end{aligned} \tag{3.23}$$

In the second step the chain rule has been applied, and the last term is a correction due to the difference between $\log(z - z_k)$ and $\log(\zeta - \zeta_k)$. This expression is used to

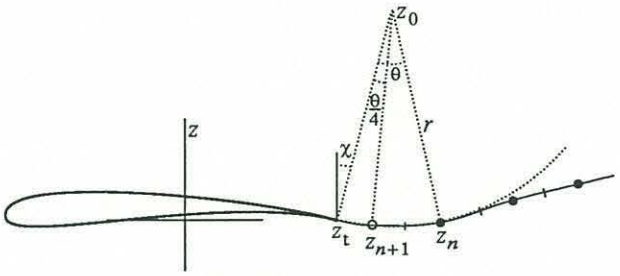

Figure 3-5: Vortex shedding algorithm.

step forward the simulation in a second order Runge-Kutta scheme. The derivative of the terms in the square bracket can be expressed in closed form. It will consist of contributions from the three unit potentials and all the vortex potentials except for the one due to vortex k itself. Thus, as the number of vortices N grows, this $O(N^2)$ effort quickly becomes prohibitively slow. A method based on multipole expansions [31, 15, 39] that reduces this effort to $O(N)$ has been implemented, greatly reducing the computational effort when the number of vortices becomes large. See Appendix A for a description.

An algorithm that releases vortices into the flow to satisfy the Kutta condition of smooth flow at the trailing edge, will complete the simulation. A certain controversy exists regarding the validity range of the Kutta condition [47], but this question will not be addressed here. We assume that the parameters of foil motion and inflow conditions are such that smooth flow over the trailing edge is a good model.

In general, there is no obvious way to introduce vortices near the trailing edge in order to satisfy the Kutta condition. Matters are simplified, however, by the fact that the trailing edge of the Joukowski foil is cusped, and that the wake must leave the trailing edge parallel to it. A vortex shedding algorithm based on an idea due to Sarpkaya [62] is illustrated in Figure 3-5. The idea is that the location of a new vortex can be determined from an interpolation between the trailing edge and one or more previously shed vortices. Each vortex in the wake (solid dots) represents a segment (between tic marks) of a continuous vortex sheet. When it is time to shed a new vortex, a circular arc tangent to the cusped trailing edge z_t, is fitted through the location of the previously shed vortex, z_n (the trailing edge angle χ is given by

the conformal mapping). The center of the arc is denoted z_0 and the angle $z_t z_0 z_n$ is θ. The new vortex is put at z_{n+1} such that the angle $z_t z_0 z_{n+1}$ is $\theta/4$. Consequently, the new vortex will sit approximately in the middle of the segment it is supposed to represent. The following relations hold:

$$\begin{aligned} z_0 - z_n &= re^{i(\frac{\pi}{2}-\chi+\theta)} \\ z_0 - z_t &= re^{i(\frac{\pi}{2}-\chi)} \\ z_0 - z_{n+1} &= re^{i(\frac{\pi}{2}-\chi+\theta/4)} \end{aligned}$$

We can write:

$$\frac{(z_n - z_t)^2}{|z_n - z_t|^2} = -e^{-i2\chi}\frac{1-e^{i\theta}}{1-e^{-i\theta}} = e^{-i2\chi}e^{i\theta} \tag{3.24}$$

$$\frac{z_{n+1} - z_t}{z_n - z_t} = \frac{1-e^{i\theta/4}}{1-e^{i\theta}}$$

The latter expression is ill posed at $\theta = 0$, but fortunately, the denominator can be factored[2]:

$$\begin{aligned} \frac{z_{n+1} - z_t}{z_n - z_t} &= \frac{1-e^{i\theta/4}}{(1-e^{i\theta/4})(1+e^{i\theta/4})(1+e^{i\theta/2})} \\ &= \frac{1}{1+e^{i\theta/4}+e^{i\theta/2}+e^{i3\theta/4}} \end{aligned} \tag{3.25}$$

Combining (3.24) and (3.25) will then give us z_{n+1} from known quantities. The strength of the new vortex is given by the requirement that $dw/d\zeta = 0$ at the point which maps onto the trailing edge, $\zeta = a - \zeta_c$. This is necessary for the flow to be smooth at the trailing edge in the physical plane and constitutes the Kutta condition in the simulation:

$$\begin{aligned} \frac{dw}{d\zeta} &= U\left[\frac{r_c^2}{\zeta^2} - \frac{a^2}{(\zeta+\zeta_c)^2}\right] + iV\left[\frac{r_c^2}{\zeta^2} + \frac{a^2}{(\zeta+\zeta_c)^2}\right] \\ &\quad + i\Omega\left[\frac{\zeta_c r_c^2}{\zeta^2} + a^2 r_c^2 \frac{2\zeta+\zeta_c}{\zeta^2(\zeta+\zeta_c)^2} + a^2\frac{\overline{\zeta}_c}{(\zeta+\zeta_c)^2} - \frac{a^4\zeta_c}{(\zeta+\zeta_c)^2(r_c^2-\delta^2)}\right] \end{aligned}$$

[2]Thanks to Dr. Séamus Tuohy for pointing this out.

$$+i\frac{\gamma_c}{\zeta}+\sum_{k=1}^{n+1} i\gamma_k\left[\frac{1}{\zeta-\zeta_k}-\frac{1}{\zeta-r_c^2/\bar{\zeta}_k}\right]$$
$$= \quad 0\,,\text{at}\;\;\zeta=a-\zeta_c \tag{3.26}$$

Denoting $a-\zeta_c = r_c e^{i\theta_c}$, $\zeta_k = r_k e^{i\theta_k}$ and $\zeta_c = \delta_R + i\delta_I$, we can solve for γ_{n+1}, and write the answer in terms of real quantities only:

$$\begin{aligned}\gamma_{n+1} \;=\; & -\frac{r_c^2-2r_c r_{n+1}\cos(\theta_c+\theta_{n+1})+r_{n+1}^2}{r_c^2-r_{n+1}^2} \\ & \left[2r_c(U\sin\theta_c+V\cos\theta_c)+2\Omega\left(a^2-a\delta_R-\delta^2\frac{a-\delta_R}{a-2\delta_R}\right)\right. \\ & \left.+\gamma_c+\sum_{k=1}^{n}\frac{\gamma_k(r_c^2-r_k^2)}{r_c^2-2r_c r_k\cos(\theta_c+\theta_k)+r_k^2}\right]\end{aligned} \tag{3.27}$$

With the strength of the free vortices determined, we must now consider the value of γ_c. In cases where the foil starts to move from an initial state of rest and the fluid is otherwise undisturbed, the total circulation around the foil and its wake must remain zero by virtue of Kelvin's circulation theorem. This implies that $\gamma_c = 0$ at all times. In the general case, vortices other than those shed at the trailing edge may be introduced in the flow at any time. Then, γ_c must change so as to preserve the circulation around the foil alone. In fact, due to the way the vortex potentials are defined, the total effect on w of such a vortex vanishes, as the point where it is introduced moves to infinity.

We can test this algorithm by comparing the foil circulaton, Γ, with linear theory for a flat plate impulsively pitched to $\alpha_0 = 0.01$. This is a good test, because the step function response obtained will contain the frequency response for all frequencies. The effect of the finite angle of attack is vanishing for the steady case, so we assume that this is true also here. Figure 3-6 shows that the vortex shedding algorithm described above yields a foil circulation in close agreement with linear theory, even for fairly large time steps. Time has been nondimensionalized by c/U_0, where c is the half chord length.

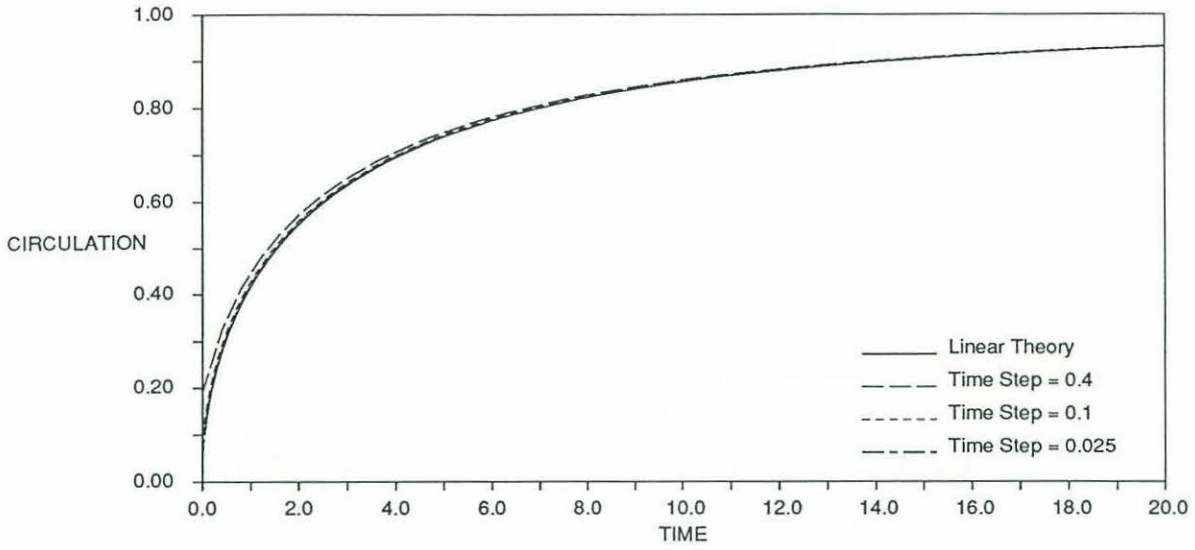

Figure 3-6: Circulation around an impulsively started flat plate normalized by its steady state value.

3.7 Pressure in a rotating and translating coordinate frame

In order to develop expressions for force and moment, it is useful to express the pressure in terms of coordinates that are fixed in the foil, z' in Figure 3-1. In the z coordinate system, which is an inertia frame, the pressure is given by

$$p = -\frac{\partial \phi}{\partial t} - \frac{1}{2}(u^2 + v^2)$$

where u and v are flow velocity components[3]. The z' frame moves with velocities $W = U + iV$ and Ω, as given by (3.3), and the flow velocities seen by an observer in this reference frame are:

$$u' = u - U + \Omega y \ , \ \ v' = v - V - \Omega x$$

[3]Fluid density is assumed to be unity, unless otherwise noted.

For later reference we note that

$$u' + iv' = \overline{\left(\frac{dw}{dz}\right)} - W - i\Omega z \tag{3.28}$$

Furthermore, the time derivative must be adjusted for spatial variation when the moving coordinate system is used:

$$\frac{\partial}{\partial t} \leftarrow \frac{\partial}{\partial t} - (U - \Omega y)\frac{\partial}{\partial x} - (V + \Omega x)\frac{\partial}{\partial y}$$

Thus, in the foil fixed coordinate system the pressure is given by:

$$p = -\frac{\partial \phi}{\partial t} - \frac{1}{2}(u'^2 + v'^2) + \frac{1}{2}(W + i\Omega z)(\overline{W} - i\Omega \overline{z}) \tag{3.29}$$

The first term should be thought of as the rate of change, as seen by an observer in the z' frame, of the potential that describes the flow in the z frame.

The utility of expressing pressure this way is that the profile S, over which the pressure must be integrated, is independent of time. Thus, the time derivative in the first term may be taken outside the integral sign.

Figure 3-7 shows the difference in pressure, calculated by the above expression, between the lower and upper face of a flat plate at a small angle of attack, in impulsively started motion. We note that the simulation results agree well with linear theory, except at the trailing edge where our method fails to predict zero pressure loading. This is a result of discretizing the wake into point vortices, because they cannot represent a flow that is discontinuous across the trailing edge. If the velocity on the upper and lower side of the trailing edge is denoted u_+ and u_- respectively, it is easy to show that

$$\frac{d\Gamma}{dt} = \frac{1}{2}(u_-^2 - u_+^2)$$

is necessary for zero pressure loading [9]. From linear theory we know that $d\Gamma/dt \sim t^{-1/2}$ as $t \rightarrow 0$, i.e. the velocity discontinuity is arbitrarily large at $t = 0$. Therefore, it is not surprising that the error in the simulation is largest initially. Furthermore we note that the discrepancy is confined to a smaller region when the time step is

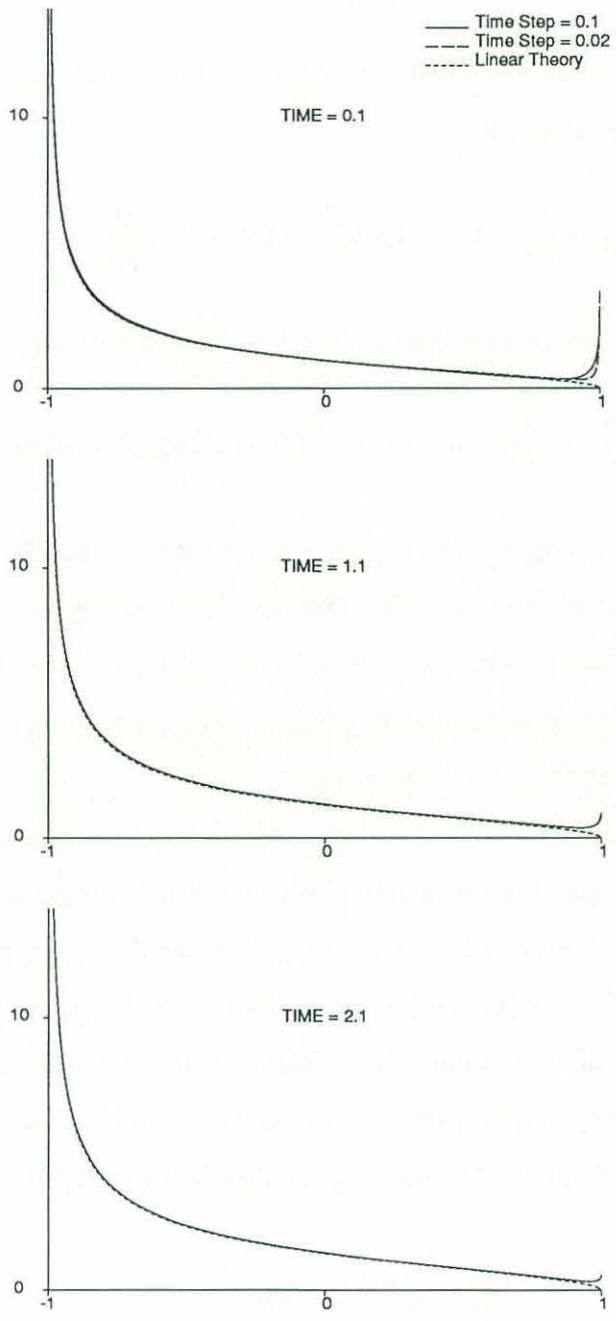

Figure 3-7: Pressure distribution at three different times for an impulsively started foil.

reduced and the trailing edge vortices are more packed together.

3.8 Force

Representing the forces per unit span X and Y along the x and y axes as one complex number, we find:

$$X + iY = i \int_S p dz \tag{3.30}$$

Using (3.29), Milne Thomson [75] develops the following force expression[4]:

$$\begin{aligned}
X + iY &= -i\frac{d}{dt}\int_S \phi dz - \frac{i}{2}\int_S (u'^2 + v'^2)dz + \frac{i}{2}\int_S (W + i\Omega z)(\overline{W} - i\Omega\overline{z})dz \\
&= -i\frac{d}{dt}\left[\int_S w dz + iWA - \Omega A z_c\right] - \overline{\frac{i}{2}\int_S \left[\frac{dw}{dz} - \overline{W} + i\Omega\overline{z}\right]^2 dz} + i\Omega A(W + i\Omega z_c) \\
&= -i\frac{d}{dt}\int_S w dz + \dot{W}A + i\dot{\Omega}Az_c - \overline{\frac{i}{2}\int_S \left[\left(\frac{dw}{dz}\right)^2 + 2\frac{dw}{dz}(-\overline{W} + i\Omega\overline{z})\right] dz} \\
&\quad -i\Omega A(W + i\Omega z_c) \\
X + iY &= -i\frac{d}{dt}\int_S w dz + \dot{W}A + i\dot{\Omega}Az_c - \overline{\frac{i}{2}\int_S \left(\frac{dw}{dz}\right)^2 dz} - \Omega\int_S z dw + iW\Gamma \\
&\quad +i\Omega A(W + i\Omega z_c)
\end{aligned} \tag{3.31}$$

where A, z_c and Γ are given by (3.7), (3.8) and (3.22), respectively. To obtain these expressions, we have made use of (3.6), (3.28), and the fact that the flow is parallel to S:

$$(u'^2 + v'^2)dz = (u' + iv')(u' - iv')dz = (u' + iv')^2 d\overline{z}$$

and the boundary condition (3.12):

$$\phi = w - i\psi = w - \frac{1}{2}(\overline{W}z - W\overline{z} - i\Omega z\overline{z}) \ , \ \text{on} \ S$$

The three integrals in (3.31) will be referred to as (I), (II) and (III) respectively. They can be evaluated by replacing the contour of integration by one that encloses

[4]Note that Milne Thomson uses a different sign convention for the complex potential.

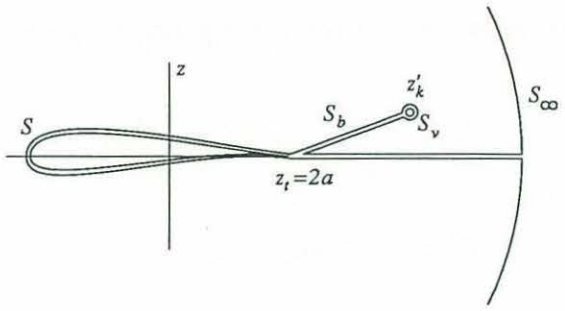

Figure 3-8: Integration contour for force.

all singularities and branch cuts, as well as S, and is closed at a large distance from the foil. This method has been used by Graham [30] and Sarpkaya [62] for flow over stationary objects. It is an extension of Lagally's theorem, which is valid for vortices that are being held fixed in a steady flow. The contour of integration is shown in Figure 3-8 for the case of a single free vortex. We have denoted the vortex position z'_k as a reminder that its time derivative must be taken as seen by an observer moving with the foil,

$$z'_k = z_k = F(\zeta_k)\ , \text{but}\ \frac{dz'_k}{dt} = \frac{dz_k}{dt} - W - i\Omega z_k = \frac{d}{dt}F(\zeta_k)$$

In the region within the entire contour, all the integrands are analytic, so the sum of the integrals evaluated over the different parts of the contour must be zero. This yields expressions for the integrals over S in terms of the other contributions, which are easier to evaluate:

$$\int_S = \int_{S_\infty} - \int_{S_v} - \int_{S_b}$$

– the direction of integration being counterclockwise. S_b encloses the branch cut between the vortex and its image, passing through the trailing edge. The integrals in (3.31) can be evaluated as follows:

(I) In the first integral, w_4 is not suited to integration on the contour in Figure 3-8, and will be evaluated later directly on S. Omitting w_4, the first integral gets a contribution from the cut S_b, where w makes a jump $2\pi\gamma_k$ from the upper to the

lower bank, and from S_∞. The following expression is then true for arbitrary profiles:

$$\int_S w dz = \int_{S_\infty} w dz - 2\pi\gamma_k(z'_k - z_t)$$

where z_t is the location of the trailing edge. Limiting ourselves to the previously defined Joukowski profile, we can readily find the far field behavior of w and identify the terms that go like $1/z$. By the residue theorem we then find the contribution from S_∞:

$$\begin{aligned}\int_{S_\infty} w dz &= 2\pi\left[iU\left(a^2 - r_c^2\right) + V\left(a^2 + r_c^2\right) + \right. \\ &\left. \Omega\left(r_c^2\zeta_c + a^2\overline{\zeta}_c - \frac{a^4\zeta_c}{r_c^2 - \delta^2}\right) + \gamma_k\left(\zeta_k - \frac{r_c^2}{\overline{\zeta}_k}\right)\right]\end{aligned}$$

Then we must add the contribution from $\gamma_c w_4$ by integrating by parts on S:

$$\int_S w_4 dz = [w_4 z]_-^+ - \int_S \frac{dw_4}{dz} z dz = -2\pi z_{cut} - \int_C F(\zeta) dw_4 = -2\pi(z_{cut} - \zeta_c)$$

The square bracket with limits means that the difference should be taken at opposite sides of the branch cut associated with the logarithmic potential, with the upper and lower limits corresponding to a counterclockwise direction of integration. The value of the integral depends on where this branch cut is chosen to be. The choice is made based on the notion that when an external vortex is introduced, the effect on the total potential integrated around the foil must vanish as the vortex is introduced further away. This requires that the $z_{cut} = 2a$, i.e. the branch cut for w_4 must pass through the trailing edge just like for the free vortices. Now,

$$\begin{aligned}\int_S w dz &= 2\pi\left[iU\left(a^2 - r_c^2\right) + V\left(a^2 + r_c^2\right) + \Omega\left(r_c^2\zeta_c + a^2\overline{\zeta}_c - \frac{a^4\zeta_c}{r_c^2 - \delta^2}\right)\right. \\ &\left. -\gamma_c(2a - \zeta_c) + \gamma_k\left(\zeta_k - \frac{r_c^2}{\overline{\zeta}_k} - z'_k + 2a\right)\right] \qquad (3.32)\end{aligned}$$

(II) The second integral gets no contributions from the cut S_b where the integrand is continuous. Neither is there a contribution from S_∞, as $w = \mathcal{O}(\log z)$ in the far

field (this is in contrast to steady flow past a stationary wing which gets $U\Gamma$ from this term). The only contribution is from S_v, this term is found by writing the potential with the singularity at z_k separated out:

$$w(z) = f_k(z) + i\gamma_k \log(z - z_k)$$

where $f_k(z)$ is analytic in the neighborhood of z_k. Then

$$\int_S \left(\frac{dw}{dz}\right)^2 dz = -\int_{S_v} \left(f_k'(z) + \frac{i\gamma_k}{z - z_k}\right)^2 dz = 4\pi\gamma_k f_k'(z_k)$$

where again, the prime denotes z derivative. From (3.23) it is seen that $\overline{f_k'(z_k)}$ is the convection velocity of the vortex, as seen in the z reference frame, i.e.

$$\overline{\int_S \left(\frac{dw}{dz}\right)^2 dz} = 4\pi\gamma_k \frac{dz_k}{dt} = 4\pi\gamma_k \left(\frac{dz_k'}{dt} + W + i\Omega z_k'\right) \tag{3.33}$$

This expression is valid for an arbitrary profile.

(III) In the last integral, $\gamma_c w_4$ also requires special attention. Apart from this term, we have

$$\int_S z dw = \int_S \frac{dw}{dz} z dz$$

which gets contributions from S_∞ and S_v. The latter is easily found, and we have the general expression:

$$\int_S z dw = \int_{S_\infty} \frac{dw}{dz} z dz + 2\pi\gamma_k z_k'$$

For the Joukowski profile,

$$\int_{S_\infty} z dw = 2\pi \left[iU\left(r_c^2 - a^2\right) - V\left(r_c^2 + a^2\right) - \Omega\left(r_c^2\zeta_c + a^2\overline{\zeta}_c - \frac{a^4\zeta_c}{r_c^2 - \delta^2}\right) + \gamma_k\left(\frac{r_c^2}{\overline{\zeta}_k} - \zeta_k\right)\right]$$

We saw above that

$$\int_S z dw_4 = -2\pi\zeta_c$$

Thus,

$$\begin{aligned}\int_S z dw &= 2\pi\left[iU\left(r_c^2-a^2\right)-V\left(r_c^2+a^2\right)-\Omega\left(r_c^2\zeta_c+a^2\overline{\zeta}_c-\frac{a^4\zeta_c}{r_c^2-\delta^2}\right)\right.\\ &\left.-\gamma_c\zeta_c+\gamma_k\left(\frac{r_c^2}{\overline{\zeta}_k}-\zeta_k+z_k'\right)\right]\end{aligned}$$

We have now calculated all the necessary integrals for a closed form force expression. In cases with $\gamma_c = 0$, the following expression may be used to evaluate the force on an arbitrary profile in the presence of point vortices, requiring only the far field behavior of the velocity potential:

$$\begin{aligned}X+iY &= -i\frac{d}{dt}\left[\int_{S_\infty} w dz - 2\pi\sum_k \gamma_k(z_k'-z_t)\right]+\dot{W}A+i\dot{\Omega}Az_c-2\pi i\sum_k\gamma_k\frac{dz_k'}{dt}\\ &-\int_{S_\infty}\frac{dw}{dz}z dz+i\Omega A(W+i\Omega z_c) \qquad (3.34)\end{aligned}$$

We have extended the result to an arbitrary number of vortices simply by summing over k. Two terms cancelled due to (3.22). In cases where the number of vortices around the profile remain constant, the time derivative may be taken inside the first summation and cancellation with the second sum is obtained. Here we want to use the above expression when vortices are released every time step into the flow, and we leave the time derivative outside the sum to take into account the changing number of vortices.

For the Joukowski foil, we use the results (I) – (III), and collect terms to obtain:

$$\begin{aligned}X+iY &= -\dot{U}[2\pi(r_c^2-a^2)-A]\\ &-i\dot{V}[2\pi(r_c^2+a^2)-A]\\ &-i\dot{\Omega}\left[2\pi\left(r_c^2\zeta_c+a^2\overline{\zeta}_c-\frac{a^4\zeta_c}{r_c^2-\delta^2}\right)-Az_c\right]\\ &-iU\Omega\left[2\pi(r_c^2-a^2)-A\right]\\ &+V\Omega\left[2\pi(r_c^2+a^2)-A\right]\\ &+\Omega^2\left[2\pi\left(r_c^2\zeta_c+a^2\overline{\zeta}_c-\frac{a^4\zeta_c}{r_c^2-\delta^2}\right)-z_cA\right]\\ &+iW\Gamma\end{aligned}$$

$$
\begin{aligned}
&-i\frac{d}{dt}\left[-2\pi\gamma_c(2a-\zeta_c)+2\pi\sum_k\gamma_k\left(2a-\zeta_c-\frac{r_c^2}{\overline{\zeta}_k}-\frac{a^2}{\zeta_k+\zeta_c}\right)\right]\\
&-2\pi i\sum_k\gamma_k\frac{dz_k}{dt}\\
&-\Omega\left[-2\pi\gamma_c\zeta_c+2\pi\sum_k\gamma_k\left(\frac{r_c^2}{\overline{\zeta}_k}+\zeta_c+\frac{a^2}{\zeta_k+\zeta_c}\right)\right] \qquad (3.35)
\end{aligned}
$$

The conventional added mass notation, m_{ij} [51], and the relation (3.22) provides a compact expression for the forces:

$$
\begin{aligned}
X+iY &= -\dot{U}(m_{11}+im_{21})-\dot{V}(m_{12}+im_{22})-\dot{\Omega}(m_{16}+im_{26})\\
&\quad +\Omega U(m_{21}-im_{11})+\Omega V(m_{22}-im_{12})+\Omega^2(m_{26}-im_{16})\\
&\quad +i(W+i\Omega\zeta_c)\Gamma+i\frac{d}{dt}[2\pi\mathcal{Z}_1-\Gamma(2a-\zeta_c)]-2\pi i\mathcal{Z}_2-2\pi\Omega\mathcal{Z}_1 \qquad (3.36)
\end{aligned}
$$

where the added mass coefficients have been identified as:

$$
\begin{aligned}
m_{11} &= \pi r_c^2-2\pi a^2+\pi r_c^2\frac{a^4}{(r_c^2-\delta^2)^2} && (3.37)\\
m_{12} &= 0 && (3.38)\\
m_{21} &= 0 && (3.39)\\
m_{22} &= \pi r_c^2+2\pi a^2+\pi r_c^2\frac{a^4}{(r_c^2-\delta^2)^2} && (3.40)\\
m_{16} &= Im\left\{-\pi r_c^2\zeta_c-2\pi a^2\overline{\zeta}_c+2\pi\frac{a^4\zeta_c}{r_c^2-\delta^2}+\pi r_c^2\frac{a^6\overline{\zeta}_c}{(r_c^2-\delta^2)^3}\right\} && (3.41)\\
m_{26} &= Re\left\{\pi r_c^2\zeta_c+2\pi a^2\overline{\zeta}_c-2\pi\frac{a^4\zeta_c}{r_c^2-\delta^2}-\pi r_c^2\frac{a^6\overline{\zeta}_c}{(r_c^2-\delta^2)^3}\right\} && (3.42)
\end{aligned}
$$

and

$$
\begin{aligned}
\mathcal{Z}_1 &= \sum_k\gamma_k\left(\frac{r_c^2}{\overline{\zeta}_k}+\frac{a^2}{\zeta_k+\zeta_c}\right) && (3.43)\\
\mathcal{Z}_2 &= \sum_k\gamma_k\frac{dz_k}{dt} && (3.44)
\end{aligned}
$$

The added mass coefficients have been verified versus Sedov's [68] expressions, in the special case of a symmetric profile. Note that there is no added mass coupling

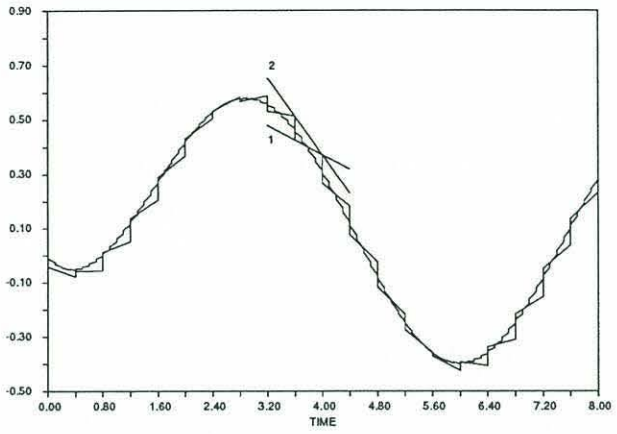

Figure 3-9: Typical time history of sum in brackets in equation (3.36) for two different time steps, $\Delta t = 0.4$ and $\Delta t = 0.1$.

between surge and heave even for a cambered Joukowski foil.

The vortex convection velocities in $\mathcal{Z}_2$, given by (3.23), are expensive to calculate. However, these velocities are needed to perform the simulation in the first place, so there is no extra effort required for the force calculation.

Figure 3-9 shows a typical time history for the expression in square brackets in (3.36), whose time derivative we need to calculate forces. At the beginning of every time step, a new vortex is released and this sum makes a jump, which can be found to be of order $\Delta t^{3/2}$. It now becomes clear why it is important to take the growing number of vortices into account when the time derivative is taken. If we fail to do this, we effectively calculate the slope as marked by "1" in Figure 3-9, whereas the correct way consistently uses the values at either the beginning or end of each time step, marked "2". Method 1 will still converge as the time step is reduced, but only at a rate $\sqrt{\Delta t}$.

Using method 2 with a central difference gives the time derivative at intermediate times, $t = (n + 1/2)\ \Delta t$. The values for Γ, $\mathcal{Z}_1$, and $\mathcal{Z}_2$ are available at times that are integer multiples of the time step in the simulation, $t = n\ \Delta t$. To form the force we must then linearly interpolate Γ, $\mathcal{Z}_1$, and $\mathcal{Z}_2$ to $t = (n + 1/2)\ \Delta t$. The added mass forces can be exactly evaluated for any t, and are added. This is a more precise calculation than taking the central difference over two time steps and adding

at $t = n\ \Delta t$.

Figure 3-10 shows how this calculation compares for an impulsively started flat plate at a small angle of attack, α_0. Lift and drag has been made nondimensional by $2\pi U^2 c\alpha_0$ and $U^2 c\alpha_0^2$, respectively. We note that the results converge everywhere except at $t = 0$, as could be expected from the analysis of the pressure distribution.

3.9 Moment

The counterclockwise moment on the foil about the point $z = 0$ is seen to be

$$M = Re\left\{\int_S pzd\overline{z}\right\} \tag{3.45}$$

Using the same technique as in the force calculation, we have from [75]:

$$\begin{aligned} M &= Re\left\{-\frac{d}{dt}\int_S \phi z d\overline{z} - \frac{1}{2}\int_S (u'^2 + v'^2) z d\overline{z} + \frac{1}{2}\int_S |W + i\Omega z|^2 z d\overline{z}\right\} \\ &= Re\left\{-\frac{d}{dt}\left[\int_S w z d\overline{z} + 3i\overline{W} z_c A + 2\Omega r_g^2 A\right]\right. \\ &\quad \left. -\frac{1}{2}\int_S \left[\frac{dw}{dz} - \overline{W} + i\Omega\overline{z}\right]^2 z dz + \Omega\overline{W} z_c A\right\} \\ &= Re\left\{-\frac{d}{dt}\int_S w z d\overline{z} - 3i\dot{\overline{W}} z_c A - 2\dot{\Omega} r_g^2 A\right. \\ &\quad \left. -\frac{1}{2}\int_S \left(\frac{dw}{dz}\right)^2 z dz + \overline{W}\int_S z dw + \Omega\overline{W} z_c A\right\} \end{aligned} \tag{3.46}$$

where again, we denote the integrals (I), (II) and (III) respectively. Note that additive constants in w will give a contribution to (I), so it is important to formulate all the potentials w_i so that the boundary condition (3.12) holds. The first integrand is not analytic, and the contour decomposition that we used in the force calculation is not applicable here, no general expression equivalent to (3.34) exists. Instead, the mapping function will be substituted for z and the integral evaluated on the map circle C, where we may use the fact that $\overline{\zeta} = r_c^2/\zeta$. But first, (I) is further broken

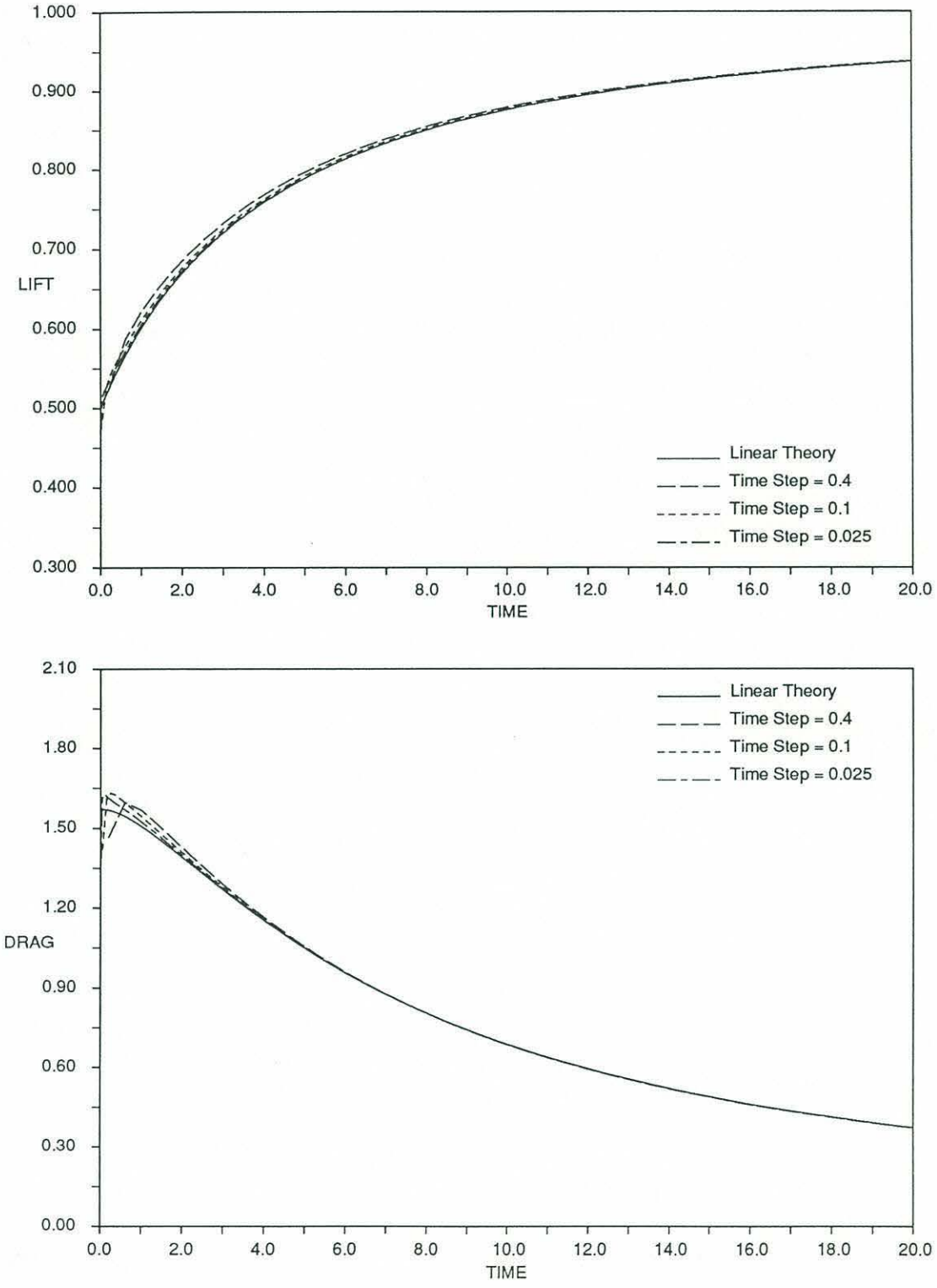

Figure 3-10: Forces on an impulsively started flat plate.

down into 5 parts:

$$\int_S wzd\overline{z} = U\int_S w_1 zd\overline{z} + V\int_S w_2 zd\overline{z} + \Omega\int_S w_3 zd\overline{z} + \gamma_c\int_S w_4 zd\overline{z} + \gamma_k\int_S w_5 zd\overline{z}$$

We shall refer to these intgrals as (I a) through (I e).

(I a)

$$\begin{aligned}
\int_S w_1 zd\overline{z} &= \int_C w_1 F(\zeta)\overline{F'(\zeta)d\zeta} \\
&= \int_C \left(-\frac{r_c^2}{\zeta} + \zeta_c + \frac{a^2}{\zeta+\zeta_c}\right)\left(\zeta + \zeta_c + \frac{a^2}{\zeta+\zeta_c}\right)\left(1 - \frac{a^2}{\overline{\zeta}+\overline{\zeta}_c}\right)d\overline{\zeta} \\
&= \int_C \left(-\frac{r_c^2}{\zeta} + \zeta_c + \frac{a^2}{\zeta+\zeta_c}\right)\left(\zeta + \zeta_c + \frac{a^2}{\zeta+\zeta_c}\right)\left(-\frac{r_c^2}{\zeta^2} + \frac{a^2 r_c^2}{(r_c^2+\overline{\zeta}_c\zeta)^2}\right)d\zeta \\
&= 2\pi i\left[-a^2\zeta_c + a^4\overline{\zeta}_c\left(\frac{1}{r_c^2-\delta^2} + \frac{r_c^2}{(r_c^2-\delta^2)^2}\right)\right. \\
&\quad \left. -2\frac{a^6 r_c^2}{(r_c^2-\delta^2)^3}\overline{\zeta}_c - r_c^2\zeta_c + \frac{a^4 r_c^2}{(r_c^2-\delta^2)^2}\zeta_c\right] \qquad (3.47)
\end{aligned}$$

In the last step, the integrand was expanded out in 12 terms that were individually evaluated by the residue theorem.

(I b)

$$\begin{aligned}
\int_S w_2 zd\overline{z} = 2\pi&\left[a^2\zeta_c - a^4\overline{\zeta}_c\left(\frac{1}{r_c^2-\delta^2} + \frac{r_c^2}{(r_c^2-\delta^2)^2}\right)\right. \\
&\left. -2\frac{a^6 r_c^2}{(r_c^2-\delta^2)^3}\overline{\zeta}_c - r_c^2\zeta_c + \frac{a^4 r_c^2}{(r_c^2-\delta^2)^2}\zeta_c\right] \qquad (3.48)
\end{aligned}$$

(I c)

$$\begin{aligned}
\int_S w_3 zd\overline{z} &= 2\pi\left[a^4 + a^2\zeta_c^2 + a^4\frac{\delta^4 - 2r_c^2\delta^2}{(r_c^2-\delta^2)^2} + \frac{a^6\overline{\zeta}_c^2}{(r_c^2-\delta^2)^2}\right. \\
&\quad \left. + \frac{2a^8 r_c^2\delta^2}{(r_c^2-\delta^2)^4} - r_c^2\frac{a^4 + r_c^4 - \delta^4}{2(r_c^2-\delta^2)} + a^4 r_c^2\frac{a^4 + r_c^4 - \delta^4}{(r_c^2-\delta^2)^3}\right] \qquad (3.49)
\end{aligned}$$

(I d) is difficult to evaluate, and in fact there is no need to. By arguing that a vortex introduced far away should not affect the integral (I), we can set (I d)= $-\lim_{\zeta_k\to\infty}$(I e).

(I e) Expanding out, this integral can be written:

$$\int_C i \log \frac{-r_c(\zeta-\zeta_k)}{\zeta_k(\zeta - r_c^2/\overline{\zeta}_k)} \left[-\frac{r_c^2}{\zeta} - \frac{r_c^2\zeta_c}{\zeta^2} - \frac{a^2 r_c^2}{\zeta^2(\zeta+\zeta_c)} + \frac{a^2 r_c^2 \zeta}{(r_c^2+\overline{\zeta}_c\zeta)^2} + \frac{a^2 r_c^2 \zeta_c}{(r_c^2+\overline{\zeta}_c\zeta)^2} + \frac{a^4 r_c^2}{(\zeta+\zeta_c)(r_c^2+\overline{\zeta}_c\zeta)^2} \right] d\zeta$$

Let $g(\zeta)$ denote the integrand. A partial fraction expansion of the 3rd and 6th term in the square brackets yields, after collecting terms:

$$g(\zeta) = i \log \frac{-r_c(\zeta-\zeta_k)}{\zeta_k(\zeta - r_c^2/\overline{\zeta}_k)} \left[\frac{\mathcal{A}}{\zeta} + \frac{\mathcal{B}}{\zeta^2} + \frac{\mathcal{C}}{\zeta+\zeta_c} + \frac{\mathcal{D}}{\zeta + r_c^2/\overline{\zeta}_c} + \frac{\mathcal{E}+\mathcal{F}\zeta}{(\zeta + r_c^2/\overline{\zeta}_c)^2} \right]$$

where

$$\begin{aligned}
\mathcal{A} &= -r_c^2 + r_c^2 \frac{a^2}{\zeta_c^2} \\
\mathcal{B} &= -r_c^2\zeta_c - r_c^2 \frac{a^2}{\zeta_c} \\
\mathcal{C} &= -\frac{r_c^2 a^2}{\zeta_c^2} + \frac{r_c^2 a^4}{(r_c^2-\delta^2)^2} \\
\mathcal{D} &= -\frac{r_c^2 a^4}{(r_c^2-\delta^2)^2} \\
\mathcal{E} &= -\frac{r_c^2 a^4}{(r_c^2-\delta^2)\overline{\zeta}_c} + \frac{r_c^2 a^2 \zeta_c}{\overline{\zeta}_c^2} \\
\mathcal{F} &= \frac{r_c^2 a^2}{\overline{\zeta}_c^2}
\end{aligned}$$

It is now apparent that g has a pole at $\zeta = -r_c^2/\overline{\zeta}_c$, in addition to the singularities inside C and at ζ_k. The integration contour in the ζ plane is shown in Figure 3-11. The branch cut between the vortex and its image runs inside C_b, which intersects C at the point that maps onto the trailing edge, $\zeta = a - \zeta_c$. C_p surrounds the pole at $-r_c/\overline{\zeta}_c$, and the contour is closed at a large distance by C_∞. We have

$$\int_C = \int_{C_\infty} - \int_{C_p} - \int_{C_b}$$

The vortex at ζ_k has a logarithmic singularity, which is too weak to give a contribution

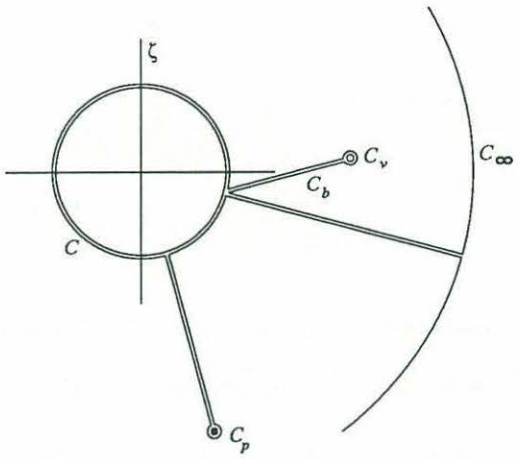

Figure 3-11: Integration contour for moment.

as C_v shrinks.

The terms of g that go like $1/\zeta$ in the far field are easily identified, and we get the following contribution from C_∞:

$$\int_{C_\infty} g(\zeta)d\zeta = -2\pi(\mathcal{A}+\mathcal{C}+\mathcal{D}+\mathcal{F})\log\frac{-r_c}{\zeta_k}$$

The contribution from C_p is found from the residue of a first and second order pole:

$$\begin{aligned}\int_{C_p} g(\zeta)d\zeta &= 2\pi i\left\{\mathcal{D}i\log\frac{-r_c(\zeta-\zeta_k)}{\zeta_k(\zeta-r_c^2/\overline{\zeta}_k)}+\frac{d}{d\zeta}\left[(\mathcal{E}+\mathcal{F}\zeta)i\log\frac{-r_c(\zeta-\zeta_k)}{\zeta_k(\zeta-r_c^2/\overline{\zeta}_k)}\right]\right\}_{\zeta=-r_c^2/\overline{\zeta}_c}\\ &= -2\pi\left[(\mathcal{D}+\mathcal{F})\log\frac{-r_c(r_c^2/\overline{\zeta}_c+\zeta_k)}{\zeta_k(r_c^2/\overline{\zeta}_c+r_c^2/\overline{\zeta}_k)}\right.\\ &\quad\left.+\left(\mathcal{E}-\mathcal{F}r_c^2/\overline{\zeta}_c\right)\left(-\frac{1}{r_c^2/\overline{\zeta}_c+\zeta_k}+\frac{1}{r_c^2/\overline{\zeta}_c+r_c^2/\overline{\zeta}_k}\right)\right]\end{aligned}$$

The contribution from C_b can be evaluated using the fact that the logarithmic term in $g(\zeta)$ makes a jump of 2π from the upper to the lower bank of C_b. Thus

$$\int_{C_b} g(\zeta)d\zeta = \int_{a-\zeta_c}^{\zeta_k} 2\pi\left[\frac{\mathcal{A}}{\zeta}+\frac{\mathcal{B}}{\zeta^2}+\frac{\mathcal{C}}{\zeta+\zeta_c}+\frac{\mathcal{D}}{\zeta+r_c^2/\overline{\zeta}_c}+\frac{\mathcal{E}+\mathcal{F}\zeta}{(\zeta+r_c^2/\overline{\zeta}_c)^2}\right]d\zeta$$

This is a sum of elementary line integrals in ζ, running from $a-\zeta_c$ to ζ_k. The last

term is conveniently evaluated by integrating by parts, and we have:

$$\begin{aligned}\int_{C_b} g(\zeta)d\zeta &= 2\pi\mathcal{A}\log\frac{\zeta_k}{a-\zeta_c} - 2\pi\mathcal{B}\left(\frac{1}{\zeta_k}-\frac{1}{a-\zeta_c}\right) + 2\pi\mathcal{C}\log\frac{\zeta_c+\zeta_k}{a} \\ &+ 2\pi(\mathcal{D}+\mathcal{F})\log\frac{r_c^2/\overline{\zeta}_c+\zeta_k}{a-\zeta_c+r_c^2/\overline{\zeta}_c} - 2\pi\frac{\mathcal{E}+\mathcal{F}\zeta_k}{\zeta_k+r_c^2/\overline{\zeta}_c} + 2\pi\frac{\mathcal{E}+\mathcal{F}(a-\zeta_c)}{a-\zeta_c+r_c^2/\overline{\zeta}_c}\end{aligned}$$

Then, all the terms can be collected to find the integral (Ie):

$$\begin{aligned}\int_S w_5 z d\overline{z} &= 2\pi\mathcal{A}\log\frac{\zeta_c-a}{r_c} + 2\pi\mathcal{B}\left(\frac{1}{\zeta_k}-\frac{1}{a-\zeta_c}\right) - 2\pi\mathcal{C}\log\frac{-r_c(\zeta_c+\zeta_k)}{a\zeta_k} \\ &+ 2\pi\mathcal{D}\log\frac{a-\zeta_c+r_c^2/\overline{\zeta}_c}{r_c^2/\overline{\zeta}_c+r_c^2/\overline{\zeta}_k} + 2\pi\mathcal{E}\left(\frac{1}{r_c^2/\overline{\zeta}_c+r_c^2/\overline{\zeta}_k}-\frac{1}{a-\zeta_c+r_c^2/\overline{\zeta}_c}\right) \\ &+ 2\pi\mathcal{F}\left(\log\frac{a-\zeta_c+r_c^2/\overline{\zeta}_c}{r_c^2/\overline{\zeta}_c+r_c^2/\overline{\zeta}_k}+1-\frac{\overline{\zeta}_k}{\overline{\zeta}_k+\overline{\zeta}_c}-\frac{a-\zeta_c}{a-\zeta_c+r_c^2/\overline{\zeta}_c}\right) \qquad (3.50)\end{aligned}$$

Upon taking the real part, the logarithmic terms cancel. This should come as no surprise, since the logarithm is a multivalued function. Now, employing the relation

$$r_c^2 = (a-\zeta_c)(a-\overline{\zeta}_c)$$

we get

$$\begin{aligned}Re\left\{\int_S w_5 z d\overline{z}\right\} &= 2\pi Re\left\{\mathcal{B}\left(\frac{1}{\zeta_k}-\frac{1}{a-\zeta_c}\right)+\mathcal{E}\left(\frac{1}{r_c^2/\overline{\zeta}_c+r_c^2/\overline{\zeta}_k}-\frac{\overline{\zeta}_c}{a(a-\zeta_c)}\right)\right. \\ &\left.+\mathcal{F}\left(\frac{\overline{\zeta}_c}{\overline{\zeta}_k+\overline{\zeta}_c}-\frac{\overline{\zeta}_c}{a}\right)\right\} \qquad (3.51)\end{aligned}$$

$\mathcal{B},\mathcal{E},\mathcal{F}$ blow up as $\zeta_c \to 0$, so this expression is not suitable for the special case of a flat plate. With this in mind, we can substitute and contract terms until we reach the following result:

$$\begin{aligned}Re\left\{\int_S w_5 z d\overline{z}\right\} &= 2\pi Re\left\{\frac{-r_c^2\zeta_c}{\zeta_k}-\frac{a^2r_c^2}{\zeta_k(\zeta_k+\zeta_c)}+a^2-\delta^2\right. \\ &\left.-\frac{a^4\zeta_c}{(\delta^2-r_c^2)(\overline{\zeta}_k+\overline{\zeta}_c)}-\frac{a^2\overline{\zeta}_c}{\zeta_k+\zeta_c}+a\zeta_c+\frac{a^3\zeta_c}{\delta^2-r_c^2}\right\} \qquad (3.52)\end{aligned}$$

(I d) Letting $\zeta_k \to \infty$ in the above expression yields the integral (I d):

$$Re\left\{\int_S w_4 z d\overline{z}\right\} = -2\pi Re\left\{a^2 - \delta^2 + a\zeta_c + \frac{a^3\zeta_c}{\delta^2 - r_c^2}\right\} \tag{3.53}$$

(II) The second integral in (3.46) can be evaluated by separating out the singular part of w at ζ_k the same way as in the case of force. The result is:

$$\int_S \left(\frac{dw}{dz}\right)^2 z dz = 4\pi\gamma_k \frac{d\overline{z}_k}{dt} z_k \tag{3.54}$$

(III) The third integral was found in the force calculation:

$$\begin{aligned}\int_S \frac{dw}{dz} z dz \;=\; & 2\pi\left[iU(r_c^2 - a^2) - V(r_c^2 + a^2) - \Omega\left(r_c^2\zeta_c + a^2\overline{\zeta}_c - \frac{a^4}{r_c^2 - \delta^2}\zeta_c\right)\right. \\ & \left. + \gamma_c\zeta_c + \gamma_k\left(\frac{r_c^2}{\overline{\zeta}_k} - \zeta_k + z_k'\right)\right]\end{aligned} \tag{3.55}$$

The moment can now be written in closed form:

$$\begin{aligned}M \;=\; & -\dot{U}\pi\left[2a^2 - r_c^2 + 2\frac{a^4}{r_c^2 - \delta^2} - \frac{r_c^2 a^6}{(r_c^2 - \delta^2)^3}\right]\delta_I \\ & - \dot{V}\pi\left[2a^2 + r_c^2 - 2\frac{a^4}{r_c^2 - \delta^2} - \frac{r_c^2 a^6}{(r_c^2 - \delta^2)^3}\right]\delta_R \\ & - \dot{\Omega}\pi\left[2a^4 + 2a^2(\delta_R^2 - \delta_I^2) + 2a^4\frac{\delta^4 + a^2(\delta_R^2 - \delta_I^2) - 2r_c^2\delta^2}{(r_c^2 - \delta^2)^2}\right. \\ & \qquad \left. + a^8 r_c^2\frac{2\delta^2 - r_c^2}{(r_c^2 - \delta^2)^4} - \frac{r_c^2 a^4}{r_c^2 - \delta^2} + r_c^2\delta^2 + a^4 r_c^2\frac{a^4 + r_c^4 - \delta^4}{(r_c^2 - \delta^2)^3}\right] \\ & - U\Omega\pi\left[2a^2 + r_c^2 - 2\frac{a^4}{r_c^2 - \delta^2} - \frac{r_c^2 a^6}{(r_c^2 - \delta^2)^3}\right]\delta_R \\ & + V\Omega\pi\left[2a^2 - r_c^2 + 2\frac{a^4}{r_c^2 - \delta^2} - \frac{r_c^2 a^6}{(r_c^2 - \delta^2)^3}\right]\delta_I \\ & + UV2\pi\left[r_c^2 + \frac{r_c^2 a^4}{(r_c^2 - \delta^2)^2}\right] \\ & + 2\pi\dot{\gamma}_c Re\left\{a^2 - \delta^2 + a\zeta_c + \frac{a^3\zeta_c}{\delta^2 - r_c^2}\right\} \\ & - 2\pi\frac{d}{dt}\sum_k \gamma_k Re\left\{\frac{-r_c^2\zeta_c}{\zeta_k} - \frac{a^2 r_c^2}{\zeta_k(\zeta_k + \zeta_c)} + a^2 - \delta^2\right.\end{aligned}$$

$$
\begin{aligned}
& -\frac{a^4\zeta_c}{(\delta^2-r_c^2)(\overline{\zeta}_k+\overline{\zeta}_c)}-\frac{a^2\overline{\zeta}_c}{\zeta_k+\zeta_c}+a\zeta_c+\frac{a^3\zeta_c}{\delta^2-r_c^2}\Bigg\} \\
- \quad & 2\pi\sum_k \gamma_k Re\left\{\frac{d\overline{z}_k}{dt}z_k\right\} \\
+ \quad & 2\pi Re\left\{\overline{W}\left[\gamma_c\zeta_c+\sum_k\gamma_k\left(\frac{r_c^2}{\overline{\zeta}_k}-\zeta_k+z_k'\right)\right]\right\} \qquad (3.56)
\end{aligned}
$$

In a more compact form:

$$
\begin{aligned}
M \quad = \quad & -\dot{U}m_{61}-\dot{V}m_{62}-\dot{\Omega}m_{66}-U^2m_{21}+V^2m_{12} \\
& +UV(m_{11}-m_{22})-U\Omega m_{26}+V\Omega m_{16} \\
& +\frac{d}{dt}\left[2\pi\mathcal{S}_1-\Gamma\left(a^2-\delta^2+a\zeta_c+\frac{a^3\zeta_c}{\delta^2-r_c^2}\right)\right] \\
& -2\pi\mathcal{S}_2+Re\{\overline{W}(2\pi\mathcal{Z}_3-\Gamma\zeta_c)\} \qquad (3.57)
\end{aligned}
$$

where

$$
\begin{aligned}
m_{61} \quad &= \quad m_{16} \qquad (3.58) \\
m_{62} \quad &= \quad m_{26} \qquad (3.59) \\
m_{66} \quad &= \quad \pi\Bigg[2a^4+2a^2(\delta_R^2-\delta_I^2)+2a^4\frac{\delta^4+a^2(\delta_R^2-\delta_I^2)-2r_c^2\delta^2}{(r_c^2-\delta^2)^2} \\
& \qquad +a^8r_c^2\frac{2\delta^2-r_c^2}{(r_c^2-\delta^2)^4}-\frac{r_c^2a^4}{r_c^2-\delta^2}+r_c^2\delta^2+a^4r_c^2\frac{a^4+r_c^4-\delta^4}{(r_c^2-\delta^2)^3}\Bigg] \qquad (3.60) \\
\mathcal{S}_1 \quad &= \quad \sum_k\gamma_k Re\left\{\frac{r_c^2\zeta_c}{\zeta_k}+\frac{a^2r_c^2}{\zeta_k(\zeta_k+\zeta_c)}+\frac{a^4\zeta_c}{(\delta^2-r_c^2)(\overline{\zeta}_k+\overline{\zeta}_c)}+\frac{a^2\overline{\zeta}_c}{\zeta_k+\zeta_c}\right\} \qquad (3.61) \\
\mathcal{S}_2 \quad &= \quad 2\pi\sum_k\gamma_k Re\left\{\frac{d\overline{z}_k}{dt}z_k\right\} \qquad (3.62) \\
\mathcal{Z}_3 \quad &= \quad 2\pi\sum_k\gamma_k\left(\frac{r_c^2}{\overline{\zeta}_k}+\frac{a^2}{\zeta_k+\zeta_c}\right) \qquad (3.63)
\end{aligned}
$$

Figure 3-12 shows that this calculation compares nicely with linear theory for an impulsively started flat plate at a small angle of attack.

In addition to comparisons with linear theory for a flat plate, the algorithm has also been verified versus direct numerical integration of the pressure. The results agree to whatever accuracy we are able to evaluate the integrals numerically.

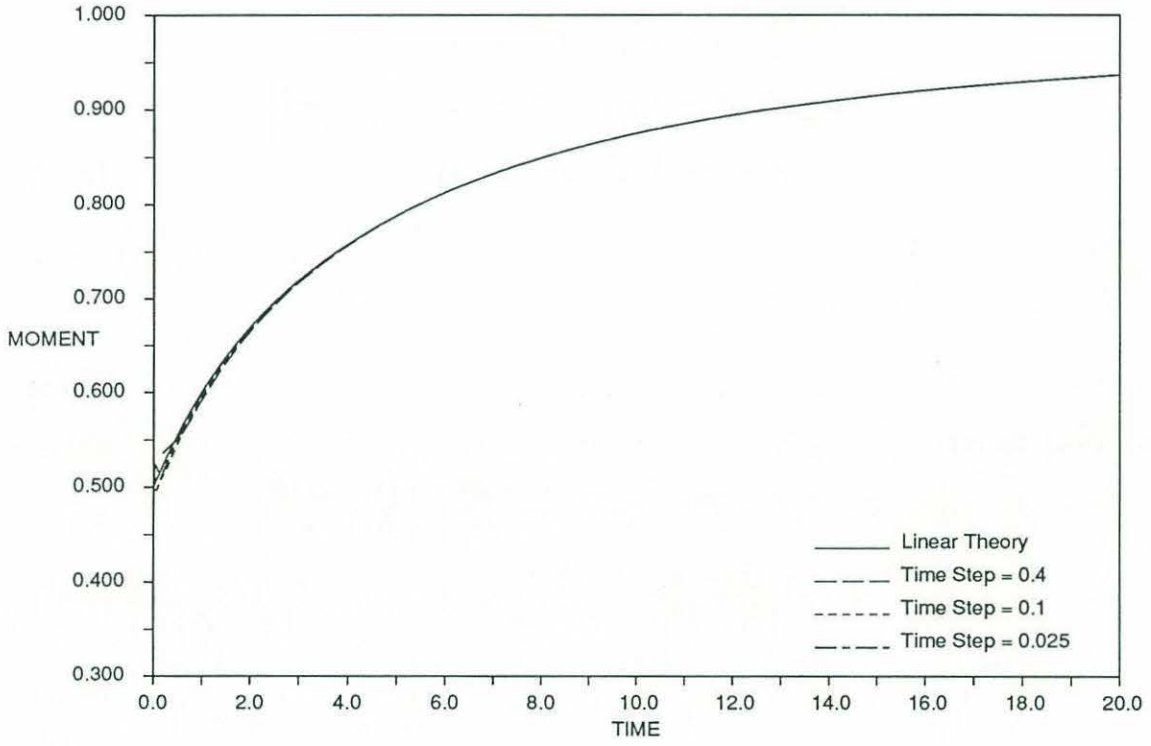

Figure 3-12: Moment on an impulsively started flat plate normalized by its steady state value, $\pi U^2 c^2 \alpha_0$.

3.10 Comments

Let us conclude this chapter with a summary of the principal differences from previous work.

- A careful formulation of the unit potentials allows us to introduce arbitrary vortices in addition to those shed at the trailing edge.
- The algorithm for vortex shedding contains no disposable parameters that must be calibrated [63].
- Other two–dimensional potential flow calculations are more general than the present one, for instance Choi and Landweber [16] which uses a completely general profile shape and Lam [42] which allows a descripition of the wake as vortex segments. However, these rely on numerical integration on the foil surface for force and moment calculation.
- The profile shape is a general Joukowski foil, compared to a flat plate in [62] and [48], and a general power series transform in [30].
- The profile is allowed to perform arbitrary motion in a fluid at rest. This is more general than flow over a stationary profile in [62, 30], which is kinematically equivalent in the case of translation, but precludes treatment of rotation.
- The influence of a growing number of vortices have been retained in the time derivatives, removing an $O(\sqrt{\Delta t})$ error, where Δt is the time step of the simulation.

Chapter 4

Simulation Results

4.1 A comparison with experiment for uniform inflow

At the MIT Ocean Engineering testing facility, my colleague David Barett has performed a series of oscillating foil experiments in a flow without an oncoming vortex street. In this section we will compare the results from two of these experiments with the numerical computations described in the previous chapter, as well as the classical linear theory.

A sketch of the testing apparatus can be seen in Figure 4-1; basically a pair of streamlined struts are connected to a towed carriage via a lead screw assembly, permitting an arbitrary heave motion to be performed as the complete rig advances. A second motor drives a transmission chain that actuates the foil in the pitch degree of freedom. The foil is sufficiently submerged to avoid free surface effects, while the driving motors are located out of the water. The force transducer is located at the foil pivot point, whereas torque is measured at the pitch motor. Triantafyllou & al. [77, 76] and Gopalkrishnan [28] has a fuller description of the testing apparatus, the force and moment measurement techniques, and the hardware and software used to control the experiment and process the data.

Table 4.1 lists all the pertinent information about the foil profile and the motion

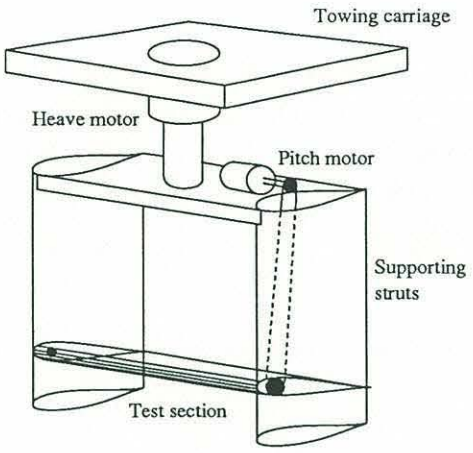

Figure 4-1: Experimental rig for oscillating foil.

Table 4.1: Parameters for experimental run.

Run	nov1413	nov2916
Profile	NACA0012	NACA0012
Chord length, $2c$	0.100 m	0.100 m
Span	0.600 m	0.600 m
Fluid density	1000 kg/m^3	1000 kg/m^3
Forward speed, U_0	0.40 m/s	0.40 m/s
Frequency, ω	3.353 s^{-1}	3.987 s^{-1}
Heave amplitude	0.0800 m	0.0792 m
Pitch amplitude	0.3125 rad	0.587 rad
Pitch point	$2c/3$ from l.e.	$2c/3$ from l.e.

that was specified for the runs in our comparison. In the experiments, each run was denoted by date and sequential numbers, this nomenclature has been retained here. The parameters that determine foil geometry in the numerical simulation are listed in Table 4.2. With these input variables, we obtain a profile shape with the same chord and thickness as the experimental one. In figure 4-2, the two of them are compared. We note that the Joukowski foil is somewhat fuller in the leading edge and thinner towards the trailing edge.

Table 4.2: Parameters for numerical simulation.

Circle intersection w. x-axis, a	0.02476 m
Circle center, ζ_c	-0.00253 m
Location of pitch point, b	-0.01717 m
Time step Δt	0.02 s

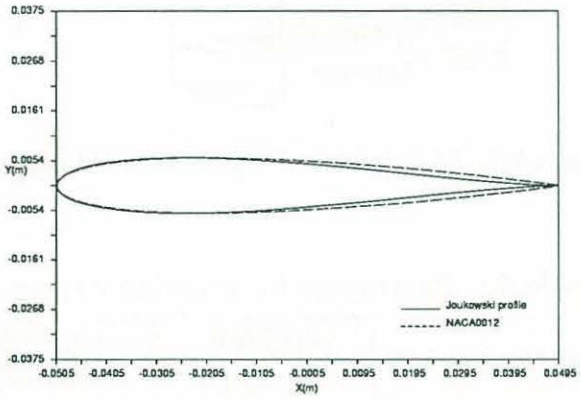

Figure 4-2: Profile shapes.

4.1.1 Experimental run "nov1413"

The reason for choosing this particular run for comparison, was that it gave a high propulsive efficiency. Figure 4-3 shows a representative portion of the force and moment time series obtained in the experiment, compared to numerical simulation and linear theory. It is assumed that the transient effects have died out at $t = 0$ in the experimental record, but the simulation commences at this time.

The thrust force obtained in the experiment has a significant fundamental harmonic component, indicating that some kind of asymmetry is present in the experimental setup. It could for instance be due to a slightly misaligned force transducer, causing a part of the lift force to bleed into the thrust record. Furthermore, we note that the numerical simulation yields large amplitude forces over the initial period of simulation. Subsequently it agrees well with linear theory, indicating that the nonlinear effects are modest, even for this large amplitude motion. Both simulation and theory predicts thrust fluctuation amplitudes somewhat lower than the experiment.

Most of the data records from the experiment have some non–zero reading when

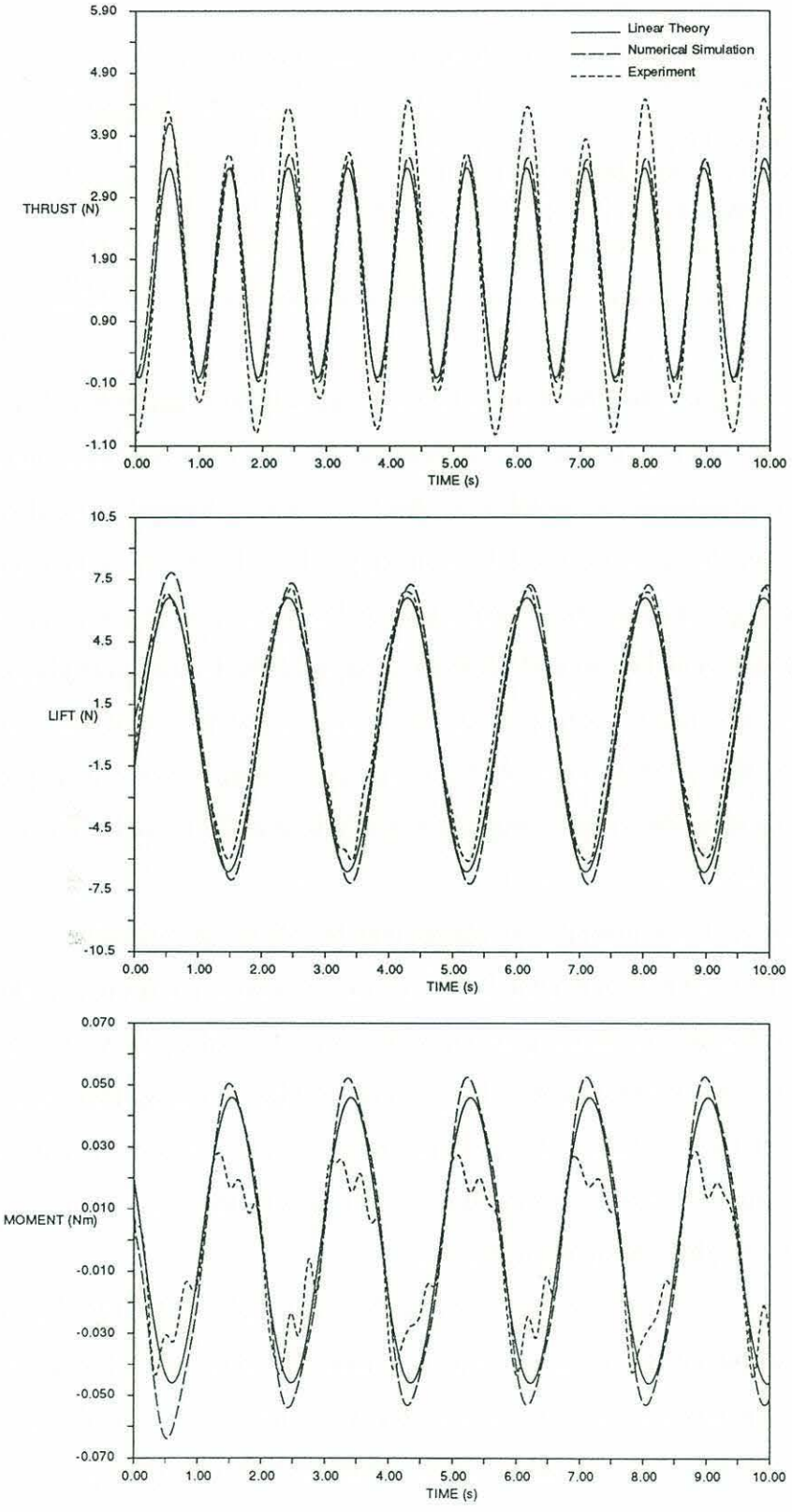

Figure 4-3: Force and moment records.

Table 4.3: Foil performance for "nov1413".

	Theory	Simulation	Experiment
Mean thrust (N)	1.69	1.71	1.62
Mean power input, heave (W)	0.875	0.918	0.822
Mean power input, pitch (W)	-0.0104	-0.0126	-0.001
Mean power input, total (W)	0.865	0.905	0.821
Efficiency	0.780	0.756	0.790

the foil is not moving, i.e. before or after the run. For lift and moment, this is of no concern, because we can add a constant to these so that the expected zero mean value results. In any event a mean error will not affect the energy budget. For thrust, the situation is different, because we must be able to predict the mean value accurately. It is difficult to correct for the static reading from the force transducer, because this value is typically different before and after the run, and fluctuates over shorter time scales also. Here, the mean correction to the thrust force record is such that the result agrees with the original analysis that was performed when the experiments were done. In this case the mean thrust is slightly below that predicted by theory and simulation.

The results for lift force are in close agreement for all three methods.

The moment from the experiment has a third harmonic component, causing a clipped down amplitude. According to Dave Barrett, the pitch drive train suffers from some low frequency resonance, which must be the cause of this error. The interesting thing is that it causes a reduction and not an increase in the moment amplitude. The simulation and theory agrees well also in the case of moment, the simulation giving a slightly higher amplitude.

Mean thrust, power input, and efficiency is shown in Table 4.3. The heave input power is simply negative the vertical velocity times lift force, and the pitch input power is negative the angular velocity times moment. The efficiency is defined as the thrust times forward velocity divided by total input power, as in (2.41).

We see that the discrepancy in the moment is of little significance, as the energy required for the pitch motion is negligible.

Table 4.4: Foil performance for "nov2916".

	Theory	Simulation	Experiment
Mean thrust (N)	1.082	0.609	0.350
Mean power input, heave (W)	0.591	0.399	0.505
Mean power input, pitch (W)	-0.0266	0.0649	0.0067
Mean power input, total (W)	0.564	0.609	0.506
Efficiency	0.767	0.526	0.279

In conclusion we can say that all the methods give a propulsive efficiency of 75% or more. This is higher than previous experiments have shown [64, 5, 21].

4.1.2 Experimental run "nov2916"

This example differs from the previous one mainly in the higher value of the feathering parameter, 0.74 versus 0.47. This means that the attitude of the foil is closer to the tangent of its own path, which reduces the loads. The example was chosen because the efficiency obtained in the experiment was substantially below that predicted by linear theory. Comparing with experiment, we hope to clarify how much of this can be attributed to nonlinear effects. Figure 4-4 shows a representative portion of the force and moment time series obtained in the experiment, compared to numerical simulation and linear theory, and Table 4.4 lists the average values.

The thrust force in the experiments has a larger amplitude and a smaller mean value than the theoretical one. This seems to be partly a nonlinear effect. Intuitively one would also expect the viscous drag on the foil to be relatively more important in this case, since the foil is gliding through the water at smaller local angles of attack.

The lift force is somewhat larger for the numerical simulation, this may have to do with the prescribed motion of the foil. (3.1) corresponds to the foil pitching about $z = 0$ with different phase angles relative to the heave, and this corresponds to pitch about an arbitrary point b only for small motions. It can be shown that the lift amplitude is rather sensitive to the exact value of b for this case, which indicates that the discrepancy could be due to a small difference in foil motion. We also note that

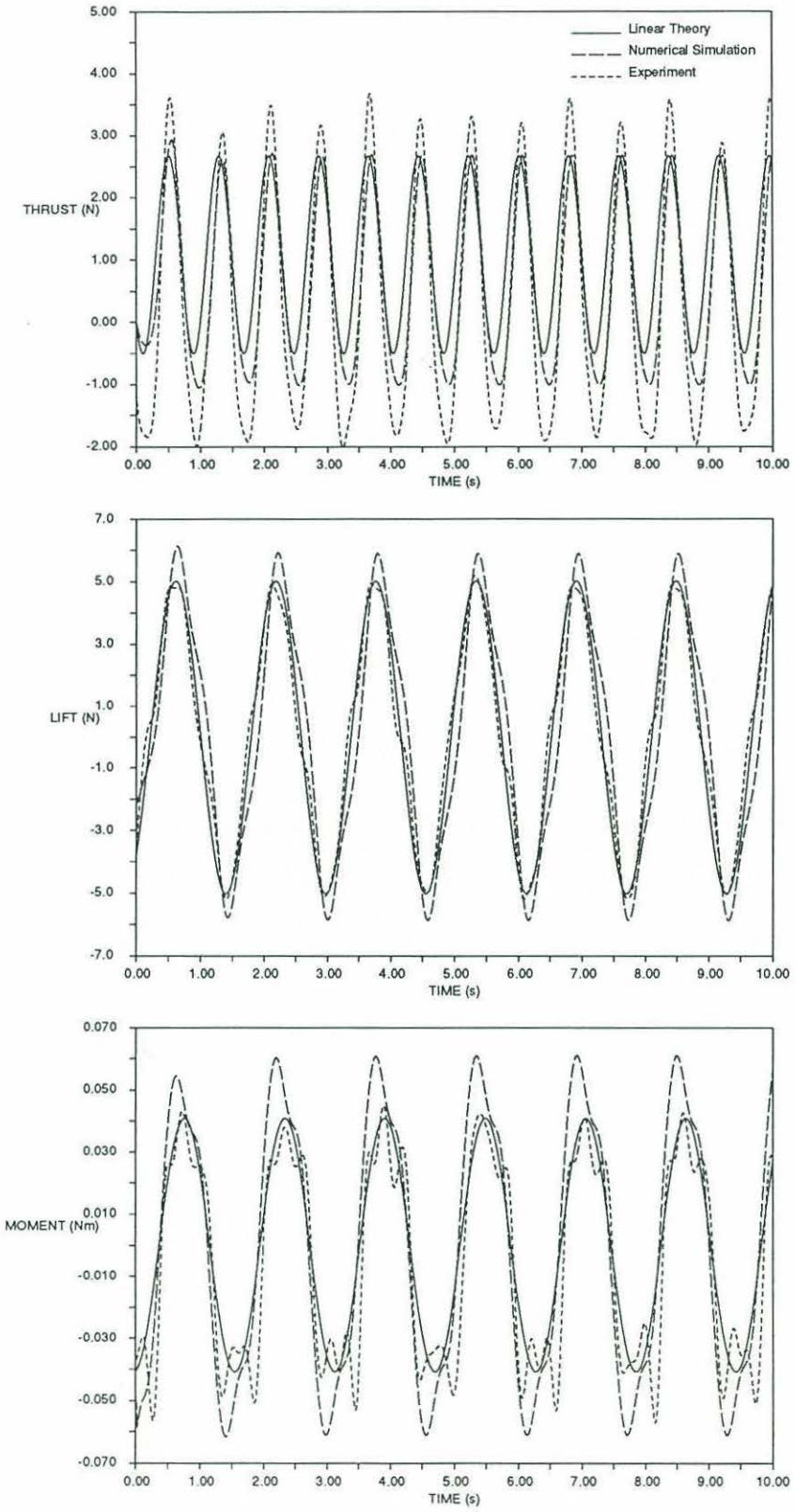

Figure 4-4: Force and moment records.

the mean input power is very sensitive to the lift force record. Lift for experiment and theory are apparently very close, yet the mean lift power differs by 20 %.

We see some important nonlinear effect in the moment record, but again, this is insignificant in the energy budget.

It seems that the low efficiency in the experiment is caused mainly by a low mean thrust force, due to nonlinear effects and viscous drag.

4.1.3 Very high efficiency runs

In experiments that were performed later, the effect of changing the pitch point, or equivalently the phase between heave and pitch, was investigated. Generally, when the pitch point is placed closer to the trailing edge, the efficiency improves. In some experiments the efficiency was as high as 87%, exceeding the value predicted by linear theory. To see if this could be explained by an inviscid model some extra simulation runs has been performed. The input is the same as for "nov1413", except for the location of the pitch point, which is now at the trailing edge. Simulation results show 79.6% efficiency, whereas linear theory predicts 81.0%. When heave and pitch amplitudes are reduced by a factor 10 in the simulation, efficiency goes up to 80.1%. When the foil is replaced by a flat plate, we get 81.0%, which agrees with linear theory, as it should. When the frequency if oscillation is reduced, even higher efficiencies are seen, and the agreement between linear theory and simulation is better, even for large amplitude motion. I have never found a case where the efficiency in simulation exceeds that of linear theory. The conclusion to this is that a rearward shift of the pitch point can improve efficiency, but the remarkably high values seen in the experiment is not seen in nonlinear inviscid simulation.

4.2 How the oncoming vortex street is generated in numerical simulation

In simulations, the Kármán vortex street is simulated by releasing vortices into a free stream at regular intervals, interacting with each other according to Biot–Savart's law. In the abcense of a foil, the motion of vortex m, say, is governed by

$$u_m - iv_m = U + \sum_{l \neq m} \frac{i\kappa_l}{z_m - z_l}$$

which may be simulated with the second order Runge Kutta method or some other suitable scheme. For most combinations of input variables, the vortex street forms nicely, without any sign of the instabilities that von Kármán predicted for the theoretical vortex street. There is sometimes a small contraction or widening of the street just downstream of the release points [80], but this is so minor that we consider q to be given by the vertical distance between the release points.

In simulations, it is impossible to specify the spatial period p, so the input parameters are U, q, κ, and ω. In Figure 2-3, we see that for a given $\kappa/(Uq)$ and $\omega q/U$, p/q may have none, 1 or 2 solutions[1]. It appears that the simulated vortex street always takes the largest of the two, in the cases where it forms properly.

For some combinations of input, typically when the vortices are very strong, a vortex street will not form. One of two things can happen; the rows of the vortex street roll up at the downstream end, or sawtooth mode instabilities develop in each of the two rows. The curious thing is that for another set of inputs, but with the same two nondimensional groups, $\omega q/U$ and $\kappa/(Uq)$, the wake may form again. So there are situations when inputs that are the same, nondimensionally speaking, leads to qualitatively different behavior. This must be due to the non–uniqueness of the period p for given U, q, κ, and ω.

In foil simulations, the oncoming vortices are in the form of clusters released upstream every half period at an ordinate $q/2$. These clusters have a total circulation

[1] This property, in a different formulation, was pointed out by Weihs [81].

of $2\pi\kappa$, and consist of 18 point vortices uniformly distributed within a circle of radius 0.3. The fact that the incoming vortices have a finite size is only important in very close interactions with the foil, in most cases we could just as well have used single vortices. The main advantage is that the straining of the incoming vortices can be observed during interaction with the foil. The vortex street is thought of as being caused by a bluff body upstream. In order to preserve a zero mean circulation around this imaginary body (which is reflected in the bound foil vorticity, as explained in Chapter 3), the first of the released vortices has only half strength.

When the upstream vortices are introduced to the flow, there is a jump in the potential, which leads to large amplitude spikes in the force and moment records. This amplitude becomes smaller as the release point is moved far upstream, because of the way the vortex potentals were formulated in Chapter 3. However, when the release point is moved further upstream, the simulations must run longer before the first vortices reach the foil, which is inefficient. The spikes are an artificial effect caused by the fact that we have essentially moved the vortex shedding body to infinity, while its vortices are released a finite distance from the foil.

Several schemes were tried to overcome this problem. The entire vortex street can be put in the flow initially, which eliminates the need to introduce upstream vortices later during simulation. When we tried this, it was difficult to obtain a steady, harmonic force record, because of end effects in the vortex street. The run time is also much longer with so many vortices in the flow already from the start. Next, we tried to introduce the vortices gradually, by releasing single vortices upstream at every time step. These would emanate from the release points like pearls on a string and roll up on account of their self interaction. It was difficult to make them roll up into tight clusters of vorticity, though. Finally, we tried to let the strength of upstream vortices grow linearly over one half period. That takes care of the spikes, but the artificial effect is now spread out over time, which affects the average force and moment.

Instead it we went back to the original scheme, releasing the vortices instantly at every half period, but when force and moment is calculated we do not attempt to

find the time derivatives at these instants. Instead an average of time derivatives at neighboring time steps is used. There is still an artifact in the force record due to the sudden introduction of upstream vortices, but the effect diminishes as we move the release points farther upstream. It was found that a distance of 30 half chords was adequately far away.

4.3 Comparison with a vortex – foil interaction experiment

In this section we shall perform numerical simulation for a foil oscillating in a vortex street in a case which has also been studied in flow visualization experiments, and thus be able to make a useful comparison of the velocity field in the wake of the foil. My colleague Jamie Anderson is using the Digital Particle Image Velocimetry technique to study the flow in this problem. The experimental technique is still being refined to minimize three–dimensional flow components, so we will only be making a qualitative comparison of the flow fields. Figure 4-5 is a typical example of the kind of results that is obtained in these experiments, the figure shows the instantaneous velocity field in the wake left behind a D – section cylinder that oscillates in the transverse direction as it progresses through the fluid. Gopalkrishnan [28] found that this is a good way to obtain a strong Kármán vortex street without the great frequency sensitivity seen when a circular cylinder is used. The orientation of the original data is reversed so that the picture corresponds to the cylinder moving from right to left, which is consistent with the other examples in this thesis. By integrating the tangential velocity on contours surrounding the vortices, we can determine the properties of the vortex street. The strength, size, and relative location of the vortices are listed in Table 4.5. With these vortex street parameters, the numerical simulation predicts the velocity field shown in Figure 4-6. Here the flow is purely two–dimensional and the vorticity is concentrated within circular regions, resulting in a velocity field that is somewhat better defined than in the experiment.

A foil was subsequently placed inside this vortex street, oscillating with motion

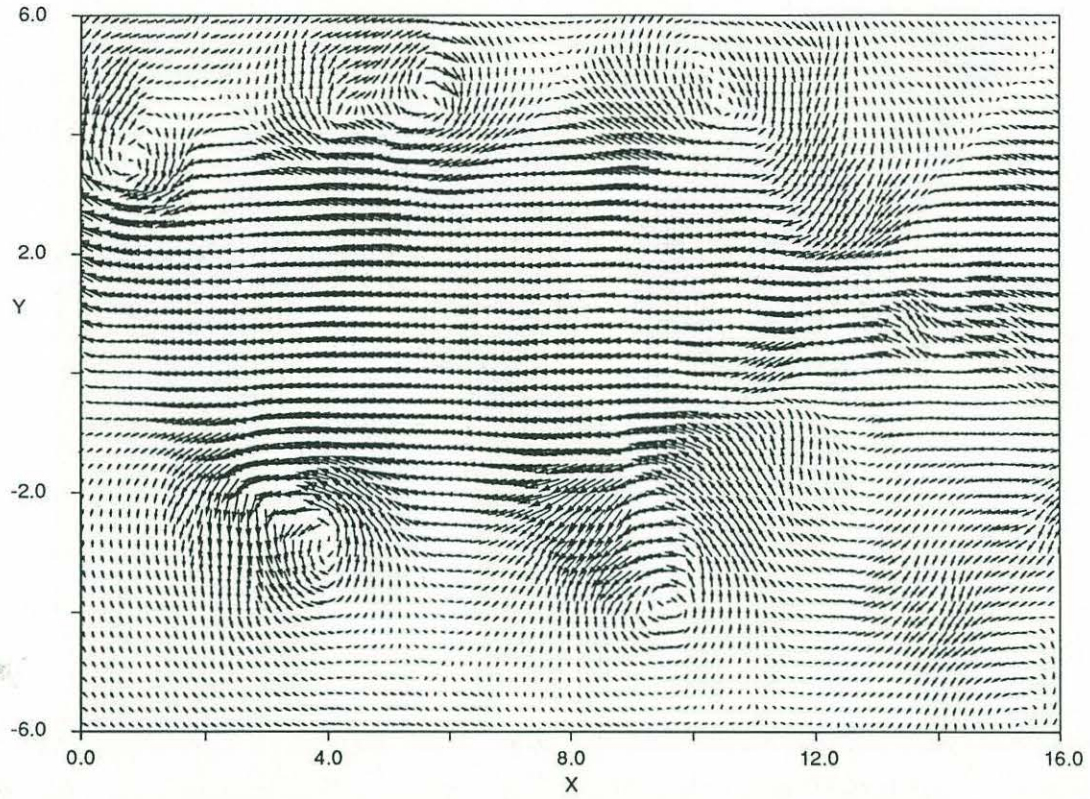

Figure 4-5: Experimentally obtained velocity field of incoming vortex street.

Table 4.5: Parameters for vortex interaction experiment.

Strength of oncoming vortices	2.0 cm^2/s
Diameter of oncoming vortices	2.0 cm
Width of Vortex street	7.0 cm
Profile	NACA0014
Forward speed, U_0	2.82 cm/s
Frequency, ω	1.82 s^{-1}
Chord length, $2c$	2.02 cm
Heave amplitude	1.59 cm
Pitch amplitude	0.785 rad
Pitch point	$c/3$ from leading edge

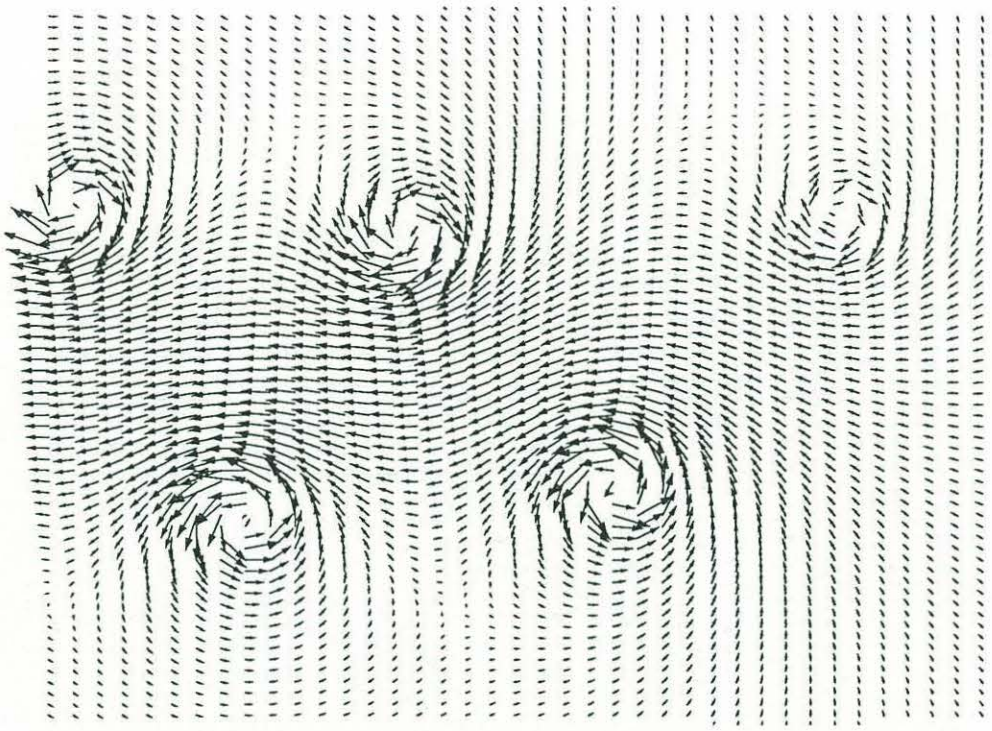

Figure 4-6: Incoming vortex street for numerical simulation.

parameters that are are listed in Table 4.5. From numerical simulation, the foil without an oncoming vortex street leaves the wake seen in Figure 4-7[2]. For this particular case we see that the foil wake consists of alternate sign vortices that lie almost on the line of the foil's mean position.

For the combined case of the oscillating foil inside the vortex street, the character of the downstream wake depends on the phase of the foil motion relative to the incoming vortex street. Let us discuss this input parameter in some more detail.

In Chapter 2, the parameter $\phi = \omega t_0$ was used to describe the relative phase between the motion of the foil and the vortex street. I simulations, it is difficult to specify t_0 a priori, so instead we let the phase of the motion, μ, run from $-\pi$ to π. By inspection during or after the simulation, t_0 can be found. The relevant parameter

[2]The vector plots in Figures 4-6 and 4-7, were created with a smooth vortex velocity kernel:

$$u - iv = \frac{i\gamma_k}{z - z_k}\left(1 - e^{\frac{|z-z_k|}{0.1}}\right)$$

This way we avoid arbitrary large velocities at field points near vortices, while preserving the resolution of interesting features. This only pertains to the displayed velocities, in the simulations we always use point vortices.

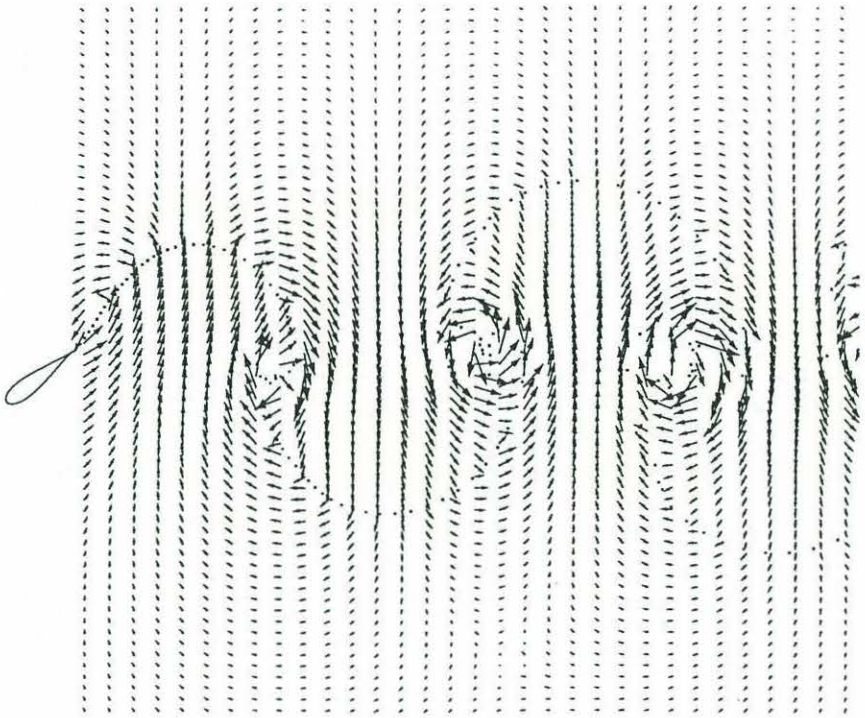

Figure 4-7: Wake velocity field for foil alone.

needed to present the results consistently, is a new definition of ϕ:

$$\phi = \mu + \omega t_0$$

Figure 4-8 shows the significance of the value of ϕ. $\phi = 0$ corresponds to a head on collision attempt by the foil, or what we can call interception–mode. At $\phi = \pm\pi$, the foil tries to avoid the vortices as much as possible, we call this the slalom–mode.

For the combination of input parameters in Table 4.5, two modes of vortex interaction were observed in the experiment, depending on the streamwise spacing between the cylinder and the foil. Changing the value of this spacing is equivalent to changing ϕ. It was observed that the π–mode caused the vortices in the incoming street to merge with same sign vorticity shed from the trailing edge of the foil, leaving a strong wake of alternate sign vortices. When the foil moved in th 0–mode, the opposite would happen, i.e. foil shed vorticity would to some extent neutralize the incoming vortex street. In figure 4-9 we see that the simulations confirm this behavior. These are snapshots of the foil and the vortices. Positive vortices are identified with a '+',

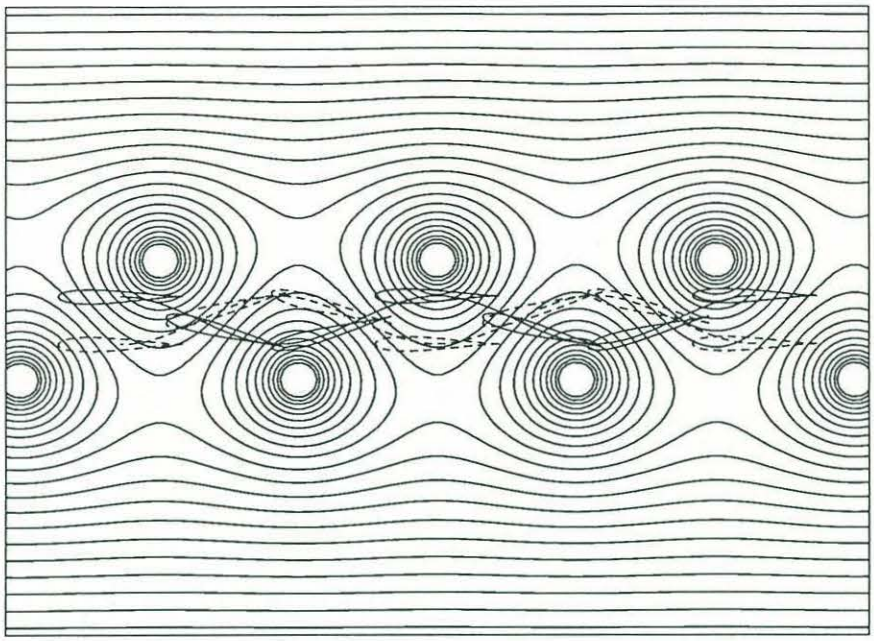

Figure 4-8: Foil path and streamlines as seen by an observer moving with the Kármán vortex street.Solid path: $\phi = 0$, dashed path: $\phi = \pm\pi$.

the negative the negative with circles. In the first case we see that the upstream vortices merges with the foil shed vorticity. In the second case, positive and negative vortex areas are close together, effectively cancelling each other.

The velocity field in the wake associated with these two modes of interaction is shown in Figure 4-10. In the merging mode, we see a strong wake velocity in the direction of foil propagation, whereas in the cancelling mode, the velocity is high only in very small regions, i.e. the wake signature has been reduced.

4.4 Simulation results

Several series of simulation runs have been performed, using the method in the previous chapter, so that the effect of different input parameters on foil performance could be assessed. Table 4.6 lists the input variables that were specified in the simulations. The foil geometry is given by a and ζ_c, which are the same in all the runs, resulting in a symmetric foil with half chord 1.0083 and 12% thickness. Heave and pitch amplitudes are h_0 and α_0 (radians), respectively, and the pitch point is b. The forces

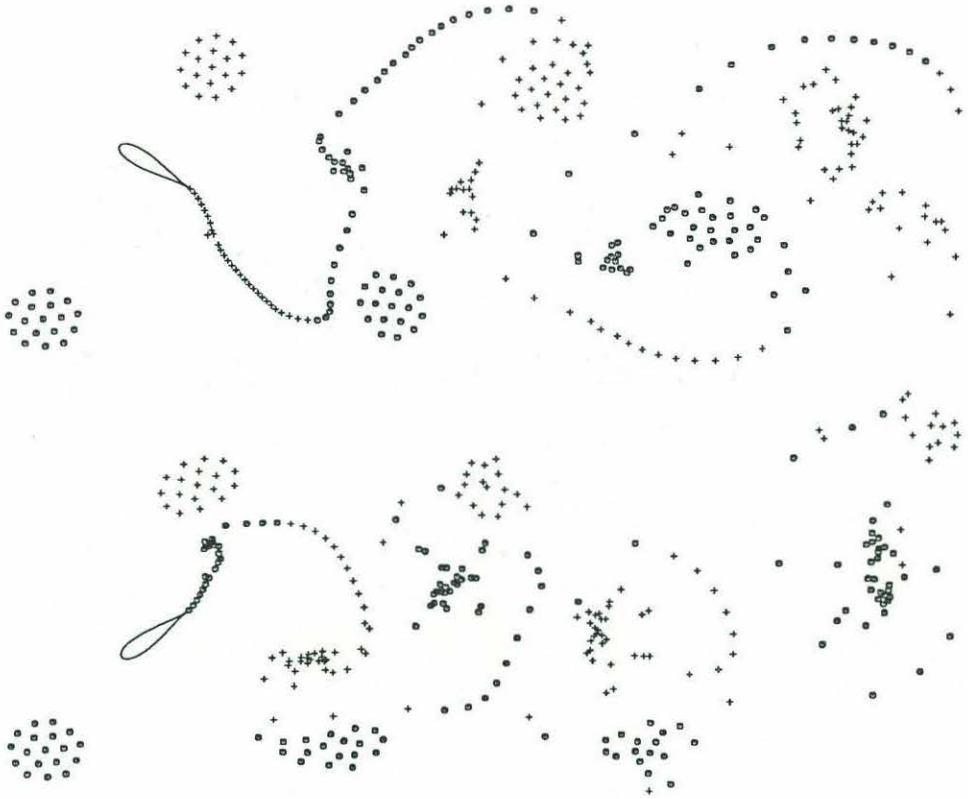

Figure 4-9: Vortex interaction.

Table 4.6: Input for simulations.

	a	ζ_c	h_0	b	α_0	U	κ	q	ω
Case 1	0.5	-0.05	0.4	0	0.2	1.0	0.1	2.0	$\pi/3$
Case 2	0.5	-0.05	0.4	0	0.2	1.0	0.2	2.0	$\pi/3$
Case 3	0.5	-0.05	0.4	0	0.2	1.0	0.2	3.6	$\pi/3$
Case 4	0.5	-0.05	0.9	0	0.3	1.0	0.2	3.6	$\pi/3$
Case 5	0.5	-0.05	0.9	0	0.3	1.0	0.2	1.8	$\pi/3$
Case 6	0.5	-0.05	0.4	0	0.2	1.0	0.4	3.0	$\pi/3$
Case 7	0.5	-0.05	0.4	-1	0.2	1.0	0.2	2.0	$\pi/3$
Case 8	0.5	-0.05	0.4	1	0.2	1.0	0.2	2.0	$\pi/3$

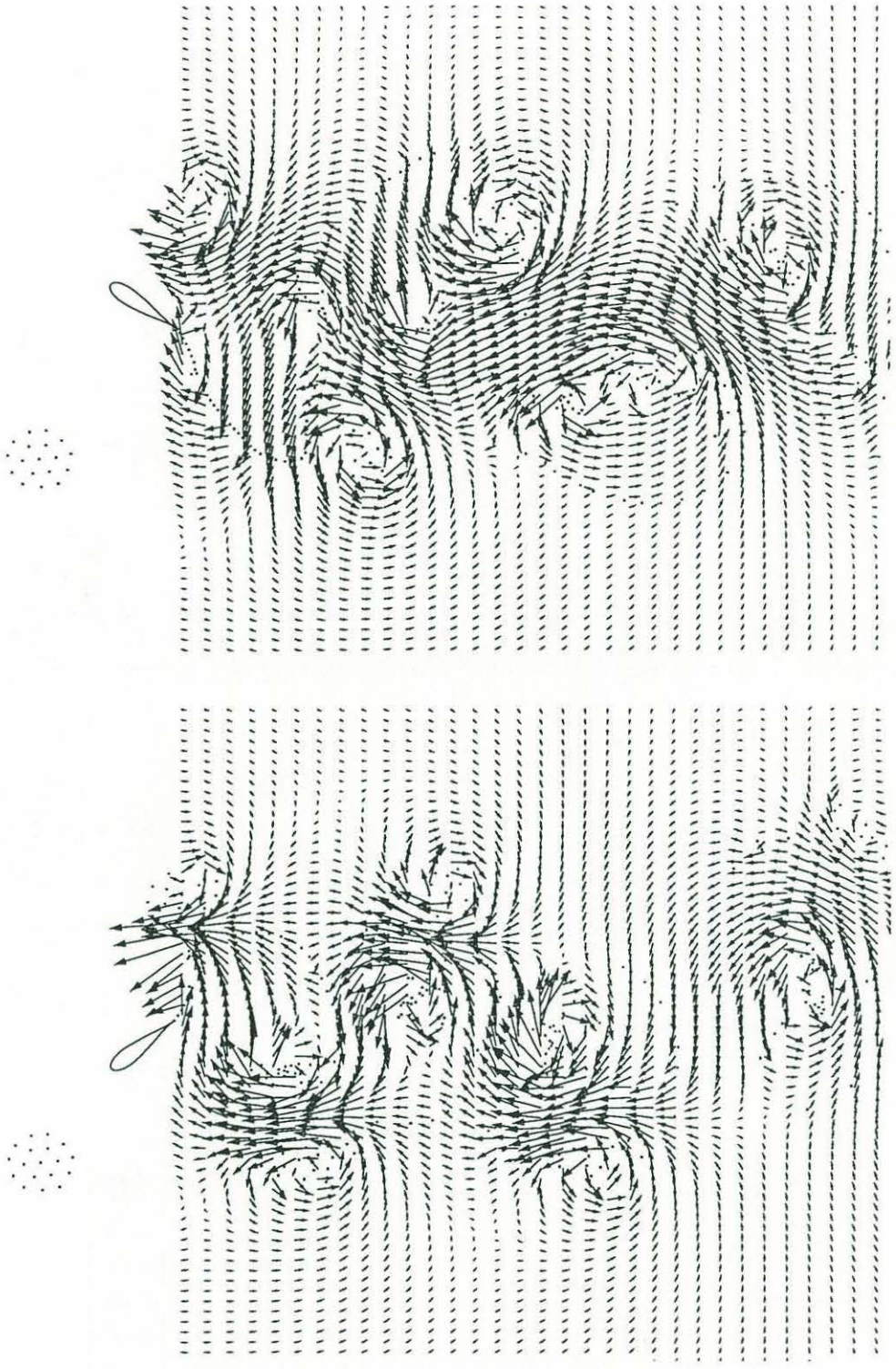

Figure 4-10: Combined wake velocity fields.

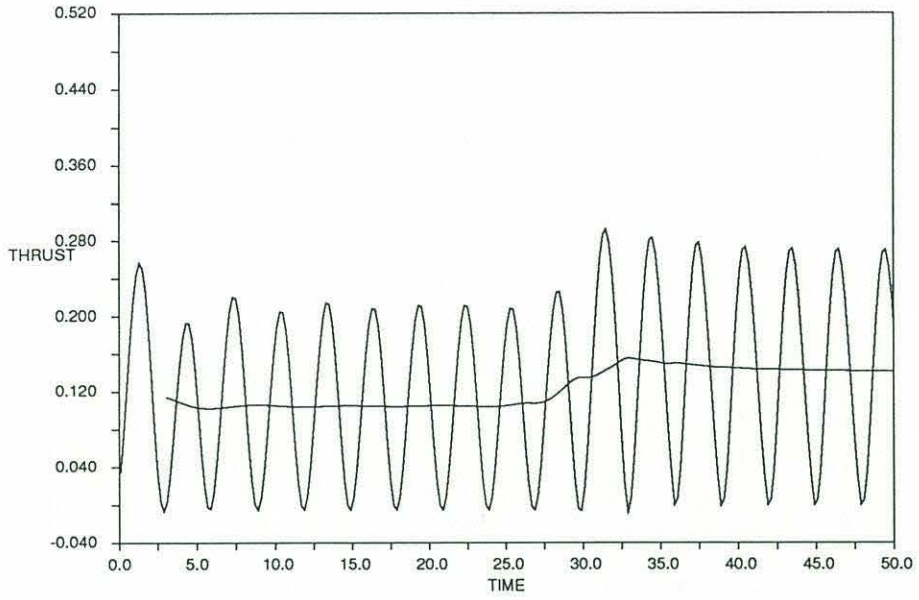

Figure 4-11: Instantaneous and averaged thrust for Case 1, $\phi = 0.1$.

are calculated according to the formulae in the previous chapter, thrust and input power are then averaged over a moving window, one period in length. That way it is easy to see when transient effects are negligible. An example can be seen in Figure 4-11, where both the instantaneous and average thrust is plotted for Case 1. This is a typical development; the force settles rather quickly at a freestream value, then the first vortices reach the foil, they are displaced from the incoming wake's eventual half width because of end effects. The foil interacts very closely with some of these and the forces go up as a result. After a couple of periods the foil is located in the regular part of the vortex street and the force evens out to its final value.

The results are presented the same way for all cases, we display how the final values of thrust, input power and efficiency depends on ϕ which runs from $-\pi$ to π, as defined in Figure 4-8. In particular we are looking for cases that show a strong dependence on ϕ, as this indicates a high potential for constructive foil–vortex interaction. Results from linear theory are also shown.

Free stream velocity is unity and the foil half chord is 1.0083, so thrust and power can be considered nondimensional coefficients.

In Case 1, the foil performs a moderate amplitude motion inside a wake that is

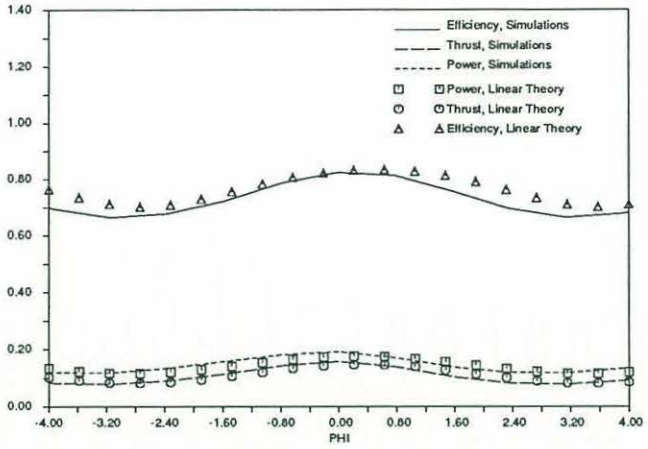

Figure 4-12: Hydrodynamic performance for Case 1.

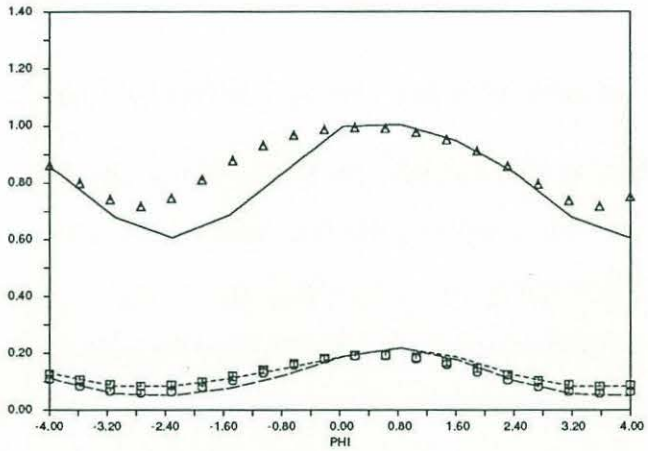

Figure 4-13: Hydrodynamic performance for Case 2. Legend in Figure 4-12.

rather weak. The heave amplitude is only 40% of the vortex street half width, so the foil stays inside the wake, but due to the finite size of the vortices and influence of their images inside the foil, the interaction closer than the input parameters suggest.. In Figure 4-12 we see that thrust, power, and efficiency all have maxima close $\phi = 0$, which isthe interception mode in Figure 4-8. In Case 1, the linear theory is in excellent agreement with the simulation.

In Case 2, the vortex street is stronger, and Figure 4-13 shows that the dependence on ϕ is stronger, which could be expected since the upwash from the vortex street accounts for a larger part of the forces.

Case 3 is one where the vortex street is wider, the upwash is weaker and the

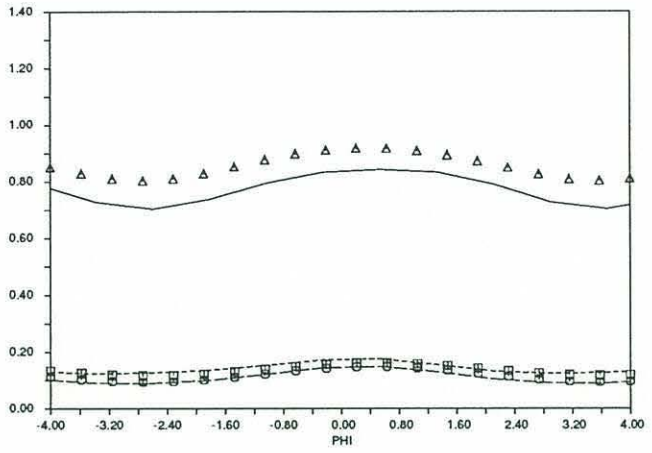

Figure 4-14: Hydrodynamic performance for Case 3. Legend in Figure 4-12.

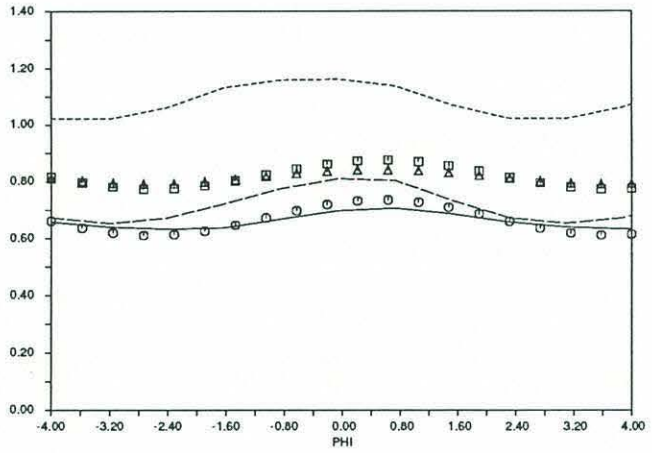

Figure 4-15: Hydrodynamic performance for Case 4. Legend in Figure 4-12.

performance depends less on ϕ since the inflow is more uniform.

In Case 4, we increase the amplitude of the motion, which has two potentially competing effects. On one hand, the motion accounts for more of the forces developed on the foil, which ought to reduce the dependency on ϕ. On the other hand, the increased amplitude brings the foil closer to the vortices, increasing the ϕ-dependency. Both power and thrust are much higher now, not surprisingly, and the ratio between them is such that the efficiency is uniformly high, exceeding unity. Also we see that the point of maximum efficiency is shifted in the negative ϕ direction, i.e. to a case where the foil reaches its maximum displacement before a vortex is encountered. In this case, we see that the linear theory no longer agrees very well with simulation.

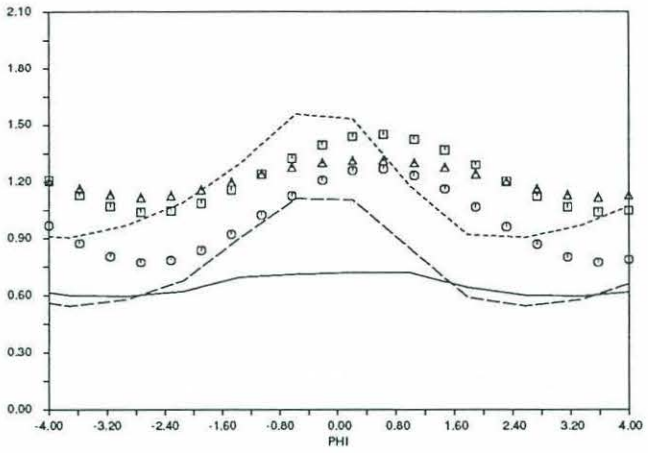

Figure 4-16: Hydrodynamic performance for Case 5. Legend in Figure 4-12.

This is probably due to the modeling of the inflow as a vertical gust independent of y, in the theory. When the foil oscillates with large amplitude, it moves into areas where this is a poor description of the flow.

Case 5 is the same as Case 4, except that the vortex street is of the same width as the heave double amplitude. This causes the foil to plunge right trough the vortices for certain ϕ, and around $\phi = 0$, the vortices are actually sucked to the inside of the foil because of their oppositely signed images in the foil. The resulting thrust and power are both very high, but the ratio between them, i.e. the efficiency, does not change much.

Case 6 has a wider and stronger vortex street, and the efficiency is strongly dependent on ϕ, exceeding unity for ϕ around $-\pi/2$. The theory is in very poor agreement for this case.

Cases 7 and 8 are like Case 2, except for the pitch pivot point which is at $b = -1$ and $b = 1$ respectively. This is equivalent to increasing the heave amplitude from 0.4 to 0.45 and changing the phase between heave and pitch by ∓ 0.46 radians, respectively. It appears that the pitch point should be located near the trailing edge for optimum performance. This conforms with the results for a foil in uniform inflow [44].

The trend seems to be quite uniform in all these numerical experiments; both thrust and input power reach their maxima at a phase angle close to 0, this is a

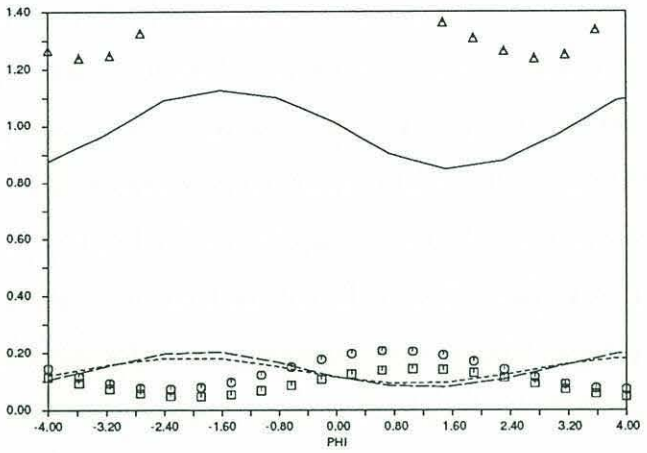

Figure 4-17: Hydrodynamic performance for Case 6. Legend in Figure 4-12.

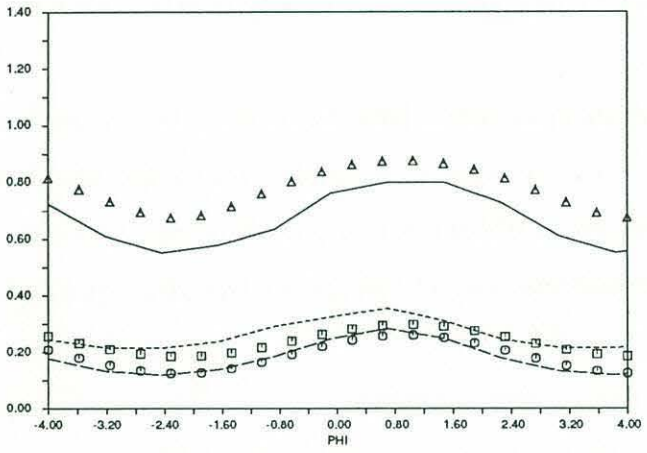

Figure 4-18: Hydrodynamic performance for Case 7. Legend in Figure 4-12.

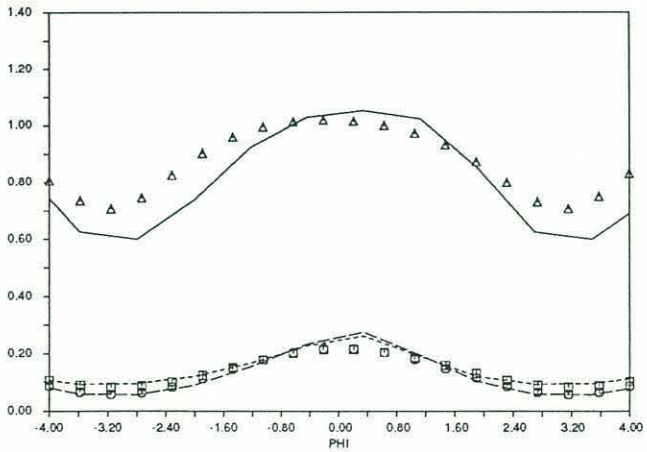

Figure 4-19: Hydrodynamic performance for Case 8. Legend in Figure 4-12.

highly loaded mode. The ratio between the two also reaches a maximum here, making this the most efficient mode as well. As we might expect, the dependency on ϕ is strongest when the vortex street is strong, and these cases are perhaps the most interesting for applications. All the important trends were verified by linear theory, although for quantitative predictions its application is limited to small amplitude motion and weak vortex streets. This is in contrast to the case of a flapping foil in uniform inflow, where linear theory works amazingly well for large amplitude motion.

The high efficiency mode is always associated with reduced wake signature of the kind seen in Figures 4-9 and 4-10, we shall have more to say about that in the next chapter. In fact, the reason for choosing ϕ as the principal input parameter of this investigation, was that we expected a wide variety of wake interaction behaviors over the span $-\pi \leq \phi < \pi$.

Certainly, many more runs would have to be done before we could claim to have a good overview of all the parameter dependencies in the problem. Perhaps most important would be the effect of the frequency ω. However, quick scans with the linear theory have not indicated that any of the results would be qualitatively different for other frequencies.

In Chapter 2, the energy recovery factor, η_R, was shown to be higher for a foil that is oscillating than one that is stationary. It has been difficult to repeat these results in simulations, because this case is so sensitive to the vortex street geometry, which is beyond direct control in the simulations. With more effort it should be possible to verify this result.

Chapter 5

The dynamics of shear layer – vortex interaction

5.1 Vortex mixing in the wake of an oscillating foil

In the previous chapter we have seen how propulsive efficiency of the foil depends on the phase, ϕ, between the foil's heave displacement and the oncoming vortices. Generally, the slalom–mode, $\phi = \pm\pi$, leads to low efficiency, whereas high efficiency is seen in the interception–mode, $\phi = 0$. These two extremes of the parameter ϕ are associated with distinctly different flows in the combined wake downstream of the foil. At low efficiency, the vortex street and the foil wake reinforce each other, leaving a trail of alternately signed vortices with a high content of kinetic energy. Conversely, in the case of high efficiency, the foil tries to cancel out incoming vortices by placing oppositely signed vorticity shed from its trailing edge close to them. Naturally, we are most interested in the cases that yield high efficiency, and to gain a better understanding of the wake dynamics for that mode, we shall consider the evolution of a flow that is a very simplified model of the foil wake and a typical oncoming vortex. The model problem is illustrated in Figure 5-1, where a vortex patch of radius R and vorticity amplitude ω_p is located a distance D from a shear layer of vorticity ampli-

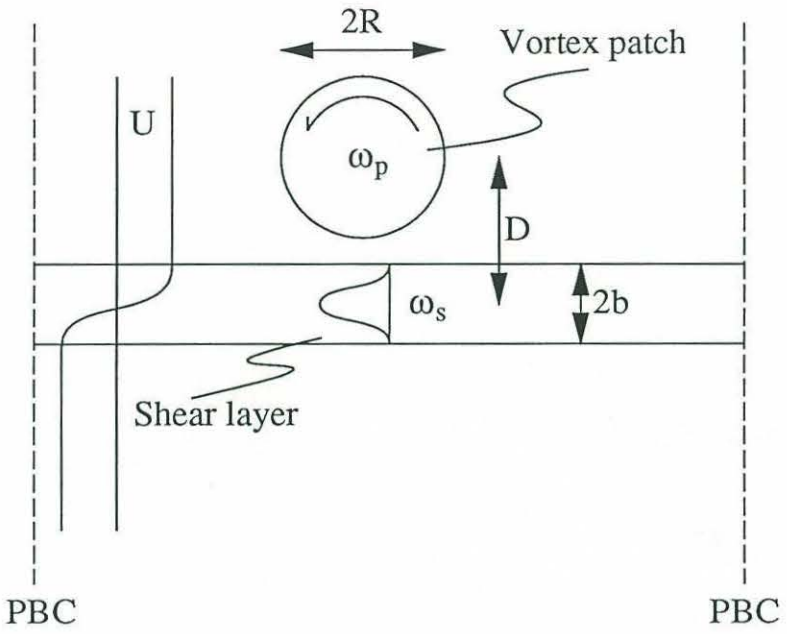

Figure 5-1: Initial configuration for model problem.

tude ω_s and half–thickness b. ω_p and ω_s are assumed to have opposite sign. There is no foil present, and the strength of the shear layer is constant along its length. If the shear layer had a finite length, its tendency to roll up at each end would dominate the evolution, so we specify periodic boundary conditions in the x-direction. The period is so much larger than the other length scales in the problem, that it does not influence the results. In this simplified model flow, we are no longer bound to use point vortices, and by switching to desingularized vortices as our computational elements, we can expect to resolve the fine scale features of the flow.

Two–dimensional vortex dynamics in free space has been subject to numerous studies as models for problems in engineering, physics and mathematics [60]. One problem of great practical importance is that of vortices generated by the wings of large aircraft, because they pose a hazard to other airplanes. This work is concerned with the rolling up of a finite length vortex sheet and the subsequent interaction process between vortices [12]. At the other end of the size spectrum, two–dimensional flow in liquid helium II is modeled with point vortices [57]. Point vortices are also a showcase of chaos, Aref [6] shows that chaotic behavior exists among point vortices when their number exceeds 3, in free space. Vortex dynamics also relates to the

development of turbulent flow. Observations of the turbulent mixing layer has shown the existence of quasi–two–dimensional coherent structures that are well described as finite size vortices. Important issues here are the merging of vortices into larger structures which can explain the growth of the shear layer, and the conditions under which vortices are torn apart by the strain induced by the other vortices. One result which has relevance to the present study is the fact that two like–signed vortices merge when their initial separation is less than 1.7 diameters [56, 19, 23]. Opposite sign vortices have been found to merge only at low Reynolds numbers [45], while in inviscid flow they do not mix and in fact there is a steady solution for large separation distances [60].

If the results obtained from this model is to have any bearing on our foil simulation results, the flow must be assumed inviscid, and one of the important questions that we would like to answer is whether the two regions of opposite sign vorticity can merge or mix in the absence of viscous diffusion. In our model, one of the participants in the vortex interaction is not a vortex patch, but a thin shear layer. When end effects are present, such a shear layer has a strong tendency to roll up under its own influence [13, 17, 49, 24, 7, 40, 41], and a lone shear layer of infinite length is subject to growing instabilities. Since the shear layer is a much more volatile entity than the vortex patch, we have reason to expect a wider variety of interaction modes, compared to the interaction between circular regions of vorticity.

The vortex method uses elements that have a finite core size, as opposed to the point vortex method in the previous chapters. It has been proven that the method converges as the input parameters are refined, which makes it suitable for investigating the qualitative behavior of the shear layer – vortex patch interaction. The vortex method gives the highest rate of convergence when the initial vorticity field is smooth, and the vorticity profiles chosen for this problem has 7 continuous derivatives, as shown in Table 5.1.

Table 5.1: Vorticity, ω, and velocity, u, for vortex patch and shear layer.

Vortex Patch	Shear Layer
$\omega = \begin{cases} \omega_p(1 - r^2/R^2)^7 & r \geq R \\ 0 & r > R \end{cases}$	$\omega = \begin{cases} \omega_s(1 - y^2/b^2)^7 & \lvert y\rvert \leq b \\ 0 & \lvert y\rvert > b \end{cases}$
$u_t = \frac{\omega_p R}{16} \begin{cases} 1 - (1 - \frac{r^2}{R^2})^8 & r \leq R \\ R/r & r > R \end{cases}$	$u = \omega_s b \begin{cases} \frac{y}{b} - \frac{7y^3}{3b^3} + \frac{21y^5}{5b^5} - \frac{5y^7}{b^7} + \frac{35y^9}{9b^9} - \frac{21y^{11}}{11b^{11}} + \frac{7y^{13}}{13b^{13}} - \frac{y^{15}}{15b^{15}} & \lvert y\rvert \leq b \\ \pm 2048/6435 & y \gtrless b \end{cases}$

5.2 Convergence of vortex methods

Rosenhead [59] was the first to use point vortices as computational elements to study the evolution of a 2–dimensional vorticity field (a zero–thickness shear layer with periodic boundary conditions). Finer discretizations in space and time quickly revealed that the method is not convergent; the apparent success of Rosenhead's calculations had been a fortuitous result of using a very small number of vortices (12) and a coarse time integration scheme. Point vortices are singular, they develop chaotic behavior and cannot represent the evolution of a vorticity field even when the initial problem is well posed [63]. The idea of representing a flow with a limited number of Lagrangian elements is very appealing in its simplicity however, and researchers have since developed methods that use non–singular vortices with a finite (or even infinite) size to overcome the difficulties [72, 18]. These methods have now been progressed to a state where convergence is proven for flows in free space and strong numerical evidence exists for convergence in the presence of bodies [43, 11, 54, 33, 69].

The vortex method solves the 2–dimensional Euler equations in the Lagrangian form. Following the notation of Hald [33], we express the trajectory of a fluid element

as a function of time and its initial position:

$$x = x(\alpha, t) \ , \ x(\alpha, 0) = \alpha$$

The particle position changes at a rate given by the local velocity:

$$\frac{d}{dt}x(\alpha, t) = u(x(\alpha, t), t) \tag{5.1}$$

where u depends on the vorticity field through Biot–Savart's law:

$$u(x(\alpha, t), t) = \int_{\mathbf{R}^2} K(x - x')\omega(x')dx'$$

K is the fundamental solution to $\nabla \times u = \omega$:

$$K(x) = \frac{[-x_2, x_1]^T}{2\pi r^2}$$

Vorticity is a material quantity, $\omega(x(\alpha, t), t) = \omega(\alpha, 0)$, and by virtue of incompressibility, we can change variable of integration:

$$u(x(\alpha, t), t) = \int_{\mathbf{R}^2} K(x - x(\alpha', t))\omega(\alpha', 0)d\alpha' \tag{5.2}$$

Equations (5.1) and (5.2) say that the flow can be thought of as an infinite number of vortex elements of constant strength that convect according to their mutual influence. This is the basis of the vortex method.

The method simulates the evolution of a given initial vortex field with a finite number of vortex elements. Their strengths and locations are initialized as shown in Figure 5-2. Each vortex is put at the points α_j of a uniform mesh of size h and assigned a circulation $\omega(\alpha_j, 0)h^2$. Equations (5.1) and (5.2) above are replaced by a finite order system:

$$\frac{d}{dt}\tilde{x}(\alpha_i, t) = \sum_j K_\delta(\tilde{x}(\alpha_i, t) - \tilde{x}(\alpha_j, t))\omega(\alpha_j, 0)h^2 \tag{5.3}$$

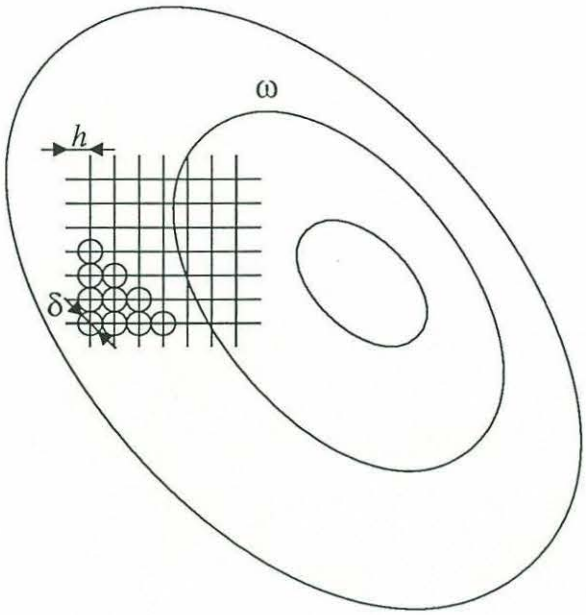

Figure 5-2: Initializing the vortex method.

which describes the trajectories of all the vortices. If the number of vortices in our discretization is N, it would appear that the calculation of all the convection velocities requires an order N^2 effort at each time step. In Appendix A it is described how this effort can be reduced to $O(N)$ by collecting the influence of remote vortices into multipole singularities. In particular, the adaptation of the multipole expansion method to periodic boundary conditions is described in detail.

The vorticity field is approximated by:

$$\tilde{\omega}(x,t) = \sum_j \zeta_\delta(x - \tilde{x}(\alpha_j, t))\omega(\alpha_j, 0)h^2 \tag{5.4}$$

K_δ is a smoothed approximation to K, corresponding to a smoothed vorticity element, ζ_δ. The cutoff radius δ, is a characteristic length scale for the size of the vortex elements. As $\delta \to 0$, $K_\delta \to K$, and $\zeta_\delta \to \delta(x,y)$, the Dirac delta function. The accuracy of the method depends on:

- Choice of cutoff function, ζ_δ.
- Smoothness of the initial vorticity field, $\omega(\alpha, 0)$.
- Choice of initializing mesh size, h.

- Choice of cutoff radius, δ.

On Hald's [33] recommendation, we choose Nordmark's 8^{th} order cutoff:

$$\zeta_\delta = \begin{cases} \frac{52}{\pi\delta^2}\left(1 - 21\frac{r^2}{\delta^2} + 105\frac{r^4}{\delta^4} - 140\frac{r^6}{\delta^6}\right)\left(1 - \frac{r^2}{\delta^2}\right)^9 & \text{for } r \leq \delta \\ 0 & \text{for } r > \delta \end{cases} \tag{5.5}$$

With complex notation $u - iv$ for the velocity, the corresponding smoothed kernel is given by:

$$K_\delta = \begin{cases} \frac{-1}{2\pi z}\left[1 + \left[286 - 1092\left(1 - \frac{r^2}{\delta^2}\right) + 1365\left(1 - \frac{r^2}{\delta^2}\right)^2 - 560\left(1 - \frac{r^2}{\delta^2}\right)^3\right]\left(1 - \frac{r^2}{\delta^2}\right)^2\right] & \text{for } r \leq \delta \\ -1/(2\pi z) & \text{for } r > \delta \end{cases}$$

The initial field is such that a convergence rate of 4 can be expected [52] as the initial discretization is refined according to:

$$\frac{\delta}{L} = 1.7\sqrt{\frac{h}{L}}$$

i.e. the vortex core size should decrease at a slower rate than the mesh size, resulting in a larger degree of overlap. Here, L is a characteristic length scale, we take it to be R in our model problem. There is one additional concern when using the multipole expansion method described in the Appendix A: The cutoff radius must be small compared to the smallest boxes of the computational domain for the multipole expansions to be accurate. Fortunately the errors introduced seemed insignificant, and the results of the simulations were also insensitive to the choice of δ, so an acceptable compromise could be found.

5.3 Simulation results

In order to track the evolution of the vorticity field, we would like to have some integrated quantity, or functional of the vorticity field, that indicates the degree of interaction. Since our model flow is inviscid and incompressible, has periodic boundary conditions, and is absent of bodies or other external forces and potentials,

there is no mechanism to change the kinetic energy over time. The mixing processes that we expect to see must be energy preserving, to de–energize the vortex street requires that work is done on the foil. Thus, we can not track kinetic energy as a function of time as a measure of vortex interaction. Other physically interesting quantities like momentum and enstrophy are also conserved.

Instead, it was found that the polar moment of vorticity in the vortex patch alone was a good indicator of the vorticity field evolution:

$$I_p = \iint_{A_p} \omega(x,y) \left[(x - x_p)^2 + (y - y_p)^2 \right] dxdy$$

where A_p is defined as the area with positive vorticity and (x_p, y_p) is the centroid. In the simulations, I_p is found from simple summations over all the positive vortices. When there is a high degree of interaction, the vortex patch deforms a lot and I_p increases with time.

In this problem there are 3 non–dimensional quantities to consider: R/b, D/b and Γ_p/Γ_s. Here, Γ_p is the circulation around the patch and Γ_s is the circulation around a piece of length $2R$ of the shear layer.

$$\Gamma_p = \frac{\pi}{8} \omega_p R^2$$
$$\Gamma_s = \frac{8192}{6435} \omega_s R b$$

The ratio between these two circulations values indicate the strength of the vortex patch compared to that of the shear layer. For all simulations. $\omega_s = -1.0$ and $b = 0.05$ were held constant, and the other parameters varied to give different nondimensional variables.

Figures 5-3 – 5-5 show how the evolution of I_p depends on the input parameters. In Figure 5-3, R/b and Γ_p/Γ_s are held constant, while D/b varies. The result is not surprising; we see that the interaction is stronger when the vortex patch is close to the shear layer. Of course, in the interaction between the foil and oncoming vortices, the distance b cannot be made zero.

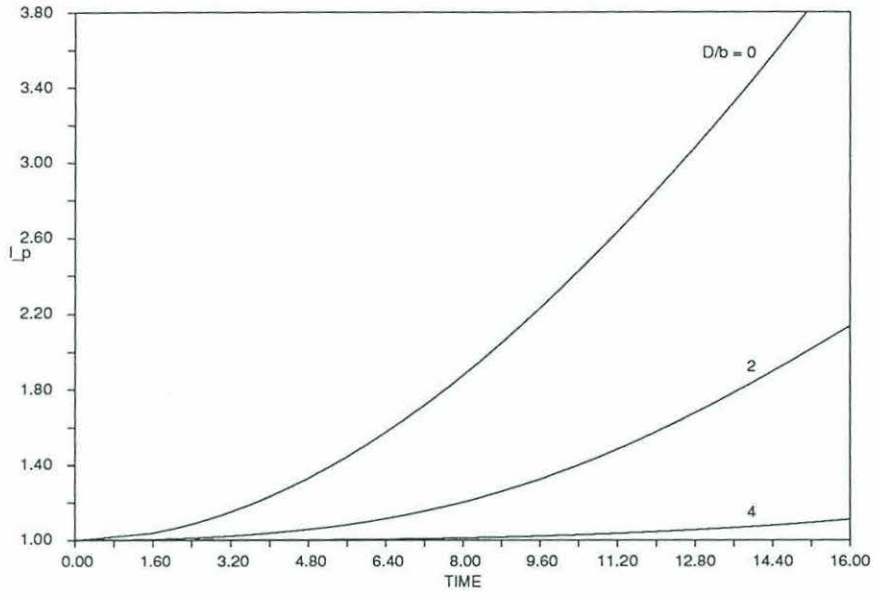

Figure 5-3: $I_p(t)$ for $R/b = 4$ and $\Gamma_p/\Gamma_s = 1$.

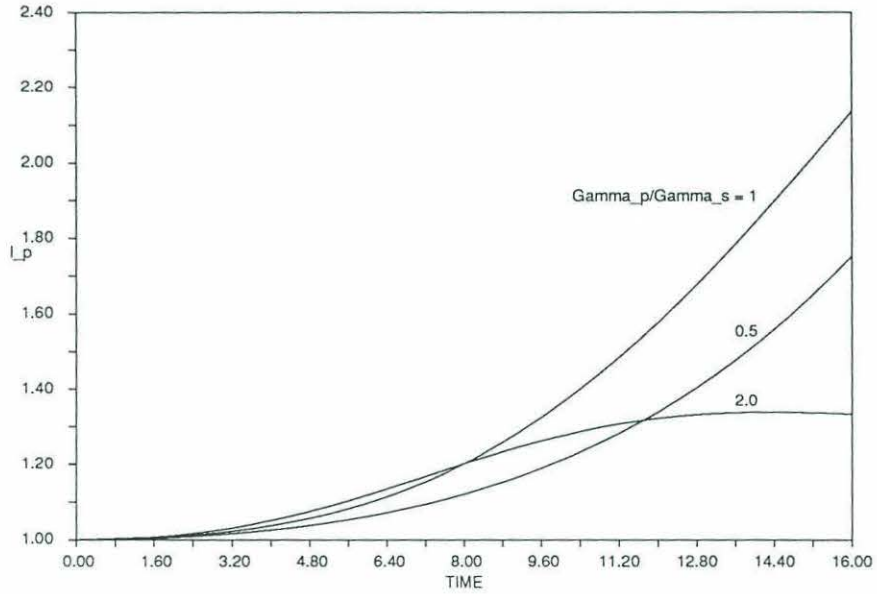

Figure 5-4: $I_p(t)$ for $R/b = 4$ and $D/b = 2$.

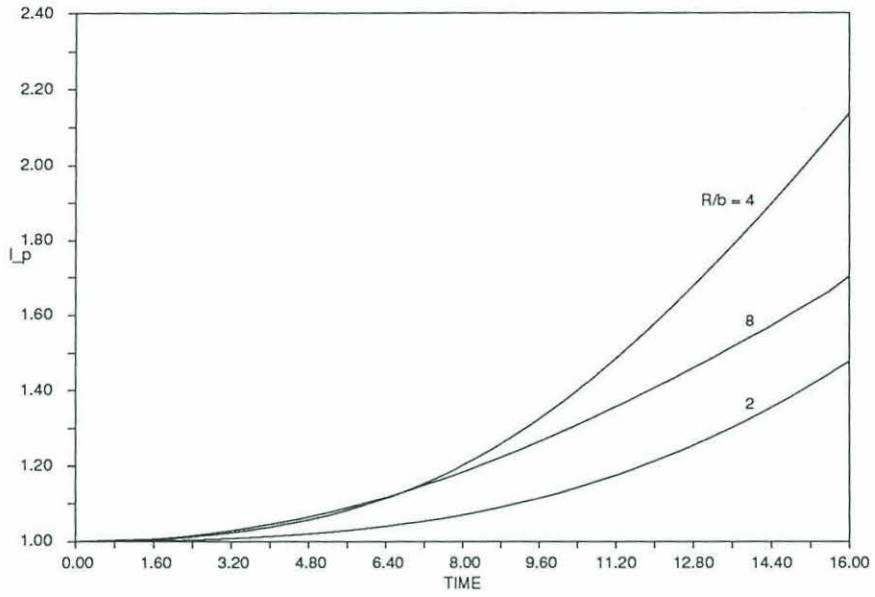

Figure 5-5: $I_p(t)$ for $D/b = 2$ and $\Gamma_p/\Gamma_s = 1$.

Next, we consider variations in Γ_p/Γ_s, Figure 5-4. We see that the vortex patch undergoes a maximum amount of straining for $\Gamma_p/\Gamma_s = 1$. When Γ_p is too small, the shear layer does not roll up very fast and when Γ_p is too large, it dominates the dynamics by sweeping the shear layer around itself without deforming very much. Thus, there is a range of intermediate Γ_p/Γ_s that gives the greatest interaction.

Finally, Figure 5-5 shows the dependence on R/b. I appears that there is an optimum value for R/b that maximizes the straining of the vortex patch. Intuitively, one would think that a larger R would lead to a larger growth in I_p, simply because the vortex overlap the shear layer more. The reason that this is not the case, could be that the periodic boundary conditions come into play when R is very large, reducing the strain of the vortex.

These simulation were all run with a rather low number of vortices (around 350 per wavelength for $h = 0.02$), and runs with more resolution were performed to verify their observed trends. The input parameters as well as a description on the evolution in each case are listed in Table 5.2.

Figures 5-6–5-9 shows some representative cases for times: $t = 0, t = 15, t = 30$. In these examples a mesh size $h = 0.01$ was used, resulting in some 1200 – 2000 vortices per wavelength. The same behaviors resulted when a finer mesh of $h = 0.005$ was

Table 5.2: Simulation runs.

Case	ω_p/ω_s	R/b	D/b	Γ_p/Γ_s	Flow description
1	-0.5	8	4	-1.23	Patch sweeps the shear layer around
2	-0.8	4	2	-0.99	Shear layer rolls up, the two move straight
3	-0.5	6	4	-0.93	Shear layer rolls up, the two move straight
4	-0.5	4	6	-0.62	Patch convects with little interaction
5	-0.1	4	4	-0.12	Patch convects with little interaction
6	-0.5	2	4	-0.31	Patch convects with little interaction
7	-0.3	4	4	-0.37	Some tendency to mix
8	-0.25	3	1.4	-0.23	Vortex patch gets squeezed and escapes
9	-0.5	4	2	-0.62	Patch gets rolled into shear layer

specified. Note that vortex elements with circulation magnitude less that $|\pi\omega_s h^2/50|$ have been removed from the figures for clarity. The clockwise vortices are marked with a circle, and the counterclockwise "+".

Figure 5-6 shows what happens when Γ_p similar to Γ_s and the patch is not too far away. The shear layer quickly rolls up and forms a cluster of comparable circulation to the patch. Then the two convect in a nearly straight path as would be expected from two nearly identical vortices.

When D is large, we observe the behavior in Figure 5-7, where the vortex patch convects with the flow and induces a slow disturbance in the shear layer. Note that the observer is moving with the patch in this sequence, so the convection is not apparent.

Next, a very weak vortex patch is put very close to the shear layer, Figure 5-8. The shear layer rolls up quickly, but the patch "escapes" and stays separate.

Finally, Figure 5-9 indicates that significant mixing can take place under the right conditions. Here. Γ_p/Γ_s = -0.62, and the patch is rather close to the shear layer. The two roll up into a kind of jelly roll pattern.

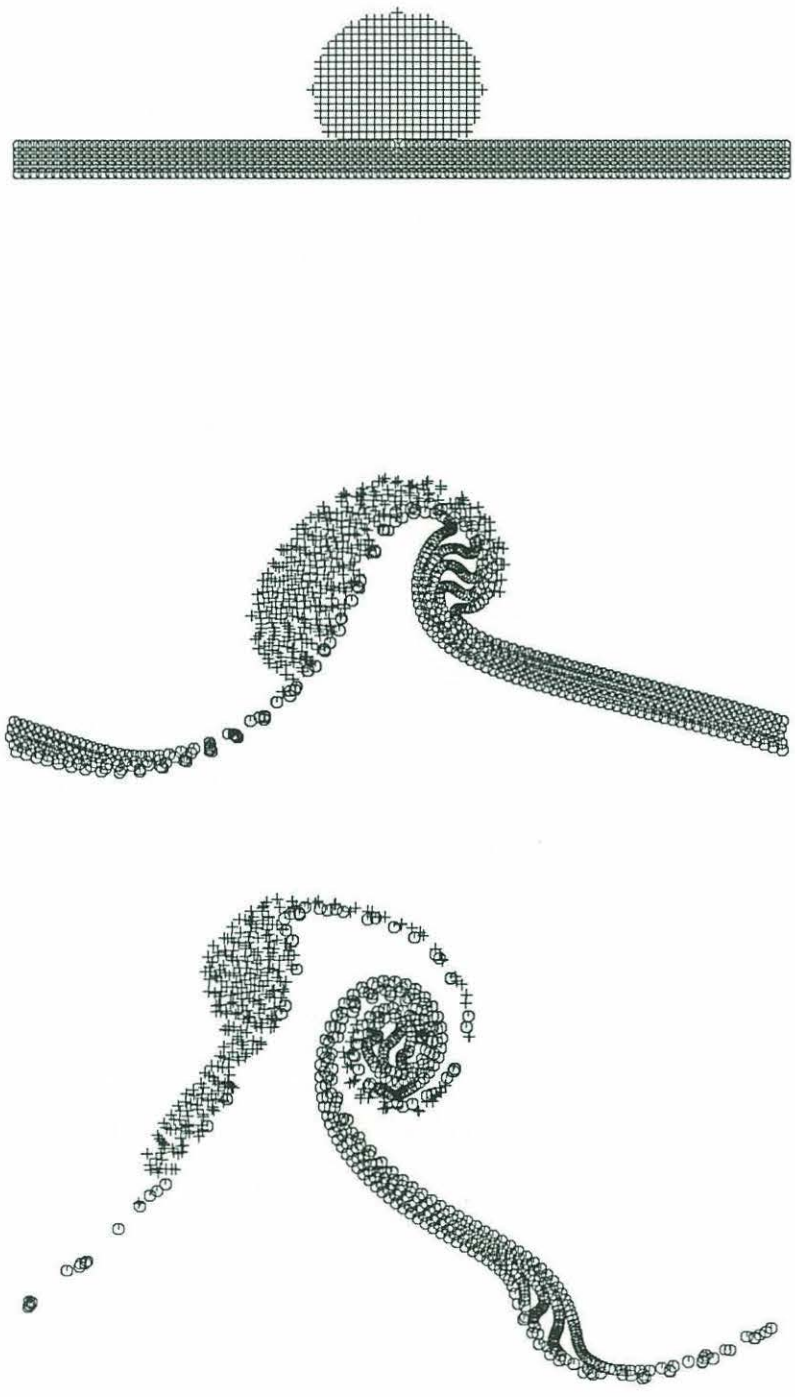

Figure 5-6: Case 2

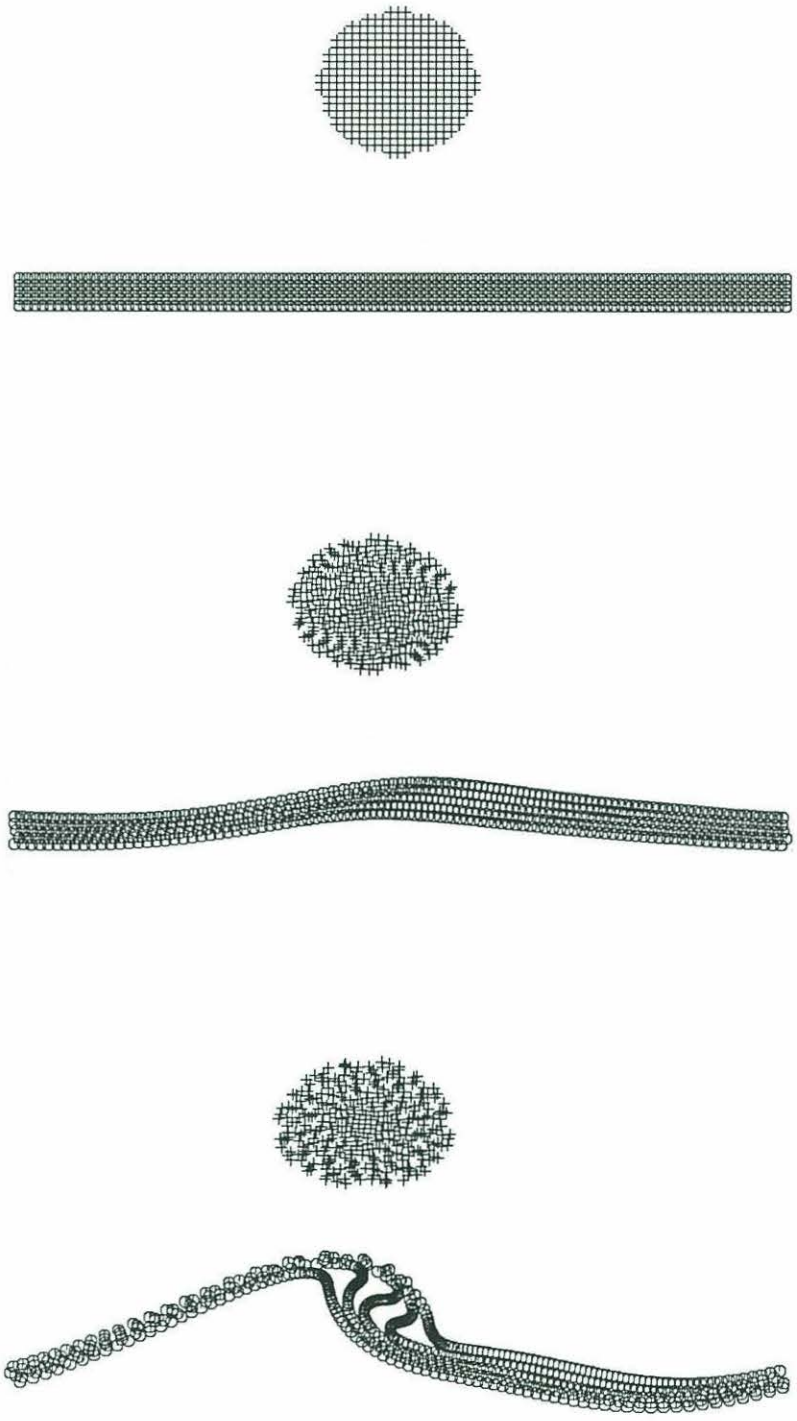

Figure 5-7: Case 4

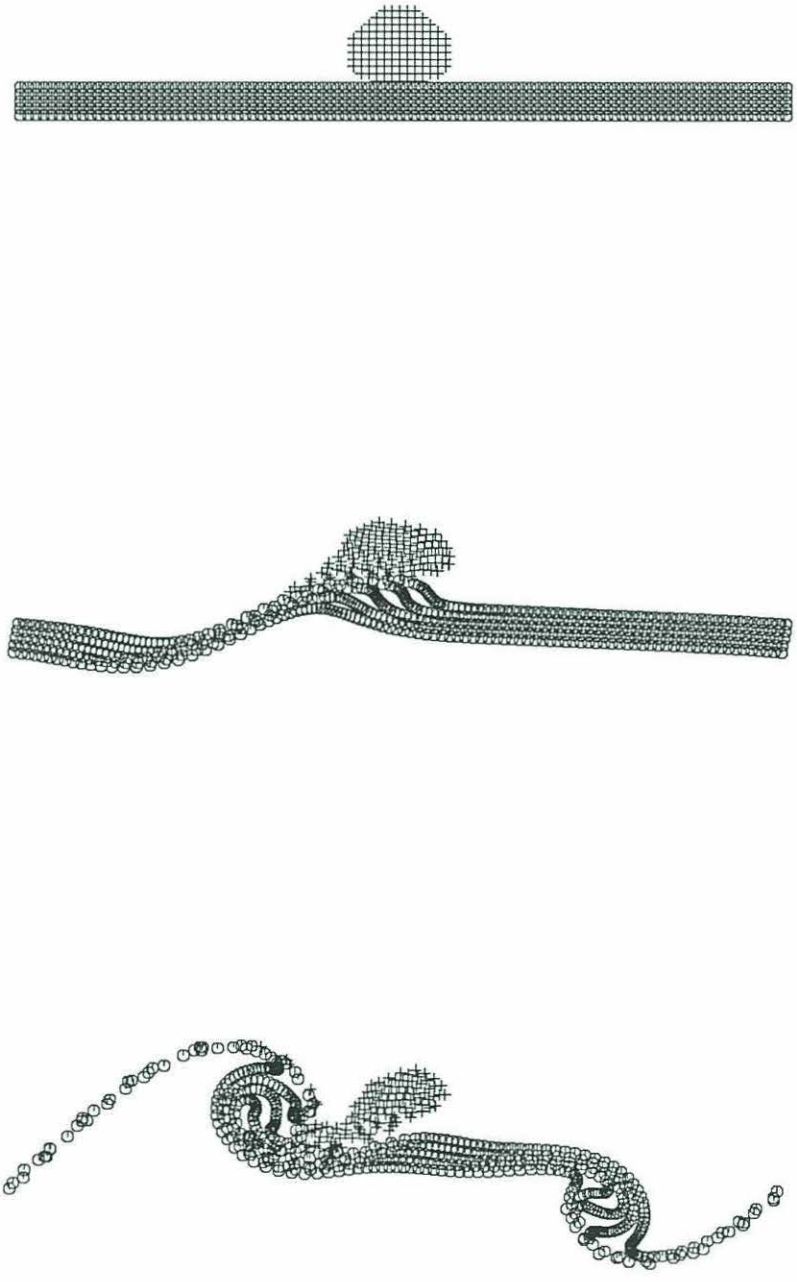

Figure 5-8: Case 8

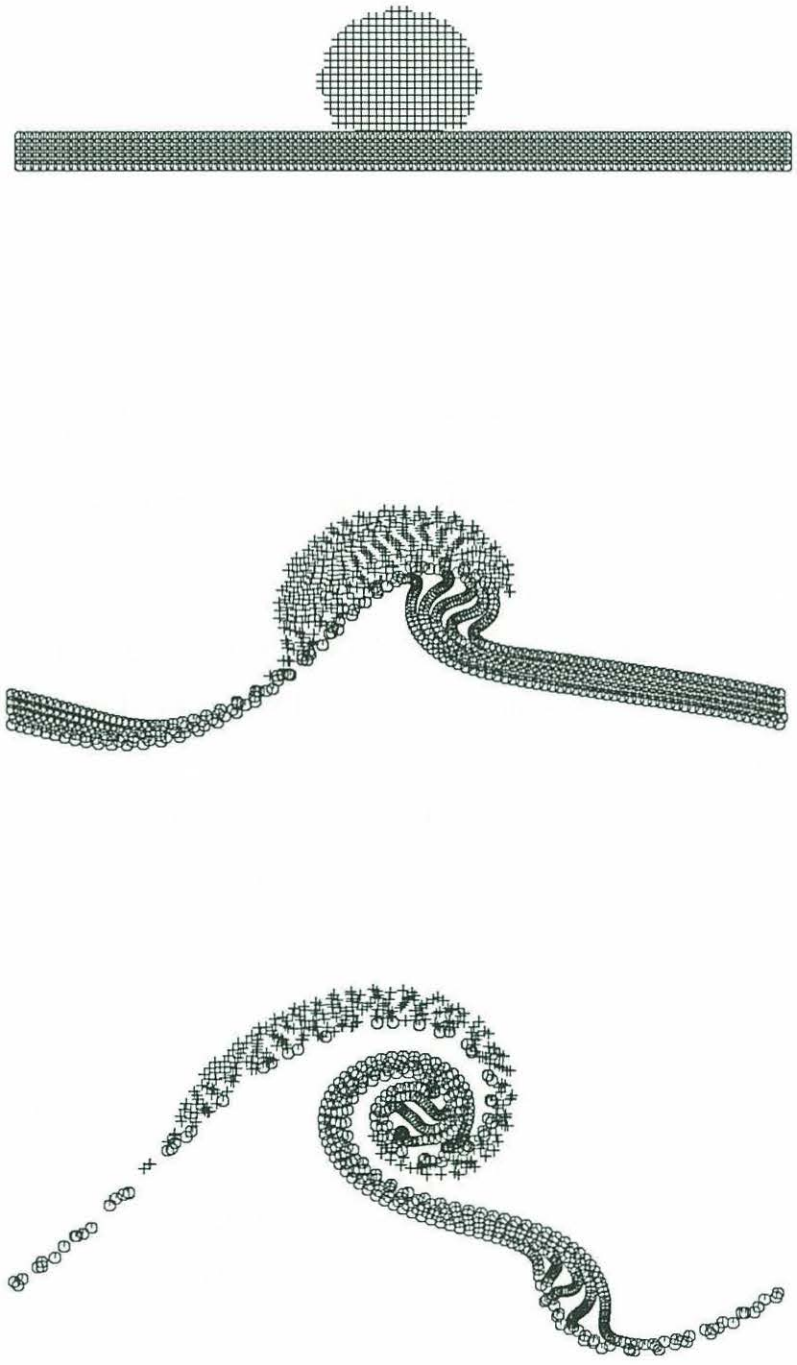

Figure 5-9: Case 9

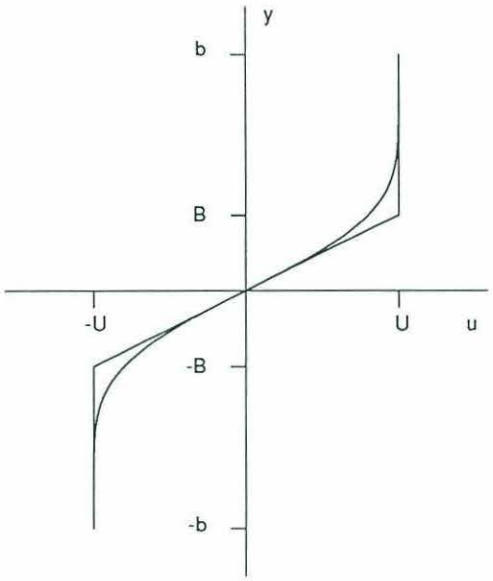

Figure 5-10: Exact and approximate velocity profiles for the shear layer.

5.4 The significance of shear layer instability

It has been known for over a century that an infinite shear layer is susceptible to instability, in the form of a standing wave of growing amplitude, and therefore can not be sustained. This phenomenon relates to the present study in at least two different ways. First, we would like to know the role of shear layer instability in Case 4, where the vortex patch is at a large distance. The question is: does the vortex patch act only to trigger the instability and is its influence is relatively unimportant at later stages? Second, all real flows have in them disturbances of different wavelengths, and we would like to show that these do not significantly change the results in the previous section.

Hydrodynamic instability is not overly sensitive to the particular shape of the velocity profile, and we can approximate the shear layer by one that has a piecewise linear profile, Figure 5-10. The linear profile is specified such that it has the exact derivative at $y = 0$ (i.e. the exact vorticity amplitude). This leads to:

$$\begin{aligned} B &= \frac{2048}{6435} b \\ U &= \frac{2048}{6435} \omega_s b \end{aligned}$$

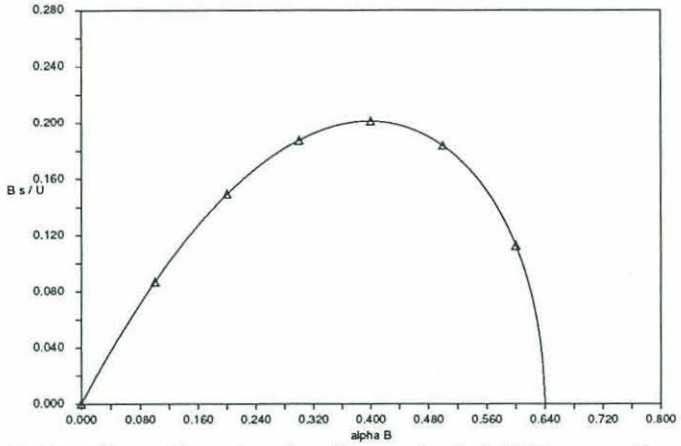

Figure 5-11: Growth rates for linear instabilities on the shear layer.

The linear stability analysis [22] for this case assumes a small disturbance in the form of a standing wave of wave number α. Lord Rayleigh [55] found that such a disturbance would grow at at rate e^{st}, with s given by:

$$\frac{B}{U}s = \frac{1}{2}\sqrt{e^{-4B\alpha} - (1 - 2B\alpha)^2} \tag{5.6}$$

shown in Figure 5-11. Since we impose periodic boundary conditions in this problem, we can only have disturbances with wavelengths of which the period is an integer multiple. The corresponding wave numbers are marked with triangles in Figure 5-11, for unit period and $b = 0.05$, which is what we use in all the simulations. $B/U = 1/\omega_s$, which is also set equal to unity in the simulations. The expected maximum growth rate is therefore $s = 0.20$, for waves of length $1/4$, whereas waves with length 1 will grow at a rate $s = 0.08$. These values correspond to a tenfold magnification of disturbances over times 11 and 29 respectively.

Figure 5-12, shows the significance of the instability of the shear layer in Case 4. What we have plotted is the maximum deflection of the center row of vortices in the simulation, as a function of time. This is the upper curve. The middle curve shows the deflection that is observed when the patch is removed at time 2, and the shear layer subsequently deforms solely due to its self-influence. This is compared

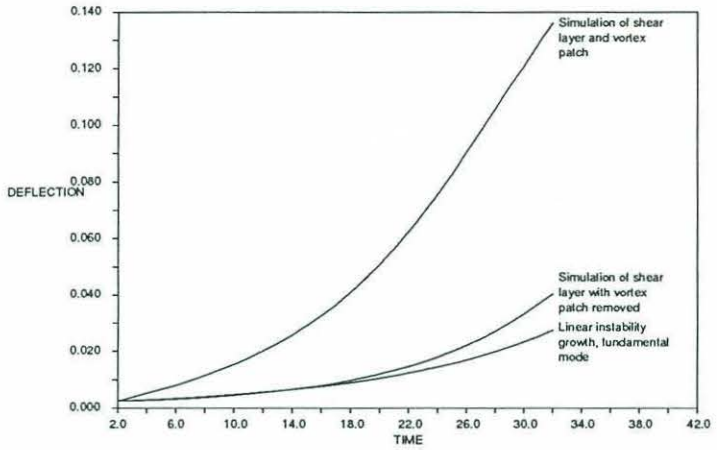

Figure 5-12: Deflection of the shear layer for Case 4.

with the growth that is predicted linear theory for the longest mode. We see that the deflection grows at a significantly higher rate when the vortex patch is present, which indicates that its influence is important throughout the simulation. Also, we note that the disturbance of the shear layer alone grows faster that the fundamental mode linear instability, indicating the presence of higher disturbance modes.

Figure 5-13 shows the configuration in Case 9 at time 30 when a maximum growth rate disturbance has been introduced to the problem. This was done by multiplying the initial vorticity in the shear layer by:

$$1 + \epsilon \cos(8\pi x)$$

Figure 5-13a and b corresponds to $\epsilon = 0.1$ and $\epsilon = -0.1$, respectively. We see remnants of the 10% disturbance in the shape of the rolled up shear layer, but the vortex interaction is not affected significantly. This is verified in Figure 5-14, where the evolution of I_p for the two disturbed cases is compared with the undisturbed case.

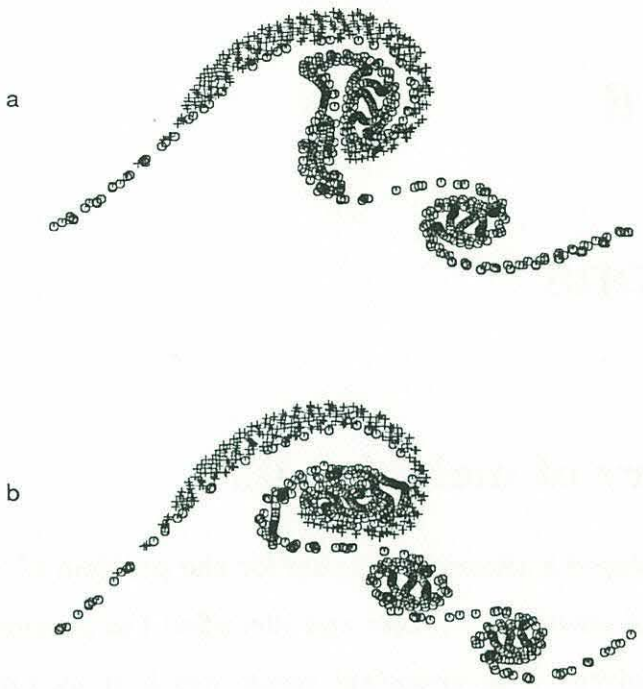

Figure 5-13: Case 9 with disturbances added to the shear layer.

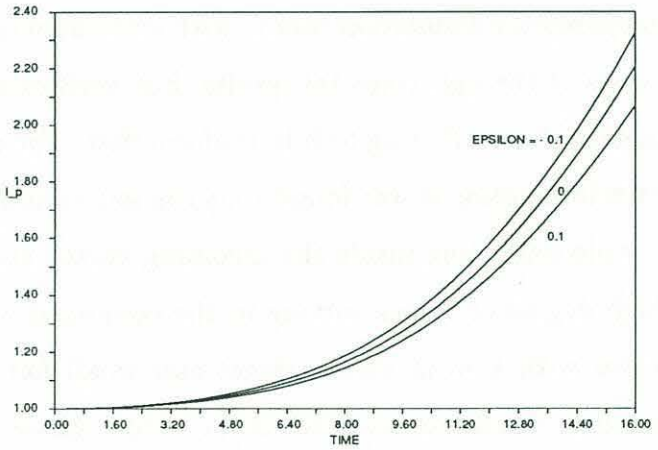

Figure 5-14: Evolution of vortex patch polar moment when the shear layer is disturbed.

Chapter 6

Conclusions

6.1 Summary of main results

In Chapter 2 we developed a theoretical model for the problem of a foil interacting with a double array of oncoming vortices and identified the parameters and nondimensional groups involved. The important result was that an oscillating foil can recover more of the energy in the wake than a stationary foil.

Chapter 3 contains the theory for the numerical simulations. The new contributions are a careful formulation of the velocity potential and derivation of closed form expressions for the force and the moment.

In Chapter 4 we compared the simulation results with experiments, which revealed some problems with some of the experimental results, but verified that a very high efficiency may be obtainable for oscillating foils in uniform flow. For optimum performance during foil–vortex interaction it was found that the foil should try to intercept the vortices head on, while remaining inside the incoming vortex street. This mode is associated with a high degree of vortex mixing in the combined wake. The linear theory is limited to cases with a weak vortex street and small foil motions, but it confirms the trends found in simulation even when the actual values are in error.

Chapter 5 dealt with this interaction in more detail. It was shown that in a narrow range of input parameters, when a vortex is close to a shear layer and the two have approximately equal (but opposite in sign) circulation, they can mix together,

effectively cancelling each other. We verified that moderate disturbance present in the flow would not change this result.

The Appendix contains two extensions to the $O(N)$ multipole expansion method. First it is shown how to deal effectively with the image vortices inside the mapped circle in foil simulations. Second, we adapt the method to periodic boundary conditions.

6.2 Recommendations for future work

The most interesting directions to take this research would be to include the effects of viscosity and 3 dimensions. Most likely, leading edge separation occurs in many of the interaction cases, and the vortex method is well suited to such calculations [71]. The method requires vortices to be generated on the entire foil surface at every time step, and the $O(N)$ method would be particularly useful in dealing with the very large number of vortices that would result.

Three–dimensional effects are sure to be important in applications, and a three–dimensional numerical model would give valuable insight into the vortex dynamics involved. One problem that I would expect is the formulation of the inflow, except for modeling of actual vortex shedding body upstream.

Appendix A

The fast vortex method

A.1 Introduction

There are many problems besides those of fluid mechanics that can be formulated as N-body interactions; galaxy interactions in celestial mechanics, particle interactions in plasma physics and molecular dynamics are well known examples. Researchers in these areas quickly found that the order N^2 effort required for direct calculation of all the pairwise interactions rendered many simulations of interest out of reach, even with the most powerful computers. This led to a search for methods with a reduced operational count. The earlier algorithms were based on fitting a uniform mesh over the computation domain, and distributing the source term onto this grid [35]. In the case of two–dimensional vortex simulations, the source term would be vorticity, ω, say. The Poisson equation relates the stream function Ψ to ω:

$$\nabla\Psi = -\omega$$

A fast method for solving Poisson's equation on the grid provides the advantage over direct computation. Then the velocity of each particle must be found from numerical derivatives of the stream function. Roberts and Christiansen [56] showed how a very large number of vortices could be tracked using this Particle In Cell method.

In simulating the evolution of point singularities, PIC leads to inherent smoothing

of the vortex distribution, and the effort required depends on the mesh size of the grid as well as the number of singularities. The mesh size must be chosen depending on N, so that in practice, the operation count becomes $O(N \log N)$. Proper boundary conditions must also be constructed. The smoothing problem was resolved by Anderson [2] in the Method of Local Corrections. In MLC, the close interactions are computed exactly. Recent applications of the Particle in Cell method to vortex simulations can be found in Yeung [82] and Scolan [66]. Clearly, in cases where the distribution of particles is highly non–uniform, there will be a lot of mesh points in regions where not much is happening, causing inefficient use of resources.

Appel, in [4], describes a fast method that is not dependent on a mesh, and shows applications to three–dimensional galaxy interactions. The individual computational elements, which may be galaxies or clusters of galaxies, are considered to be the leaves of a binary three. By maintaining the tree structure such that close and distant elements can be distinguished, the interactions that are not close can be performed with a single monopole expansion of the gravitational field from many elements. Appel estimated the computational effort to go asymptotically like $N \log N$ as N becomes large, and by careful optimization of the program was able to simulate the evolution of 10^5 elements over 500 time steps in 20 hours on a VAX11/780 computer. Appel also reports that his program had the ability to handle rapidly developing close interactions with a small time step, without imposing that time step on all the interactions.

A method that was better suited to error analysis and had simpler book–keeping, was presented by Barnes and Hut in [8]. Three–dimensional space is subdivided into cubes until a level is reached where each cube has only one particle or is empty, in which case it is discarded from the computation. Each cube has 1/8 the volume of its parent, and contributes mass and moment of mass to a "pseudo particle" at the level above it. This is done at all levels. The tree building process is relatively inexpensive and can be performed at every time step. When the force on particle k is to be computed, the pseudo particle interaction is used for cubes that are separated from k by a distance on the order of their own size. It was shown that this leads to an

$O(N \log N)$ effort. Error bounds can be found, based on worst case scenarios, where the particles are in opposite corners of their respective cells. Normally the error is much smaller, because the particles are not on average that badly placed, even when their distribution is highly non–uniform.

Greengard, Rokhlin, and Carrier [31, 15] presented a method for two–dimensional computations, based on multipole expansions of harmonic potentials that could be either Coloumbic or gravitational in nature. The algorithm builds a tree structure of boxes like that of Barnes and Hut to group elements together, but the number of elements in each box is normally larger than one. Each element contributes to a multipole expansion (a Laurent series) for their box. The number of terms in the series is chosen to give any desired accuracy, but will be small enough to result in computational savings. The expansions are translated to the center of the parent box with the same precision, so that a hierarchy of expansions exists at all levels of the tree. At any point, the appropriate level expansion is used, so that error bound criteria are satisfied. For the very closest particles, the interaction must be computed directly. A further reduction in computational effort is made possible by combining many multipole expansions into local expansions (Taylor series) at a given box, resulting in a operation count of $O(N)$ for large N. By discarding empty boxes at every level, the algorithm adapts equally well to uniform and non-uniform particle distributions. This method is used in the present work, and more details are covered in the next section.

In 1989 Katznelson [38] treated the possibilities of efficiently implementing these tree–based methods on computers with parallel architectures. With a careful mapping between the structure of the algorithm and the hardware architecture, it was estimated that computations with 10^6 particles could be performed in 24 s per time step on the most advanced computers of the day.

A practical implementation of the multipole expansion method (but without local expansions) on a parallel computer was done by van Dommelen and Rundensteiner [78] who devised a unique numbering system to identify boxes in the tree. Each box is given a number in base–3 notation from which the level and location of the box can be

instantly read. The neighbors of the box can be found by binary manipulations. van Dommelen and Rundensteiner also reduce the storage requirements by only having to keep a small number of multipole expansions at any time.

Anderson [3] developed a variation on the method by using a different computational element than multipoles, namely circular contours surrounding each box. According to Poisson's formula, the potential outside the ring can be represented as a convolution of the potential on the ring with a kernel (see for instance Problem 9.35 in [34]). Keeping the value of the potential on the ring with a number of coefficents that are much smaller than the number of vortices, leads to a reduced operation count. A hierarchical structure using such rings can be set up in the same way as for multipoles. The implementation of the box hierarchy is also described in the context of multigrid programming, and it is shown that selecting the proper depth of the tree is essential for good performance.

A.2 The multipole expansion method

The velocity induced at any field point z in the complex plane by a number of vortices is given by:

$$\overline{w} = u - iv = \sum_{k=1}^{K} \frac{i\gamma_k}{z - z_k}$$

Here γ_k and z_k are the strengths and positions of the K vortices, respectively. The multipole expansion method is based on the following theorem [31]:

Theorem 1 (Point vortices to multipole) *Suppose that K vortices are all located within a radius R from the origin, $|z_k| < R, \forall k \in [1, K]$. Then at any field point $|z| > R$, $\overline{w}$ can be expressed as a P term Laurent series:*

$$\overline{w} = \sum_{p=1}^{P} \frac{a_p}{z^p} + \epsilon \tag{A.1}$$

where

$$a_p = \sum_{k=1}^{K} i\gamma_k z_k^{p-1} \tag{A.2}$$

The error is bounded by

$$|\epsilon| < \frac{A}{(c-1)c^P}$$

where $A = \sum_{k=1}^{K} |\gamma_k|$, $c = |R/z|$.

(A.1) follows from the binomial theorem.

Three lemmas allow multipole shifting, conversion to power series, and power series shifting [31]:

Lemma 1 (Shifting multipole expansion) *Suppose that*

$$\sum_{p=1}^{P} \frac{a_p}{(z-z_0)^p} \tag{A.3}$$

is the multipole expansion of the induced velocity for a group of vortices inside a circle of radius R *centered at* z_0. *Then for* z *outside a circle of radius* $R + |z_0|$ *centered at the origin,*

$$\overline{w} = \sum_{l=1}^{P} \frac{b_l}{z^l} + \epsilon$$

where

$$b_l = \sum_{p=1}^{l} a_p z_0^{l-p} \begin{pmatrix} l-1 \\ p-1 \end{pmatrix} \tag{A.4}$$

$$|\epsilon| < \frac{A}{1 - \left|\frac{|z_0|+R}{z}\right|} \left|\frac{|z_0|+R}{z}\right|^{P+1}$$

Lemma 2 (Multipole expansion to power series) *Let* (A.3) *be the multipole expansion of a group of vortices inside a circle of radius* R *centered at* z_0, *such that* $|z_0| > (c+1)R$, $c > 1$. *The field inside a circle of radius* R *centered at the origin can be expressed as a power series:*

$$\sum_{l=0}^{P} b_l z^l + \epsilon$$

where

$$b_l = z_0^{-l} \sum_{p=1}^{P} \frac{a_p}{(-z_0)^p} \begin{pmatrix} l+p-1 \\ p-1 \end{pmatrix} \tag{A.5}$$

For any $P \geq \max(2, 2c/(c-1))$,

$$|\epsilon| < A \frac{4e(P+c)(c+1)+c^2}{c(c+1)} c^{-P-1}$$

Lemma 3 (Shifting power series)

$$\sum_{l=0}^{P} b_l (z - z_0)^l = \sum_{m=0}^{P} z^m \sum_{l=m}^{P} b_l \begin{pmatrix} l \\ m \end{pmatrix} (-z_0)^{l-m} \tag{A.6}$$

The algorithm makes use of these tools by sorting all the vortices into a quad tree of boxes. Through book–keeping of the relationships between boxes, we make sure that expansions are generated or modified only for regions that are *well separated.* In Theorem 1 this means that $c \geq 2$, and a similar requirement applies to the lemmas. Consequently, the relative error associated with any operation is guaranteed to be bounded by 2^{-P}, where P is the number of terms kept in the expansions.

In the current version, the vortices are scaled and shifted so that they fit inside a computational box of size 1x1 centered at the origin, although this is not necessary. The box tree is built by subsequent division of the domain into smaller and smaller boxes, until a lower limit on the number of vortices per box, $nlim$, is reached. Boxes that are empty an any stage are discarded from the process, this is what makes the method adapt to any distribution of vortices.

At the center of any childless box, we form a multipole according to Theorem 1, representing the velocity due to the vortices in that box. The expansion is valid outside the smallest circle that contains the box and and accurate to the desired precision outside a circle twice as big. By Lemma 1 this expansion can be shifted to the center of the parent box, where it is added to the contributions from the brother boxes. The higher level expansion is valid outside a circle containing the parent box. This shifting process propagates up through all levels until the 2-level is reached.

If we chose to use multipole expansion to find the velocity induced between well separated vortices, and use evaluation for the nearest influences, the operation count would go asymptotically like $N \log N$. Greengard and Rokhlin goes one step further

by propagating local expansions down from coarse to fine levels. In the regions where they are accurate, coarse level multipole expansions are converted to local expansion about coarse level box centers according to Lemma 2, and their coefficients are accumulated. These expansions are shifted to the center of children boxes down through all levels. To find the velocity at the location of a vortex in box b, there are 4 kinds of influences that must be added:

1. Direct influence from the other vortices in b, and the boxes adjacent to b.

2. Some influences are computed most effectively using multipole expansions directly generated from vortices in other boxes.

3. Similarly, local expansion terms generated directly from vortices in other boxes are also used.

4. Local expansion terms that have filtered down through the tree as described above.

The complexity analysis shows that the effort goes asymptotically as $O(N)$ for large N [15, 50].

Dr F.T. Korsmeyer of the MIT Ocean Engineering department was kind enough to supply a $O(N)$ computer code originally developed for solution of Laplace's equation with boundary integral elements [39]. He replaced the computational elements by vortex singularities, so the routines could be immediately implemented for vortex simulation in free space. Two modifications to the algorithm are described in the next sections.

A.3 Adaptation to Joukowski foil simulations

In the foil simulations, the boundary conditions on the foil are satisfied by introducing image vortices at the inverse points inside the mapped circle C, which has radius r_c. A typical vortex distribution and box hierarchy in the circle plane is shown in Figure A-1. There are N vortices for which the velocities must be found, and N image

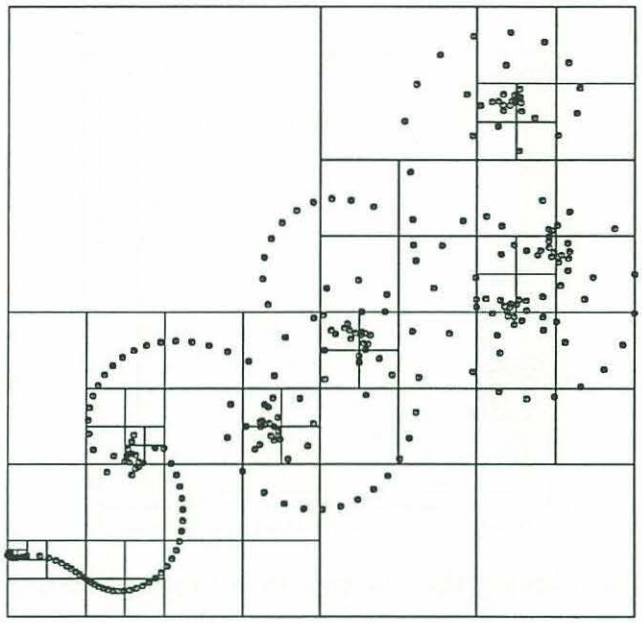

Figure A-1: Typical vortex distribution and box tree for foil simulation.

vortices inside C (C is not shown). It is clear that an inordinate amount of resources would be needed if the box tree was built around all the image vortices. Either the maximum number of vortices per box must be allowed to be very large, or the box tree must be built very deep. In both cases efficiency suffers, because FORTRAN requires all array sizes to be defined a priori and these must be made very large to handle all the image vortices.

Since we are not interested in evaluating the velocities that would be induced on the image vortices, there is no reason to retain them as separate computational elements. Most of the image vortices are within a circle C_2, of radius $r_c/2$, and are therefore well separated from the external vortices. They may be represented by a single multipole element, with the same accuracy guarantee as all the other multipole expansions. In fact, this can be used to advantage even when the direct $O(N^2)$ method is employed.

The tree building procedure needs some modifications to accommodate this special element. First we note that the image vortices to be collected into a multipole must fall within the same box, otherwise the expansion is not appropriate. This sets a limit on how small the smallest box can be. We also require that the multipole must be located at the center of such a smallest box, which has two advantages: (1) The

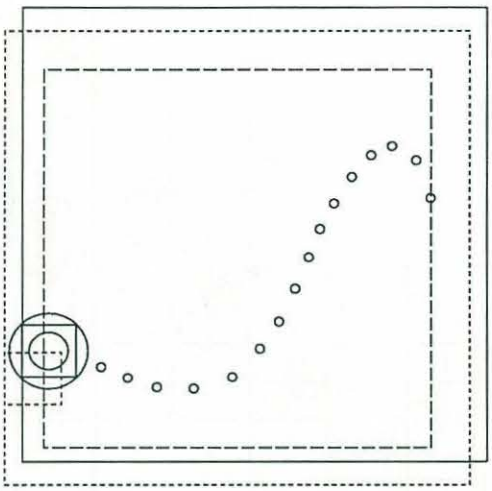

Figure A-2: Moving the box tree to accommodate a multipole.

multipole coefficients can be loaded directly into the the box tree structure without shifting. (2) The smallest box can be smaller than if we had to shift the multipole, giving us the freedom to build the tree deeper.

In order to make all the vortices fit inside the unit square box, we define a scale factor s and shift vector Z as follows:

$$\begin{aligned} x_{max} &= \max_k(\mathrm{Re}\{\zeta_k\}) \\ x_{min} &= \min_k(\mathrm{Re}\{\zeta_k\}) \\ y_{max} &= \max_k(\mathrm{Im}\{\zeta_k\}) \\ y_{min} &= \min_k(\mathrm{Im}\{\zeta_k\}) \\ s &= \max(x_{max} - x_{min}, y_{max} - y_{min}) \\ Z &= \frac{1}{2}(x_{max} + x_{min} + i(y_{max} + y_{min})) \end{aligned}$$

Thus, a square of side s, centered at Z fences in all the vortices. This is the dashed line in Figure A-2. The image vortices that are to be gathered into a multipole (not shown) are within C_2, which has radius $r_c/2$ and is centered at the origin. The size of the smallest box h will be between r_c and $2r_c$, and to put the center of C_2 at the center of the box, we may have to shift Z a distance r_c in the worst case. To make sure that no vortices fall outside the box after this shift, we add $2r_c$ to s. The

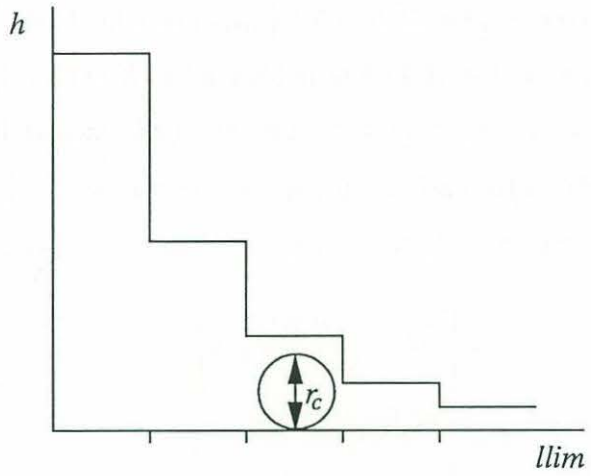

Figure A-3: Setting the maximum level.

enlarged box is shown with dotted lines in the figure.

This only works when the box tree actually puts a smallest box around C_2, which can be guaranteed by setting $nlim = 0$. We introduce instead another stop criterion for the tree builder, $llim$, such that the boxes will be divided until the maximum level $llim$ is reached, or they are empty. Now, if the deepest level of the tree is $llim$, the size of the smallest boxes will be:

$$h = s/2^{llim}$$

The smallest box must be able to contain a circle of diameter r_c, yet be as small as possible, see Figure A-3.

$$\begin{aligned} s/2^{llim+1} \leq \; & r_c \; \leq s/2^{llim} \\ & \Downarrow \\ llim \; = \; & \left[- \frac{\log r_c/s}{\log 2} \right] \end{aligned}$$

The square brackets mean that the integer part should be taken. The scaling factor s and maximum level $llim$ have now been determined, and it remains to find the necessary shift to place the origin $\zeta = 0$ at the center of the smallest box.

First imagine that the dotted box is enirely divided into smallest squares, all of

size h. They can be given a pair of indices (k,l), starting with (1,1) for lower left box. The lower left corner of the (1,1) box is located at $Z-(1+i)s/2$, and counting relative to this corner, we see that an arbitrary box (k,l) has its lower left corner at $Z-(1+i)s/2+(k-1+i(l-1))h$ and the upper right corner at $Z-(1+i)s/2+(k+il)h$. From this we find that the origin is located in the box with indices:

$$k = \left[\frac{s/2 - \mathrm{Re}\{Z\}}{h} + 1\right]$$
$$l = \left[\frac{s/2 - \mathrm{Im}\{Z\}}{h} + 1\right]$$

The distance from the origin to the center of this box is given by:

$$\Delta Z = Z - (1+i)s/2 + (k - 1/2 + i(l - 1/2))h$$

Changing z by $-\Delta Z$ now produces the desired bounding box shown with solid lines in Figure A-2

With the updated values for s and Z, all the vortex locations (including the images) are scaled and shifted according to:

$$\zeta_k \leftarrow \frac{\zeta_k - Z}{s}$$

The multipole for the vortices inside C_2 is constructed according to Theorem 1, and when the actual box tree is built, this is considered to be a single computational element like any other. The tree building routine will continue to divide boxes as long as they contain any element until *llim* is reached. This ensures that the multipole will be at the center of a smallest box, and the coefficients can be loaded directly into the proper array for that box.

At any subsequent stage the $O(N)$ algorithm is unaware of the fact that there is a special kind of element in that box, except that it does not try to compute the velocity of the multipole. This is true also for the other image vortices, those that are inside C but not C_2. All of these have indices higher than N, and it is easy for

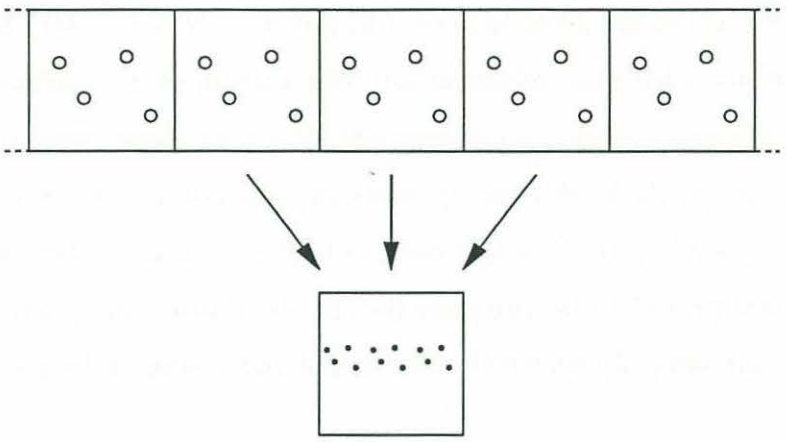

Figure A-4: How periodic boundary conditions are treated.

the algorithm to avoid computing their velocities, although no harm would be done if it did.

The $O(N)$ method breaks even with $O(N^2)$ at about 600 vortices, depending on how large the arrays must be dimensioned. A simple test in the simulation program determines which method to use.

A.4 Adaptation to periodic boundary conditions

Rokhlin and Greengard explain how to incorporate different boundary conditions on the computational box by image elements mirrored about the box walls. In the case of periodic boundary conditions in the x direction, the images take the form shown in Figure A-4. The vortex configuration in the computational box is repeated in image boxes going off to infinity in the positive and negative x direction. When the influence of all the image vortices is taken into account, periodic boundary conditions are guaranteed. It may be a little surprising that the multipole expansion method, which is based on clustering groups of vortices that are well separated compared to the regions that they occupy, is able to deal with such a case.

As Figure A-4 indicates, the vortices that are located in the two image boxes next to the computational box are taken into account directly, by scaling into a new computational box. The box tree is then built with all $3N$ vortices and the $O(N)$ computation is performed. In the same fashion as for the circle images in the section

above, the image vortices are given indices that run from $N+1$ to $3N$, and they can therefore be screened such that velocities are only calculated for vortices 1 through N. However, all the arrays must be dimensioned for $3N$ elements, and it is clear that a more efficient code could be devised by repeating the box tree for the two nearest image boxes, and extending the lists that contain information about box relationships. The simple method proved to be adequate for the simulations in Chapter 5, but for larger runs it would certainly be worthwhile to put more effort into a more efficient code.

It remains to compute the influence of all the other image boxes. These are well separated from the computational box and Lemma 2 provides a way of collecting their influence into a Taylor series about $z = 0$. The 0-level multipole expansion for the computational box has the form (A.3). Since we "polluted" the computational box with $2N$ images, we cannot find this expansion from the $O(N)$ routine, and it must be computed from scratch using Theorem 1 for the N vortices in the original computational box. This is an $O(N)$ operation so we can afford it. Now we must sum the influence of the 0–level expansions over all well separated image boxes, which have centers at $n = \pm 2, \pm 3, ...$

$$\sum_{n} \sum_{p=1}^{P} \frac{a_p}{(z-n)^p} \tag{A.7}$$

Lemma 2 says that the multipole expansions can be converted to local expansions about $z = 0$:

$$\sum_{n} \sum_{l=0}^{P} b_l z^l \tag{A.8}$$

where

$$b_l = n^{-l} \sum_{p=1}^{P} \frac{a_p}{(-n)^p} \begin{pmatrix} l+p-1 \\ p-1 \end{pmatrix} \tag{A.9}$$

These expansions are accurate to the desired precision inside the computational box.

By interchanging order of summation, we arrive at the final expression:

$$\sum_{l=0}^{P} B_l z^l \tag{A.10}$$

where

$$B_l = \sum_n b_l = \sum_{p=1}^{P} a_p (-1)^p \begin{pmatrix} l+p-1 \\ p-1 \end{pmatrix} \sum_n \frac{1}{n^{l+p}} \tag{A.11}$$

This local expansion can be applied at all vortex locations and is added to the other influences already described.

The rest of this section is concerned with the evaluation of the last series in (A.11), which can be precomputed and stored. We can write

$$\sum_n \frac{1}{n^{l+p}} = \sum_{n=2}^{\infty} \left(\frac{1}{n^{l+p}} + \frac{1}{(-n)^{l+p}} \right)$$

For odd powers, the two terms cancel, and for even powers they are the same, hence

$$\sum_n \frac{1}{n^{l+p}} = \begin{cases} 0 & \text{for } l+p \text{ odd} \\ 2S(l+p) & \text{for } l+p \text{ even}, \quad S(k) = \sum_{n=2}^{\infty} \frac{1}{n^k} \end{cases}$$

The series $S(k)$, with the lower limit replaced by 1, has a long history, reviewed by Stark in [73]. Stark also provides exact expressions that apply to the series with even k:

$$\begin{aligned} S(2) &= \frac{\pi^2}{6} - 1 \\ S(4) &= \frac{\pi^4}{90} - 1 \\ S(6) &= \frac{\pi^6}{945} - 1 \end{aligned}$$

There are recursion relationships that give us the value for any even argument, but they become difficult to use in practice because the expressions involve fractions and differences between very large numbers, leading to roundoff error. Therefore it was decided to sum the series directly with a finite number of terms, for arguments higher

Table A.1: Results from summing $S(4)$ different ways.

double precision, forward summing:	0.082323233296059505000
double precision, backward summing:	0.082323233296059612000
single precision, backward summing:	0.082323238253593444000
single precision, forward summing:	0.082323119044303894000

than 6. A bound on the truncation error can be found by bounding the terms in the series by a continuous function in n:

$$\sum_{n=N+1}^{\infty} \frac{1}{n^k} < \int_{N+1/2}^{\infty} \frac{dn}{(n-1/2)^k} = \frac{N^{1-k}}{k-1}$$

A lower bound on the value of $S(k)$ itself can be found in a similar way:

$$\sum_{n=2}^{\infty} \frac{1}{n^k} > \frac{2^{1-k}}{k-1}$$

The relative error is thus bounded:

$$\epsilon = \frac{\sum_{n=N+1}^{\infty} \frac{1}{n^k}}{\sum_{n=2}^{\infty} \frac{1}{n^k}} < \left(\frac{N}{2}\right)^{1-k}$$

This relationship tells us how many terms are needed for a desired relative error bound:

$$N > 2\epsilon^{\frac{1}{1-k}}$$

For instance, we find that for $\epsilon = 10^{-8}$, $k = 8$ we need 28 terms. In order to keep track of roundoff error we must also know the ratio between the first and last term in the summation:

$$\delta = \left(\frac{2}{N}\right)^k$$

This turns out to be a concern, because δ is smaller than ϵ. So in order to compute S to single precision, we must use double precision arithmetic or evaluate the sum backwards. Table A.1 shows the result for the 4 different ways of computing in the case $k = 4$, $\epsilon = 10^{-8}$. 929 terms were needed. For the single precision sums,

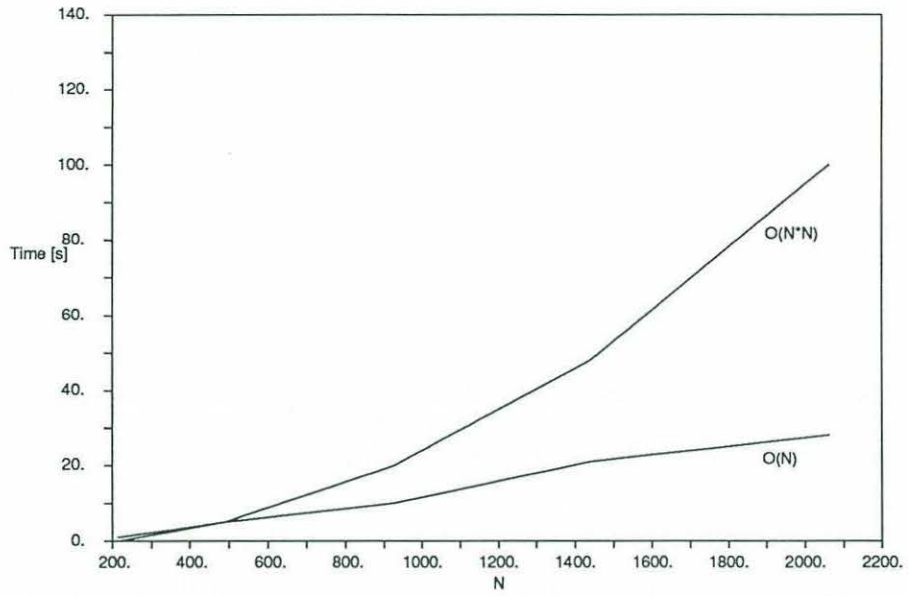

Figure A-5: Execution times for periodic boundary conditions.

we see that an extra significant digit can be obtained by summing backwards. The two double precision cases differ by 10^{-15}, indicating that the error bounds are very conservative. Single precision is sufficient for the applications in this work, and $S(k)$ was computed and stored in a lookup table.

Figure A-5 shows how the execution times for the method compares with direct computation, we break even at approximately 200 vortices.

Bibliography

[1] M. Abramowitz and I.A. Stegun. *Handbook of Mathematical Functions.* Dover Publications, Inc., New York, ninth edition, 1970.

[2] C.R. Anderson. A method of local corrections for computing the velocity field due to a distribution of vortex blobs. *Journal of Computational Physics*, 62:111–123, 1986.

[3] C.R. Anderson. An implementation of the fast multipole method without multipoles. *SIAM Journal of Scientific and Statistical Computing*, 13:923–947, July 1992.

[4] A.W. Appel. An efficient program for many-body simulation. *SIAM Journal of Scientific and Statistical Computing*, 6(1):85–103, January 1985.

[5] R.D. Archer, J. Sappupo, and D.S. Betteridge. Propulsion characteristics of flapping wings. *The Aeronautical Journal of the Royal Aeronatical Society*, 83(825):355–371, Sept 1979.

[6] H. Aref. Chaos in the dynamics of a few vortices - fundamentals and applications. In F.I. Niordson and N. Olhoff, editors, *IUTAM Theoretical and Applied Mechanics*, pages 43–68. Elsevier Science Publishers B.V. (North-Holand), 1985.

[7] G.R. Baker. The 'Cloud in Cell' technique applied to the roll up of a vortex sheet. *Journal of Computational Physics*, 31:76–95, 1979.

[8] J. Barnes and P. Hut. A hierachical $O(N \log N)$ force-calculation algorithm. *Nature*, 324:446–449, 1986.

[9] B.C. Basu and G.J. Hancock. The unsteady motion of a two-dimensional aerofoil in incompressible inviscid flow. *Journal of Fluid Mechanics*, 87:159–178, 1978.

[10] G.K. Batchelor. *An Introduction to Fluid Mechanics.* Cambridge University Press, 1967.

[11] J.T. Beale and A. Majda. High order accurate vortex methods with explicit velocity kernels. *Journal of Computational Physics*, 58:188–208, 1985.

[12] A.J. Bilanin, M.E. Teske, and G.G Williamson. Vortex interaction and decay in aircraft wakes. *AIAA Journal*, 15:250–260, 1977.

[13] G. Birkhoff and J. Fisher. Do vortex sheets roll up? *Rendiconti del Circolo Matematico di Palermo*, 8:77–90, 1959.

[14] G. Petit Bois. *Tables of Indefinite Integrals.* Dover, 1961.

[15] J. Carrier, L. Greengard, and V. Rokhlin. A fast adaptive multipole algorithm for particle simulations. *SIAM Journal on Scientific and Statistical Computing*, 9(4):669–686, July 1988.

[16] D.H. Choi and K. Landweber. Inviscid analysis of two-dimensional airfoils in unsteady motion using conformal mapping. *AIAA Journal*, 28(12):2025–2033, December 1990.

[17] A.J. Chorin. Discretization of a vortex sheet with an example of roll-up. *Journal of Computational Physics*, 13:423–429, 1973.

[18] A.J. Chorin. Numerical study of slightly viscous flow. *Journal of Fluid Mechanics*, 57:785–796, 1973.

[19] J.P. Christiansen and N.J. Zabusky. Instability, coalencence and fission of finite-area vortex structures. *Journal of Fluid Mechanics*, 61:219–243, 1973.

[20] R.R. Clements. An inviscid model of two-dimensional vortex shedding. *Journal of Fluid Mechanics*, 57:321–336, 1973.

[21] J.D. DeLaurier and J.M. Harris. Experimental study of oscillating–wing propulsion. *AIAA Journal*, 19, 1982.

[22] P.G. Drazin and W.H. Reid. *Hydrodynamic Stability.* Cambridge University Press, Cambridge, 1987.

[23] D.G. Dritschel. Vortex properties of two-dimensional turbulence. *Physics of Fluids A*, 5:984–997, 1993.

[24] P.T. Fink and W.K. Soh. A new approach to roll-up calculations of vortex sheets. In *Proceedings of the Royal Society*, pages 195–209, 1978. A362.

[25] T. Fujinami, G.S. Dulikravich, and A.A. Hassan. Free-vortex method simulation of unsteady airfoil/vortex interaction. In *AIAA 4th Applied Aerodynamics Conference*, pages 189–196, San Diego, CA, 1986. A Collection of Technical Papers.

[26] H. Glauert. *The Elements of Aerofoil and Airscrew Theory.* Cambridge University Press, 1926.

[27] S. Goldstein, editor. *Modern Developments if Fluid Dynamics.* Dover, 1965. 2 Volumes.

[28] R. Gopalkrishnan. *Vortex-Induced Forces on Oscillating Bluff Cylinders.* PhD thesis, Massachusetts Institute of Technology, Cambridge, MA, 1983.

[29] Gradshteyn and Ryzhik. *Tables of Integrals, Series and Products.* Academic Press, 1980.

[30] J.M.R. Graham. The forces on sharp-edged cylinders in oscillatory flow at low Keulegan-Carpenter number. *Journal of Fluid Mechanics*, 68:109–128, 1980.

[31] L. Greengard and V. Rokhlin. A fast algorithm for particle simulations. *Journal of Computational Physics*, 73:325–348, 1987.

[32] J. Grue, A. Mo, and E. Palm. Propulsion of a foil moving in water waves. *Journal of Fluid Mechanics*, 186:393–417, 1988.

[33] O.H. Hald. Convergence of vortex methods. In K.E. Gustafson and J.E. Sethian, editors, *Vortex Methods and Vortex Motion.* Society for Industrial and Applied Mathematics, 1991.

[34] F.B. Hildebrand. *Advanced Calculus for Applications.* Prebntice–Hall, Inc., 2. edition, 1976.

[35] R.W. Hockney and J.W. Eastwood. *Computer Simulation Using Particles.* McGraw–Hill, New York, NY, 1981.

[36] M.-K. Huang and C.-Y. Chow. Trapping of a free vortex by joukowski airfoils. *AIAA Journal*, 20(1):292–298, March 1982.

[37] E.R. Booth Jr. Experimental observations of two-dimensional blade-vortex interaction. *AIAA Journal*, 28(8):1353–1359, August 1990.

[38] J. Katznelson. Computational structure of the n–body problem. *SIAM Journal of Scientific and Statistical Computing*, 10(4):787–815, July 1989.

[39] F.T. Korsmeyer. An order N algorithm for the solution of the boundary integral equations of potential flow. In *The Fifth International Workshop on Water Waves and Floating Bodies*, Manchester, England, 1990.

[40] R. Krasny. A numerical method for vortex sheet roll–up. In D. Rues and W. Kordulla, editors, *Proceedings of the Sixth GAMM-Conference on Numerical Methods in Fluid Mechanics*, pages 193–200, Braunschweig/Wiesbaden, 1986. Friedr. Vieweg & Sohn.

[41] R. Krasny. Computation of vortex sheet roll-up. In C. Anderson and C. Greengard, editors, *Vortex Methods, Proceedings of the U.C.L.A. Workshop held in Los Angeles*, pages 9–22, Berlin Heidelberg New York London Paris Tokyo, May 1987. Springer Verlag.

[42] C.-M. G. Lam. Nonlinear wake evolution of joukowski aerofoils in severe maneuver. Master's thesis, Massachusetts Institute of Technology, Cambridge, MA, 1989.

[43] A. Leonard. Vortex methods for flow simulation. *Journal of Computational Physics*, 37:289–335, 1980.

[44] Sir James Lighthill. *Mathematical Biofluiddynamics.* Society for Industrial and Applied Mathematics, Philadelphia, 1975.

[45] R.K. Lo and L. Ting. Studies of the merging of vortices. *Physics of Fluids*, 19:912–913, 1976.

[46] Mallock. On the resistance of air. *Proceedings of the Royal Society*, 79:262–265, 1907.

[47] W.J. McCroskey. Unsteady airfoils. *Annual Review of Fluid Mecanics*, 14:285–311, 1982.

[48] J.E. McCune and T.S. Tavares. Perspective: Unsteady wing theory – The Kármán/ Sears legacy. *Journal of Fluids Engineering*, 115(4):548–560, December 1993.

[49] D.W. Moore. A numerical study of the roll-up of a finite vortex sheet. *Journal of Fluid Mechanics*, 63:225–235, April 1973.

[50] K. Nabors, T. Korsmeyer, F.T. Leighton, and J. White. Preconditioned, adaptive, multipole-accelerated iterative methods for three-dimensional potential integral equations of the first kind. *SIAM Journal of Scientific and Statistical Computing*, To be published, 1993.

[51] J.N Newman. *Marine Hydrodynamics.* M.I.T. Press, 1977.

[52] H.O. Nordmark. *Higher Order Vortex Methods with Rezoning.* PhD thesis, University of California, Berkeley, 1988.

[53] A.G. Panaras. Numerical modeling of the vortex/airfoil interaction. *AIAA Journal*, 25(1):5–11, January 1987.

[54] M. Perlman. On the accuracy of vortex methods. *Journal of Computational Physics*, 59:200–223, 1985.

[55] Lord Rayleigh. *The Theory of Sound.* Macmillan, 2. edition, 1894.

[56] K.V. Roberts and J.P. Christiansen. Topics in computational fluid mechanics. In G.R. Macleod, editor, *The Impact of Computers in Physics, Proceedings of the First European Conference on Computational Physics*, pages 14–32. North-Holland Publishing Company, April 1972.

[57] P.H. Roberts and R.J. Donnelly. Superfluid mechanics. *Annual Review of Fluid Mechanics*, 6:179–225, 1974.

[58] M.W. Rosen. Water flow about a swimming fish. Master's thesis, University of California in Los Angeles, May 1959.

[59] L. Rosenhead. Formation of vortices from a surface discontinuity. In *Proceedings of the Royal Society*, page 170, 1931. A134.

[60] P.G. Saffman and G.R. Baker. Vortex interactions. *Annual Review of Fluid Mechanics*, 11:95–122, 1979.

[61] P.G. Saffman and J.S. Sheffield. Flow over a wing with an attached free vortex. *Studies in Applied Mathematics*, 57:107–117, 1977.

[62] T. Sarpkaya. An inviscid model of two-dimensional vortex shedding for transient and asymptotically steady separated flow over an inclined plate. *Journal of Fluid Mechanics*, 68:109–128, 1975.

[63] T. Sarpkaya. Computational methods with vortices - The 1988 Freeman scholar lecture. *Journal of Fluids Engineering*, 111:5–52, March 1989.

[64] J.O. Scherer. Experimental and theoretical investigation of large amplitude oscillating foil propulsion systems. Technical Report 662-1, Hydronautics Inc., Laurel, Maryland, Dec 1968.

[65] W. Schmidt. Der wellpropeller, ein neuer antrieb für wasser-,land-, und luftfahrzeuge. *Z. Flugwiss.*, 13:472–479, 1965.

[66] Y.-M. Scolan and O.M. Faltinsen. Numerical studies of separated flow from bodies with sharp corners by the vortex in cell method. *Journal of Fluids and Structures*, 8(2):201–230, 1994.

[67] W.R. Sears. Some aspects of non-stationary airfoil theory and its practical application. *Journal of the Aeronautical Sciences*, 8(3):104–108, January 1941.

[68] L.I. Sedov. *Two-Dimensional Problems in Hydrodynamics and Aerodynamics.* Interscience Publishers, New York, London, Sydney, 1965.

[69] J.A. Sethian. A brief overview of vortex methods. In K.E. Gustafson and J.E. Sethian, editors, *Vortex Methods and Vortex Motion.* Society for Industrial and Applied Mathematics, 1991.

[70] Q.-Y. Sheen. *Potential Flow Analysis of Unsteady Joukowski Airfoil in the Presence of Discrete Vortices.* PhD thesis, University of Colorado, Boulder, CO, 1986.

[71] C. Shih, L. Lourenco, L. Van Dommelen, and A. Krothapalli. Unsteady flow past an airfoil pitched at constant rate. In J.A. Miller and D.P. Telionis, editors, *International Symposium on Nonsteady Fluid Dynamics*, pages 41–50, Toronto, Ontario, Canada, June 1990. ASME.

[72] J.R. Spreiter and A.H. Sacks. The rolling up of the trailing vortex and its effect on the downwash behind wings. *Journal of the Aeronatical Sciences*, 18:21–32, 1951.

[73] E.L. Stark. The series $\sum_{k=1}^{\infty} k^{-s}$, $s = 2, 3, 4, ...$, once more. *Mathematics Magazine*, 41:197–202, 1974.

[74] J. Straus, P. Renzoni, and R.E. Mayle. Airfoil pressure measurements during a blade vortex interaction and a comparison with theory. *AIAA Journal*, 28(2):222–228, February 1990.

[75] L.M. Milne Thomson. *Theoretical Hydrodynamics.* The MacMillan Company, New York, 1960.

[76] G.S. Triantafyllou, M.S. Triantafyllou, and M.A Grosenbaugh. Optimal thrust development in oscillating foils with application to fish propulsion. *Journal of Fluids and Structures*, 7:205–224, 1993.

[77] M.S. Triantafyllou and G.S. Triantafyllou R. Gopalkrishnan. Wake mechanics for thrust generation in oscillating foils. *Physics of Fluids*, 3(12):2835–2837, December 1991.

[78] L. van Dommelen and E.A. Rundensteiner. Fast, adaptive summation of point forces in the two-dimensional poisson equation. *Journal of Computational Physics*, 83:126–147, 1989.

[79] Th. von Karman and W.R. Sears. Airfoil theory for non-uniform motion. *Journal of the Aeronautical Sciences*, 5(10):379–390, August 1938.

[80] D. Weihs. Semi–infinite vortex trails, and their relation to oscillating airfoils. *Journal of Fluid Mechanics*, 54, 1972.

[81] D. Weihs. On the existence of multiple Kármán/ vortex–street modes. *Journal of Fluid Mechanics*, 61:199–205, 1973.

[82] R.W. Yeung and M. Vaidhyanathan. Flow past oscillating cylinders. *Journal of Offshore Mechanics and Arctic Engineering*, 115(4):197–205, 1993.